

UCLA

UCLA Electronic Theses and Dissertations

Title

Effects of Flow Patterns on Tissue Development in 3D Culture

Permalink

<https://escholarship.org/uc/item/8rt15558>

Author

Nakasone, Russell Ray

Publication Date

2023

Peer reviewed|Thesis/dissertation

UNIVERSITY OF CALIFORNIA

Los Angeles

Effects of Flow Patterns on Tissue Development in 3D Culture

A thesis submitted in partial satisfaction

of the requirements for the degree

Master of Science in Biochemistry, Molecular and Structural Biology

by

Russell Ray Nakasone

2023

© Copyright by
Russell Ray Nakasone
2023

ABSTRACT OF THE THESIS

Effects of Flow Patterns on Tissue Development in 3D Culture

by

Russell Ray Nakasone

Master of Science in Biochemistry, Molecular and Structural Biology

University of California, Los Angeles, 2023

Professor Louis-Serge Bouchard, Chair

Objective: Three dimensional cell and tissue culture outcomes depend on mechanical forces in their environment and sufficient delivery of nutrients and removal of waste. Flow and shear influence parenchymal cell distribution and vascular morphogenesis. Herein a bioreactor which can control fluid flow and shear patterns over large areas was developed as a tool for tissue engineering. *Methods:* A 12-inlet perfusion bioreactor was constructed to be compatible with multiple types of tissue engineering scaffolds including biopolymer hydrogels and macroporous sponges and can support the growth and viability of thick tissue scaffolds. Scaffolds containing mammalian cells cultured under flow were compared to static conditions and other flow patterns. *Results:* Flow patterns in the scaffolds were obtained using MRI flow maps. Hydrogels and commercial sponges were assessed for 3D culture compatibility and Gel 2 (a specific ECM hydrogel mixture), Collagen, and Gelatin sponges were found to be both optimal for cell growth and compatible with perfusion flow. Culture experiments determined the feasibility of our bioreactor in supporting thick tissue growth and viability and various flow patterns were shown to alter cell distribution, growth, and viability. *Conclusion:* We demonstrated the ability of the bioreactor to implement macroscopic, tun-

able flow patterns in a biocompatible environment suitable for cell and tissue culture and found distinct differences in tissue development from different flow patterns. *Significance:* The bioreactor will enable future studies on different flow patterns and their effects on cell growth and viability for medically relevant tissues and could inform on culture conditions that better mimic what occurs *in vivo* during tissue development.

The thesis of Russell Ray Nakasone is approved.

Tzung Hsiai

William M. Gelbart

Song Li

Louis-Serge Bouchard, Committee Chair

University of California, Los Angeles

2023

To my parents who have provided endless support and encouragement.

TABLE OF CONTENTS

1	Introduction	1
1.1	Tissue Engineering	1
1.2	Cells	3
1.2.1	Cell Types	3
1.2.2	Signaling Cues and Cell Behavior and Development	4
1.3	Tissue Culture Methods	7
1.3.1	Scaffold Design	9
1.3.2	Bioreactor Culture Systems	12
2	Design, Operation, and Maintenance of Custom Twelve-Channel Bioreac-	
tor		15
2.1	Materials and methods	17
2.1.1	Bioreactor Body Design	17
2.1.2	TC Chamber Design	18
2.1.3	Bioreactor System Setup	20
2.1.4	Scaffold Preparation	25
2.1.5	Reactor Operation	29
2.2	Results	32
2.2.1	General Bioreactor Performance	32
2.2.2	Scaffold Results Determine Compatible Scaffolds for Culture and Per- fusion Flow	32
2.2.3	Flow Through Scaffolds	35

2.2.4	Discussion	49
3	Tissue Culture Experiments with Custom Bioreactor	52
3.1	Materials and Methods	53
3.2	Results	56
3.2.1	Effect of Flow on Cell Growth Distribution in 3D	56
3.2.2	Feasibility of Growing Thick Tissue Constructs with Novel Bioreactor	57
3.2.3	Effects of Different Flow Patterns on Cell Growth and Viability of Tissue Constructs	59
3.3	Discussion	60
4	Conclusion	72
A	Supplemental Figures	75
A.1	Code for Density Heatmaps in Fiji	75
	References	78

LIST OF FIGURES

1.1	Tissue Engineering Overview. Graphic illustrates the tissue engineering ‘triad’ where the main components in a tissue model are cells, scaffold, and signaling cues. © 2023 Abdelaziz et al. Adapted from [1] originally distributed under the Creative Commons Attribution License.	2
1.2	Mechanical Cues and Mechanotransduction. (A) Graphic illustrates both the intrinsic and extrinsic cues experienced by cells. Extrinsic cues on the right come from shear forces generated from fluid and local (intrinsic) cues come from interactions with cell density, shape, and the extracellular matrix (ECM). (B) Graphic illustrates the mechanotransduction pathway. Mechanical cues alter the cytoskeleton which activates signals downstream into the nucleus which influence cellular behavior. © 2023 Petzold and Gentleman. Adapted from [2]; originally distributed under the Creative Commons Attribution License.	6
1.3	Illustration of 2D vs 3D Culture. Simple graphic illustrates differences between 2D and 3D culture. Cells are constrained to a flat morphology and limited in cell-cell and cell-matrix interactions in 2D culture while 3D culture provides the ability for expansion to native morphology and interactions.	8
1.4	Pore Size Effects on Mesenchymal Stem Cell Fate. Graphic illustrates how different pore sizes can influence mesenchymal stem cells to either differentiate or maintain stemness. Adapted from [3] with permission, © Elsevier Ltd. 2021	11
1.5	Engineering Parameters for Different Bioreactors. Figure illustrates different engineering parameters for different, common bioreactor types. © 2013 Nasim Salehi-Nik et al. Adapted from [4]; originally distributed under the Creative Commons Attribution License.	13
2.1	Bioreactor Design. 3D models of the side and front of the bioreactor.	18

2.2	Bioreactor Design. 3D models of the top and side of the TC chamber. Inlet and outlet directions are labeled.	19
2.3	Silicone Gasket Casting. Workflow diagram of the silicone mold assembly and casting for sponges and biopolymer gels. A magnified view of the last step highlights how metal tubing was aligned. Adapted from [5] with permission, © Brian Archer 2021	20
2.4	Bioreactor Body Assembly. Top of the figure shows schematic of full assembly of bioreactor with scaffold and TC chamber. Bottom figure shows photograph of fully assembled bioreactor body.	21
2.5	Bioreactor System Setup. Full view of the system setup. Each photo comprises a half of the system.	22
2.6	Temperature and Gas Control Components. (a) Photograph of 2GF-mixer from Oko-labs which was used to maintain 5% CO ₂ . (b) Steel pipe heater design used to heat the flow of air made from Belilove Company-Engineers. (c) Temperature control console that measures and controls temperature which was also provided from Belilove Company-Engineers.	23
2.7	Process Flow Diagram. Color Legend: Black - cell culture media, blue - gas flow, yellow/purple lines - digital signals generated and received by computer, red - 37°C air flow. Abbreviations: BT - Bubble Trap, PR - Pressure Relief, BP - Back Pressure. Adapted from [5] with permission, © Brian Archer 2021	24
2.8	Diagram of the Gel Casting Apparatus. Diagram demonstrates full assembly and steps taken for gel casting.	27
2.9	Sponge Laser Cutting Apparatus. Diagram includes the components and assembly of the apparatus used to contain and position the sponge during laser cutting. Adapted from [5] with permission, © Brian Archer 2021	28

2.10	Flow Rate and Temperature Monitors. Figure shows measurements from flow rate control computer and temperature control console. (a) Flow rate measurements were generated by MATLAB while controlling bioreactor inlet flow rates. Digitally measured parameters related to the bioreactor are plotted over time. Upper plot shows flow rates measured in each of the twelve inlets. Lower left plot shows pressure measured downstream of the peristaltic pump. Lower right plot displays the total flow rate through the bioreactor. Channels 1-4 were set to $1 \text{ mL}\cdot\text{min}^{-1}$, channels 5-8 were set to $0.5 \text{ mL}\cdot\text{min}^{-1}$, and channels 9-12 were set to $0 \text{ mL}\cdot\text{min}^{-1}$. (b) Temperature measurements shown with control console during culture. The red number is the measured value while the green number is the temperature setpoint. Flow rate monitor image and description is originally from [5] with permission, © Brian Archer 2021	33
2.11	HAEC Static Culture in Biopolymer Gels 1-4. Confocal images of HAECs cultured statically in each gel composition. Cell nuclei were stained with DAPI (shown in blue) and actin was stained with Texas Red™-X Phalloidin (shown in red). Adapted from [5] with permission, © Brian Archer 2021	34
2.12	HAEC Static Culture in Macroporous Sponges. Confocal stacks of HAECs cultured statically in collagen, gelatin, and alginate-RGD sponges from left to right. Cell nuclei were stained with DAPI (shown in blue), and actin was stained with Texas Red™-X Phalloidin (shown in red). Adapted from [5] with permission, © Brian Archer 2021	35

2.13	Fluid Velocity Maps in Biopolymer Scaffold. (a) Diagram of gel scaffold highlighting the pattern of open channels within the gel. Diagram is labelled with channel inlet numbers and the Cartesian coordinate orientation corresponding to all other fluid velocity maps presented. (b) Photograph of biopolymer scaffold mounted in bioreactor. The region of interest (ROI) used when cropping and displaying flow-weighted MRIs is outlined in green. (c) Fluid velocity maps within biopolymer scaffold corresponding to input flow rates of $0.5 \text{ mL}\cdot\text{min}^{-1}$ in all inlet channels. Velocity maps were cropped to include only the scaffold region of the MRI. Values in colorized scale bars are in $\text{mm}\cdot\text{s}^{-1}$. Adapted from [5] with permission, © Brian Archer 2021	36
2.14	Flow and Shear Maps. The left is a map of the total flow speed magnitude calculated from the directional fluid velocity maps in Fig. 2.13. The middle plot is a flow vector field determined from x and y fluid velocity maps. The right panel is a shear rate map calculated from the x and y fluid velocity maps. Adapted from [5] with permission, © Brian Archer 2021	37
2.15	Analysis of Flow-weighted MRI. (a) Top: cross section view of v_y modelled in channel and surrounding matrix. Middle: plot of modelled v_y along red line. Bottom: plot of modelled $\dot{\gamma}$ in matrix and channel along red line. (b) Top: cross section view of v_y in channel and surrounding matrix segmented with the same x resolution used in the flow-weighted MRI from Fig. 2.13. Middle and Bottom: plot of modelled \bar{v}_y and $\bar{\dot{\gamma}}$ profiles respectively. Black profile is segmented with same x resolution used in MRI. Magenta profile is unsegmented. (c) Top: portion of flow speed map seen in Fig. 2.13 with ROI highlighted in red. Middle: profile of average flow speed in ROI along x direction. Bottom: profile of average shear rate in ROI along x direction. Adapted from [5] with permission, © Brian Archer 2021	50

2.16	Flow and Shear Maps in Collagen Sponge. The left panel is a map of the total flow speed magnitude. The middle panel is a flow vector field made from the \bar{v}_x and \bar{v}_y maps. The right panel is a map of $\bar{\gamma}$. Adapted from [5] with permission, © Brian Archer 2021	51
2.17	Wall Shear in Collagen Pores. Map of estimated shear stress at pore walls in collagen sponge plotted in dynes-cm ⁻² . Adapted from [5] with permission, © Brian Archer 2021	51
3.1	Flow Pattern Influences Parenchymal Distribution. (a) Diagram highlighting imaged regions of scaffold. Numbered regions are indicated with respect to the flow channels surrounding the TC chamber. Square regions highlighted in blue correspond to actual size of confocal micrographs. (b) Confocal micrographs of HEK293 cells stained with DAPI cultured on porous collagen scaffold for 5 days under the flow pattern with 0.5 mL/min flow rates in all inlets. (c) Confocal micrographs of select regions of scaffold seeded with HEK293 cells for 2 hours. (d) Confocal micrographs of HEK293 cells cultured on a porous collagen scaffold for 5 days statically in an incubator. Adapted from [5] with permission, © Brian Archer 2021	55
3.2	Representative Micrographs of a Whole Scaffold Sample. (a) Micrograph of the scaffold with all fluorescent signals overlayed (cyan-DAPI, IIT-Green, Orange-CMRA). A 8× zoomed inset image is shown on the upper right corner. (b) Micrograph of the scaffold with DAPI only. A 8× zoomed inset image is shown on the upper right corner. (c) Micrograph of the scaffold with CMRA only at the region around the 8× zoomed inset image. (d) Micrograph of the scaffold with IIT only at the region around the 8× zoomed inset image. The brightness and contrast were adjusted for all images using Fiji for visualization.	64

3.3	Plot for CMRA over the Designated Culture Period. CMRA Density plot over time. Density was calculated as the number of raw CMRA cell counts divided by the volume of the scaffold imaged. The red plot is for static culture sample densities while the blue plot is for perfusion culture densities. Height of bar and error bars are a measure of the mean and standard deviation.	65
3.4	Representative CMRA Micrographs of Central Region of Scaffold Sections from Various Culture Groups. (a) Graphic showing direction of flow in scaffold under perfusion culture (channels 1-4 at 1 mL/min). Blue square represents central region where micrographs were taken. (b) Representative micrograph at central region of scaffold section after 0 Days of culture just after seeding. (c) Representative micrograph at central region of scaffold section from 3 Day static culture. (d) Representative micrograph at central region of scaffold section from 5 Day static culture. (e) Representative micrograph at central region of scaffold section from 3 Day perfusion culture. (f) Representative micrograph at central region of scaffold section from 5 Day perfusion culture. Contrast and brightness were adjusted with Fiji to remove autofluorescence and enhance visualization.	66
3.5	Representative CMRA Micrographs of Edge of Scaffold Sections After 5 Days from Static or Perfusion Culture. (a)Graphic showing direction of flow in scaffold under perfusion culture (channels 1-4 at 1 mL/min). Blue square represents central region where micrographs were taken. (b) Representative micrograph of an edge of a scaffold section after 5 days of static culture. (c) Representative micrograph of an edge of a scaffold section after 5 days of perfusion culture. Contrast and brightness were adjusted with Fiji to remove autofluorescence and enhance visualization.	67

3.6	Higher Objective Micrographs of Cell-Cell Interactions in Tissue Scaffold. (a) 20× image of a cell clump in tissue scaffold. (b) 100× image visualizing cell-cell interactions in scaffold with expected subcellular staining visualized. . .	67
3.7	Cell Distribution Analysis of Scaffolds From Different Culture Conditions using Intensity Heatmaps. (a) Intensity heatmap for CMRA from a section of a static culture scaffold. (b) Intensity heatmap for CMRA from a section of a perfusion culture scaffold (1 mL/min flow rates at channels 1-4). (c) Intensity heatmap for CMRA from another lower section of a perfusion culture scaffold (1 mL/min flow rates at channels 1-4).	68
3.8	Dead Cell Analysis for Various Culture Groups. (a) Plot of Raw IIT Counts from the whole scaffold of different culture groups. NF stands for No Flow or static culture conditions and F stands for Flow or perfusion culture conditions. (b) Plot of Raw IIT Counts from the core or center of the scaffold. NF stands for No flow or static culture conditions and F stands for Flow or perfusion culture conditions. (c) Plot of Raw IIT Counts from the periphery or top of the scaffold. NF stands for No flow or static culture conditions and F stands for Flow or perfusion culture conditions. (d)-(e) Representative 5-day culture IIT micrographs. Top two images are micrographs from center section of the scaffold. Bottom two images are micrographs from sections specifically from the top of the scaffold. Each row has the static condition micrograph on the left and the perfusion culture condition on the right.	69
3.9	Plots for CMRA and IIT of Different Culture Groups. (a) Plot of CMRA cell density for different culture groups. Density was calculated as CMRA cell counts divided by volume of the scaffold. (b) Plot of raw IIT cell counts.	70

3.10	MRI Flow Maps and CMRA Micrographs for 0.5 mL/min Channel Flow Rate Culture Groups.	(a) Graphic illustrating the direction of flow rate within the scaffold chamber. (b) Flow maps from flow-weighted MRI of flow patterns generated from 0.5 mL/min flow rates at the designated channels (1-4 for left map, 5-8 for middle map, 9-12 for right map). (c) CMRA micrographs for flow patterns generated from 0.5 mL/min flow rates at channels 1-4 (left micrograph), channels 5-8 (middle micrograph), and channels 9-12 (right micrograph). . . .	71
4.1	Example of ANN Control Loop Algorithms for Tissue Optimization.	Outer control loop is cell density control loop with target set to maximal density. Output from density loop sets target for inner control loop which is flow pattern control loop. Each iteration progressively gets closer to target due to automated adjustment. Inputs for both cell density and flow pattern is measured via MRI.	73

LIST OF TABLES

2.1	ECM Hydrogel Compositions.	26
2.2	Final ECM Concentration	26
2.3	Gel Permeabilities	40

ACKNOWLEDGMENTS

I would like to thank my mentor, Dr. Louis-Serge Bouchard for his guidance and provision of resources on this project. I would also like to thank my committee members, Dr. Song Li, Dr. William M. Gelbart, and Dr. Tzung Hsiai for their advice. I would also like to thank Brian Archer, my former mentor and colleague, for his guidance and education on the project. Gratitude is also expressed to my colleagues who have assisted on the project: Jake Inzalaco, Ivana Erlandsen, Samuel Peng, and Julian Tran. Finally, I would like to thank my family and friends who have supported me through my journey.

Copyrighted Materials: The body chapters of this thesis is adapted from a publication manuscript being worked on by me. Therefore, some portions from Chapter 2 that are in the manuscript were not independently done and are adapted from Brian Archer's thesis [5], who was a former colleague, with permission where a description of the bioreactor design and operation was also provided since the same bioreactor was used. Most of the MRI flow map and scaffold design work and associated materials and methods, results, mathematical analysis, and discussion in Chapter 2 were completed in [5] and reused verbatim. Such portions were still approved for inclusion to provide continuity and a complete picture on this thesis project.

CHAPTER 1

Introduction

1.1 Tissue Engineering

Tissue engineering (TE) has seen an emergence in the past three decades due to its potential of fabricating biological substitutes that mimic native tissue [6]. Such an approach could prove to be valuable in the medical field where it could be used as a therapeutic to repair tissue damage from diseases such as diabetic ulcers [7], trauma and burns [8], or it could be utilized to address the organ shortage crisis by regenerating whole organs for use [9]. While tissue engineering has demonstrated regeneration of single targeted tissues [10], the translation of these concepts is limited to only a few FDA-approved dermal and cartilage substitute products [11]. The applicability of tissue engineering for whole organ regeneration is also limited due to the requirement for simultaneous regeneration of multiple cell lineages [10]. The discrepancy between the vast number of engineered tissues from research and the availability of products approved for the market is due to challenges in developing regulatory standards, scaling up manufacturing, and consistently generating properly matured tissue constructs for implantation [11, 12]. Proper maturation characteristically results in a well-distributed, highly dense population of cells within the material as well as a pre-vascular network to anastomose to host tissue if very thick constructs are desired [13]. To achieve this, the formal definition of TE describes utilizing the interdisciplinary application of biological, chemical, and engineering concepts with biomaterial scaffolds, cells, and factors alone or combined to restore or generate tissue [14]. Providing the appropriate environment is essential to achieve maturation for medical applications. As shown in Fig. 1.1, cells, scaffolds, and environment

are the three main components which will be explored further [1].

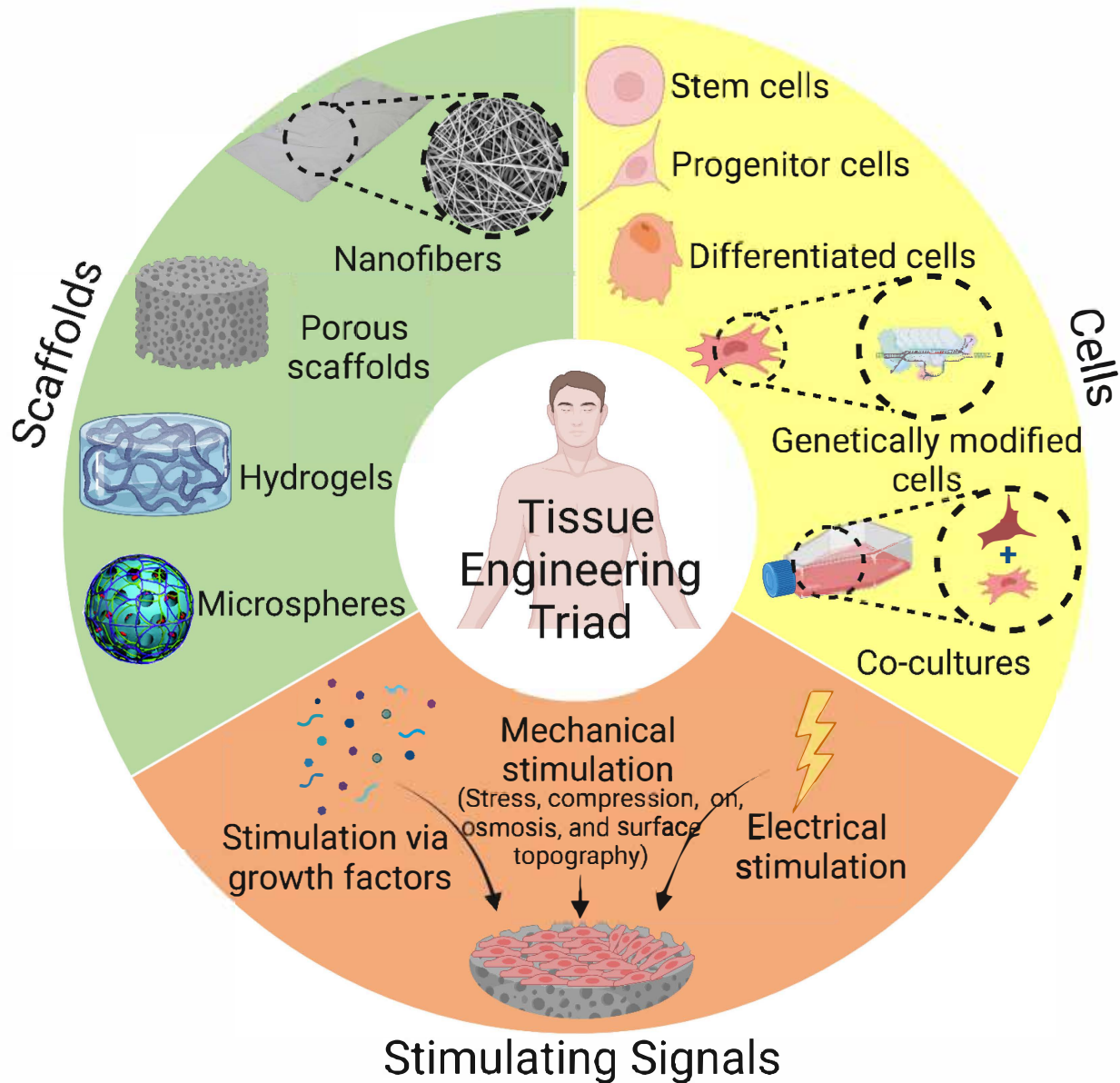


Figure 1.1: **Tissue Engineering Overview.** Graphic illustrates the tissue engineering ‘triad’ where the main components in a tissue model are cells, scaffold, and signaling cues. © 2023 Abdelaziz et al. Adapted from [1] originally distributed under the Creative Commons Attribution License.

1.2 Cells

Cells are the essential, dynamic component for tissue regeneration in tissue engineering. Successful engineered constructs for medical use are reliant on viable, highly populated number of cells of the appropriate cell type within the construct. Because of this, proper cell type selection is vital.

1.2.1 Cell Types

A wide variety of cell types can be selected when recapitulating a specific tissue of interest. Traditionally, tissue engineering has relied on specific differentiated cells from cell lines or primary cells to mimic certain tissues. For example, fibroblasts, melanocytes, and keratinocytes are often utilized for skin tissue culture while cardiomyocytes and human umbilical vein endothelial cells (HUVECs) have been utilized for heart biomimetic cultures [15,16]. While cell lines are convenient and inexpensive, they have failed to properly model human conditions as they often drift genetically from their tissue of origin [17]. The use of primary cells, whether derived autologously (host) or from donors, often better recapitulate human tissue due to retained cellular phenotypic features from their tissue of origin. However, primary cells often also suffer from low proliferation rates and often change phenotypically under senescence which can occur at an early passage. Reproducibility and donor-to-donor variation are also common issues when using primary cells from a specific tissue [18].

As a result of the mixed success obtained from research with cell lines and primary cells, a shift has occurred in the field towards stem cells due to their ability to maintain stemness and differentiate towards one specialized cell type (potency). Previously, the only source of stem cells were human embryonic stem cell (ESC) lines [19] but the discovery of induced pluripotent stem cells (iPSCs) provided another stem cell source where stem cells can be generated directly from differentiated cells by introducing a specific set of genes or chemical reprogramming [20]. iPSCs have been used for tissue engineering, disease modeling, and cell

therapy applications but face some limitations as iPSC-derived cell types can occasionally exhibit immature phenotypes if not provided the appropriate microenvironment. Another type of stem cell used as a cell source are mesenchymal stem cells (MSCs) which are multipotent stem cells often isolated from bone marrow, blood, ligaments, and skeletal muscle [20]. They have the same capabilities as iPSCs but can differentiate toward only osteogenic, chondrogenic, and adipogenic cell types [20]. They have excellent homing capabilities which make them strong candidates for tissue regeneration and wound healing and have become a useful resource due to their ease of use in isolation and differentiation compared to iPSCs [20]. Overall, while stem cells provide greater capabilities in tissue regeneration and control, it also demonstrates the need for a greater understanding on cell signaling cues and subsequent behavior in the *in vivo* environment.

1.2.2 Signaling Cues and Cell Behavior and Development

Cell signals can be generally divided into two categories: 1) biochemical stimuli 2) biophysical stimuli. For biochemical stimuli in tissue, concentration gradients of various biochemical components, nutrients, oxygen, and pH are essential in influencing various cellular processes [21]. Various biomolecules commonly found *in vivo* have different effects on cellular behavior and are integral in supporting cellular growth. Carbohydrates are the main source of energy for cellular metabolism and growth [17]. Blood serum *in vivo* also contains a variety of amino acids or peptides that regulate proliferation and viability, serve as carriers, or promote cell adhesion [17]. Growth factors are also present in blood serum and are involved in cell signaling and communication that mediate processes such as proliferation, differentiation, and tissue maturation [22]. One final common biomolecule in signaling networks is cytokines which are produced by a variety of cells and are involved in differentiation and the immune response [23]. In order to maintain the homeostasis of biochemical concentration gradients by delivering sufficient nutrients and removing waste, it is essential that the proper structures are present. Gradients are regulated by the proximity of vasculature, diffusion in

the ECM, and the metabolic activity of the tissue [21]. Vascular structures are also needed in order to support tissue through sufficient delivery of nutrients and waste removal from interstitial flow [24–26]. Bone tissue *in vivo* for example, often form a complex lacunocanalicular network which provides a circulation of interstitial fluid that transports nutrients and signals and removes waste for osteocytes [27,28].

Besides biochemical cues, tissues also experience a mechanical microenvironment from both intrinsic and extrinsic mechanical cues involving interactions with neighboring cells, the ECM, and blood flow. Fig. 1.2 illustrates both of these mechanical cues and demonstrates the mechanotransduction path where physical forces and cytoskeleton alterations are transduced into biochemical signals downstream that modify cellular behavior (proliferation, shape, and migration) [2,20]. Efforts are focused on understanding the effects of mechanical stimuli on cells, particularly on the effects of fluid shear stresses that various tissues experience. Endothelial cells which experience the highest pressures (1-5 Pa) have been shown to alter cell morphology and orientation which regulates vessel function and remodeling [29]. Another example is epithelial cells where fluid shear stress can affect structure and function and is integral in the formation of microvilli for various tissues, from the intestines [30] to the lungs [31]. Studies have also tried to explore the effects of physical cues on stimulating cells to enhance their characteristics and function. A common strategy is mechanical stretching which has been utilized to control cell growth, gene expression, and differentiation for various functional tissues [32]. Such studies demonstrate the importance in mechanical cues for cellular behavior and tissue maturation.

While the provision of physiological signals (both biochemical and biophysical) are important for tissue development, the spatiotemporal delivery and control of such signals has also been shown to be critical. Both biomechanical and biochemical spatiotemporal signal patterning have been critical in the development of dermal, vascular, cardiac, neural, and craniofacial tissue [33–39], and timed micromechanical signaling has been used to control intercellular interactions [40]. Overall, based on what has been discussed previously, it can

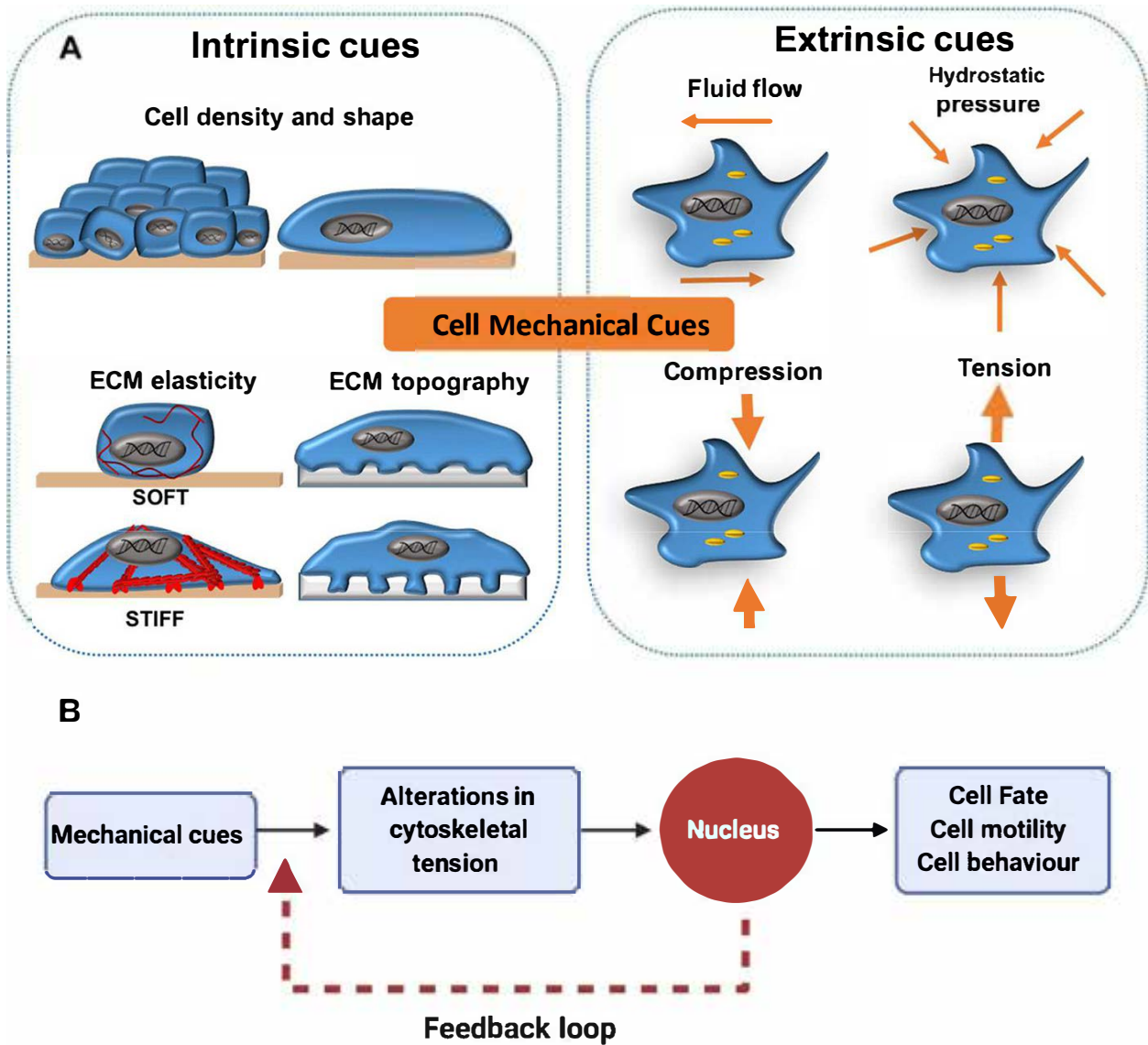


Figure 1.2: **Mechanical Cues and Mechanotransduction.** (A) Graphic illustrates both the intrinsic and extrinsic cues experienced by cells. Extrinsic cues on the right come from shear forces generated from fluid and local (intrinsic) cues come from interactions with cell density, shape, and the extracellular matrix (ECM). (B) Graphic illustrates the mechanotransduction pathway. Mechanical cues alter the cytoskeleton which activates signals downstream into the nucleus which influence cellular behavior. © 2023 Petzold and Gentleman. Adapted from [2]; originally distributed under the Creative Commons Attribution License.

be concluded that two major aspects of the environment are critical to the developmental outcomes of tissue types: 1) the provision and spatiotemporal heterogeneity of physiological signals 2) sufficient delivery of nutrients and removal of waste. Because of the significance of biomechanical signaling and nutrient delivery in tissue engineering, efforts have been made to map spatial variation in extracellular matrix stiffness and flow induced shear at the cellular and tissue scales and to develop culture systems that can support engineered tissue constructs [39, 41–43]. Because of the lack of a vascular network in engineered tissue constructs and the importance of providing nutrients and physiological signals and removing waste, it is essential that the culture platform developed and selected best emulates *in vivo* conditions and provides the proper stimuli and nutrients throughout the whole construct for tissue development.

1.3 Tissue Culture Methods

When it comes to tissue engineering, although culture media often includes biomolecules from *in vivo* environments that stimulate cellular growth and behavior, biochemical stimuli from media alone is insufficient to fully recapitulate what occurs *in vivo* during tissue development. Therefore, the choice in culture platform must also be considered [19]. While replicating the *in vivo* environment as close as possible would be ideal, practical limitations of current tissue culture (TC) technology currently make it impossible to replicate all aspects of the *in vivo* environment. Traditional 2D static culture methods (Petri dishes, flasks, etc.) are popular due to their convenience and ability to efficiently support a monolayer of cells through diffusion as the cells are in continuous contact with the medium [19, 44]. 2D culture methods have made contributions to an understanding on cellular biology. However, such methods fail to translate to medical settings due to being a poor imitation of what occurs *in vivo*, where cells grow in a complex 3D environment that has complex oxygen and nutrient gradients and experience physical cues from blood flow and matrix architecture [19] for development. Cells

under 2D culture conditions lack the complex *in vivo* environmental context which results in cells being excluded from key cell-cell and cell-matrix interactions for cellular processes and constrains them to a flat morphology as a monolayer that is not a natural form of organization [45]. This can be seen in a basic graphic from Fig. 1.3 where cell morphology is flattened as a monolayer in 2D culture while 3D culture allows for the natural morphology of cells as well as distinct cell-cell and cell-matrix interactions not available in 2D.

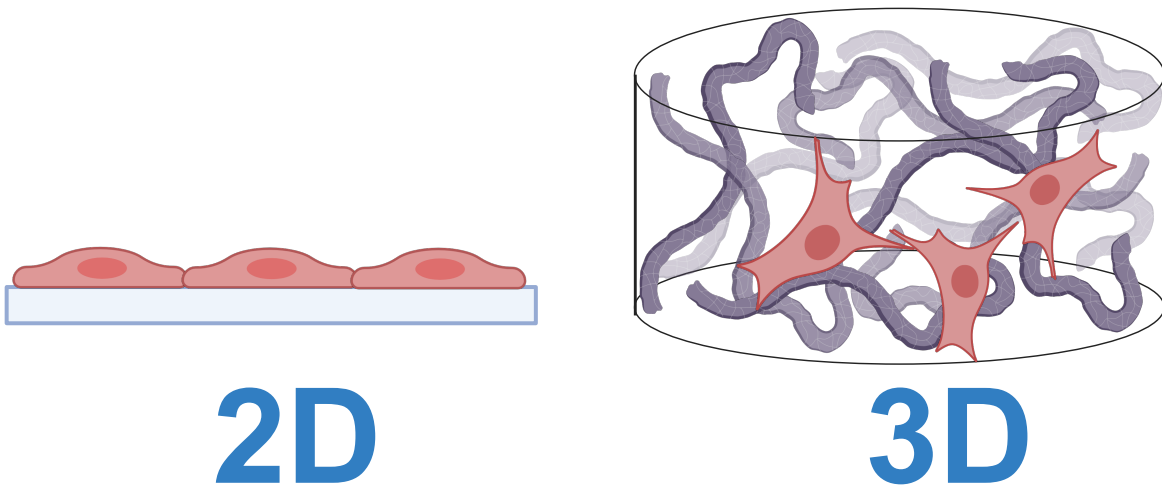


Figure 1.3: **Illustration of 2D vs 3D Culture.** Simple graphic illustrates differences between 2D and 3D culture. Cells are constrained to a flat morphology and limited in cell-cell and cell-matrix interactions in 2D culture while 3D culture provides the ability for expansion to native morphology and interactions.

Such differences are significant as gene expression and the cytoskeleton are altered which can result in a loss of cell phenotype and subsequent behavior and function [46]. As a result, there has been a shift to 3D culture methods in order to provide a tissue microenvironment that enable cells to grow while maintaining their native morphology and function. Scaffold-based tissue engineering is one area of focus for 3D culture where scaffolds are meticulously

designed and utilized in order to replicate the ECM environment by providing signaling cues and promoting key interactions for development. However, scaffolds alone are not sufficient in replicating conditions *in vivo* as the distribution of nutrients, biochemical, and biophysical signals spatiotemporally through flow are also needed for thick tissue construct development. While static culture can potentially support thin 3D tissue scaffold constructs, it is unable to fully support thick tissue constructs (>6 mm scaffolds) as passive diffusion is insufficient in providing nutrients and removing waste of cells at the core of the construct [26,44]. The complex requirements to support thick viable constructs have driven the development of bioreactors that better mimic the *in vivo* environment [47]. Therefore, it can be seen that two main areas are being considered and focused on as the transition to 3D culture methods occur in tissue engineering: 1) scaffold design 2) bioreactor culture. Both areas will be discussed in detail below.

1.3.1 Scaffold Design

Scaffold-based approaches formally is described as utilizing natural or synthetic materials to provide support in the form of a matrix that creates the desired tissue-specific microenvironment for optimal cell growth and natural ECM deposition, while preserving the native tissue architecture [45]. The type of scaffold and their properties are important parameters to consider during tissue development. There are two common types of natural material scaffolds: biopolymer hydrogels and macroporous sponges. Biopolymer hydrogels referred to in this study are water swollen matrices composed of a mixture of several types of randomly oriented, physically crosslinked extracellular matrix (ECM) protein fibers and often have pores smaller than cells [48]. Macroporous sponges refer to materials containing large (>10 μm) pores separated by thin walls, which are synthesized by lyophilizing hydrogels [49, 50]. The properties from scaffolds can have major effects during culture and should be considered. Macro-scale topology, pore geometry, and fluid permeability can influence culture flow patterns by allowing some quantity of interstitial flow [51–54]. Fluid permeability also depends

on several scaffold properties including porosity (total void fraction), pore interconnectivity, and size distribution [55–60]. The scaffold’s mechanical durability or resistance to shear induced erosion and compression, which depends on the microarchitecture and stiffness of the scaffold, are also important properties to consider [61–63]. While biopolymer hydrogels are often soft and preferred for soft tissue models [19], subjecting certain biopolymer hydrogels to perfusion or flow can result in scaffold deformation and degradation on time scales much shorter than what is required for tissue development. Without channels to accommodate flow, the low hydraulic conductivity of the gel causes a pressure differential to form across the gel that results in gel compression. Even with channels present, erosion at the channel wall occurs on a time scale of hours [43]. Such results demonstrate the importance of scaffold type and composition used as some scaffolds cannot be supported with bioreactor culture. Scaffold structural properties can also influence cell behavior depending on the cell type of interest [64–68]. Pore size can have a significant impact on migration for interactions and is dependent on ECM concentration and type and ratios of individual ECM proteins. Pore size has also been shown to regulate mesenchymal stem cell fate where smaller pore sizes maintain stemness and larger pore sizes improves differentiation and osteogenesis for maturation as seen in Fig. 1.4.

For hydrogels, Matrigel[®] at 50% concentration and hydrogels comprised of similar biopolymer mixtures have an average pore size of 2-3 μm [64, 69]. Collagen hydrogels have mesh size distributions in which most pores are close to a few microns [70]. The average pore size in a 2 $\text{mg}\cdot\text{mL}^{-1}$ collagen gel is 7.4 μm whereas the average pore size in a 2 $\text{mg}\cdot\text{mL}^{-1}$ fibrin gel is 0.6 μm [71]. These pore size distributions are optimal for cell migration through the matrix [71]. Unlike the mesh features within biopolymer hydrogels, which are smaller than the diameter of most cells, the pores from porous sponges are much larger than individual cells, greatly altering how cells can move in 3D space. The pore walls from large pores are only a few microns thick, which limits cells to movement along pore wall surfaces and struts [72]. Despite the fact that the porous features within macroporous sponges are one

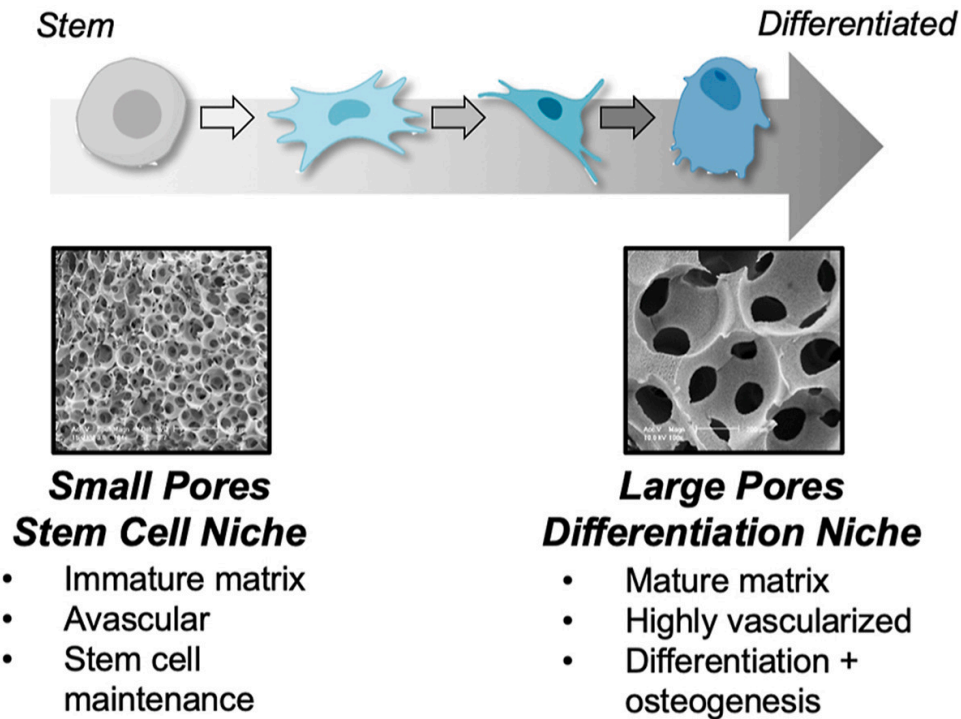


Figure 1.4: **Pore Size Effects on Mesenchymal Stem Cell Fate.** Graphic illustrates how different pore sizes can influence mesenchymal stem cells to either differentiate or maintain stemness. Adapted from [3] with permission, © Elsevier Ltd. 2021

to two orders of magnitude larger than in biopolymer hydrogels, the pore size and scaffold architecture of macroporous sponges impact cell migration to a similar degree as biopolymer hydrogels [64,66,72]. Besides pore size, other properties can be adjusted with attachments or remodeling to provide signaling molecules or growth factors or adjust shape and roughness in order to further guide tissue maturation [73]. In conclusion, it can be seen that the scaffold utilized is essential for tissue development as the scaffold serves as a synthetic ECM that is meant to best provide cells the appropriate framework for appropriate cell behavior and interactions through biophysical cues. However, scaffold choice and selection alone cannot be the only factor for specific thick tissue development. The need for a better reproduction of the *in vivo* microenvironment that overcomes the diffusion limit and couples delivery of biochemical and mechanical cues with spatiotemporal control cannot be achieved with static

culture alone which demonstrates the importance in considering sophisticated bioreactor systems.

1.3.2 Bioreactor Culture Systems

As mentioned, static culture cannot sufficiently support thick tissue scaffold constructs as diffusion is limited in providing nutrients and removing waste throughout the whole construct [26, 44]. Inhomogeneous distribution of viable cells will result in changes in behavior to cells in the middle of the scaffold compared to those closer to the tissue surface which would result in non-uniform cell proliferation, viability, and matrix deposition and eventually, inhomogeneous tissue formation [74]. As a result, efforts have focused on developing culture platforms that can better mimic the native spatiotemporal variation of signals and maintain the homeostasis of nutrient delivery and waste removal for thick tissue development which could help with obtaining a better understanding on *in vivo* conditions and eventually provide better flexibility and control on cell function and fate for tissue development [75]. Bioreactors are designed to serve such a purpose. Formally, they are defined as devices that are designed to mimic the appropriate native environment for cells using biochemical and biomechanical signals as well as provide nutrients and remove waste beyond the rates of the diffusion limit [47].

Many bioreactor designs have been developed, from spinner flasks [76] to rotational-walled [77] and perfusion bioreactors [4]. While rotational or spinner flask bioreactors can increase the convection of media along the external surface of the scaffold, this does not guarantee sufficient chemotransportation within the core of the scaffold interior as most of the media circumnavigates the scaffold [78]. As a result, perfusion bioreactors are often more popular as they address the internal requirement for medium flow within the core of a thick scaffold [26]. Such engineering parameters on mass transfer and shear stress are shown in Fig. 1.5.

Perfusion maintains nutrient and waste homeostasis *in vitro* and mechanically conditions

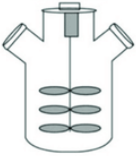


Bioreactor Type	Description	Mechanism of Transfer	Stress	Usage	Tissue Type	Other Considerations
Static Bioreactor						
	Batch culture with no flow of nutrient	Diffusion (high)	Very low	Cell proliferation	—	Homogeneous structure of cell constructs and nutrient diffusion limitations
	Rotating at a speed so the constructs in the reactor are maintained "stationary" in a state of continuous free fall	Convection (high)	Low	Tissue constructs that need dynamic laminar flow	Cartilage, bone and skin	Operating conditions (e.g., speed of rotating) especially for growing large tissue mass
	Flow of medium over or through a cell population or bed of cells	Convection (moderate) and diffusion (high)	Moderate	Tissues that are physicochemically and environmentally relevant to human tissues	Epithelial cells, intestines, bone, cartilage, and arteries	Seeding and attachment of human cells especially within the scaffold body

Figure 1.5: **Engineering Parameters for Different Bioreactors.** Figure illustrates different engineering parameters for different, common bioreactor types. © 2013 Nasim Salehi-Nik et al. Adapted from [4]; originally distributed under the Creative Commons Attribution License.

artificial tissues to maturation with fluid-induced shear forces. Despite advancements with bioreactor designs, there has been limited success in translatability with cell-based tissue grafts which could be attributed to a lack of standardization, challenges with scaling up to a manufacturing scale, and reproducibility issues [11, 12]. All of these challenges suggest a lack of understanding of the effects of the complex flow culture environment on engineered tissue development. This complex, spatiotemporal patterning of physiological signals must be understood and controlled in order to guide engineered tissues through multistage developmental processes. To investigate the effects of a broad dynamic range of heterogeneous fluid-induced shear patterns on three-dimensional (3D) cell culture and engineered tissue development, we created a novel 12 channel perfusion bioreactor (4 channels in each direc-

tion) that improves on the original 10 channel design [79]. The new design maintains magnetic resonance imaging (MRI) compatibility and the ability to generate arbitrary flow patterns from multiple inlets. The ability to monitor and control fluid-induced shear forces noninvasively in thick, optically opaque media make this bioreactor design ideally suited for studying the influence of varied spatiotemporal biomechanical signaling on engineered tissue development. Therefore, the goal of this work is to first evaluate the ability of this new bioreactor in maintaining long term culture for thick tissue construct development and subsequently demonstrate its potential in determining the effects of arbitrary flow patterns on tissue development. Chapter 2 will provide the design, operation, and maintenance protocol of the bioreactor as well as results on different scaffolds (hydrogels, sponges) that are compatible or even optimal for long-term culture with our perfusion system. Chapter 3 will present the results from thick tissue culture experiments under perfusion flow and static conditions over a period of time. Results will show feasibility of our bioreactor in supporting thick tissue constructs as well as present preliminary work on the effects of different flow patterns on tissue development.

CHAPTER 2

Design, Operation, and Maintenance of Custom Twelve-Channel Bioreactor

Because of the importance of the spatiotemporal patterning of biomechanical signals in guiding engineered tissue development, many bioreactors with unique, complex functionalities have been developed to better understand the *in vivo* environment for development. However, due to limitations in technology in observing the complex flow environment in a bioreactor, many studies have relied on computational fluid dynamics (CFD) simulations or modeling [80, 81]. These models are able to predict approximate or rough estimates of the mechanical environment over time, but high levels of variation introduced by biological processes suggest that, for individual experiments, modeled predictions are not necessarily sufficient. Therefore, real time measurements of complex flow patterns are required, but to our knowledge, these have not been obtained in 3D thick, optically opaque environments, which are typical properties of thick tissue constructs. A 10-channel bioreactor design was developed at the time with the ability to monitor and control fluid-induced shear forces non-invasively in thick, optically opaque media using MRI flow maps and multiple inlet flow rate control capabilities [79]. As a result, this design was ideally suited for studying the influence of varied spatiotemporal flow patterns in perfusion culture on engineered tissue development. However, little had been done to investigate the compatibility of various tissue engineering (TE) scaffolds with this type of bioreactor and its ability to finely control fluid induced shear distributions within various scaffold types. Equally as important is that no work had been done on determining whether such a bioreactor could support thick, viable tissue constructs.

The custom-designed 12 inlet bioreactor proposed here is based on the original 10-channel bioreactor design. The new design maintains micro magnetic resonance imaging (MRI) compatibility and the ability to generate arbitrary flow patterns. Two additional inlets in the bioreactor provided 2 additional degrees of freedom over the 10-channels, allowing for finer tuned control over flow patterns. MRI compatibility enabled mapping of flow patterns during culture in real time. The design also features a modular, removable tissue culture (TC) chamber to accommodate the use of a wider range of scaffold types including the macroporous sponges and biopolymer hydrogels and allowed for the implementation of macro-scale modifications to scaffolds (such as the inclusion of open flow channels within the scaffold) prior to cell seeding which can further influence flow patterns [82]. In this chapter, the design, operation, and maintenance of this novel bioreactor was presented. The new bioreactor design was also evaluated for its ability to maintain several types of tissue engineering scaffolds in long term perfusion cell culture. Commercially available porous scaffolds were evaluated for compatibility with continuous, patterned perfusion for periods of up to two weeks and for their ability to promote desirable cell behaviors during culture such as migration and proliferation. The commercially available Ultrafoam™ collagen sponge used in this study has a pore size range of 100-200 μm [83], whereas the gelatin based ® sponges (Gelfoam, Surgifoam) have a pore size range of 30-700 μm [84]. An alginate-RGD macroporous scaffold with an average pore size of 100 μm was also prepared according to protocols established previously [85]. Additionally, biopolymer hydrogels with several unique ECM compositions were similarly evaluated. Scaffolds that best balanced mechanical durability (resisted wear for up to two weeks) and stiffness (supported channel architecture) with relevant levels of cell migration and proliferation was also determined and utilized in subsequent cell culture experiments in the next chapter.

2.1 Materials and methods

2.1.1 Bioreactor Body Design

The bioreactor body was designed using Autodesk Inventor and was subsequently fabricated and 3D printed using a United States Pharmacopeia (USP) Class VI biocompatible stereolithographic resin (Formlabs, Dental SG Resin). Additive manufacturing allowed for the fabrication of intricate geometries. Stereolithography allowed for the production of high-resolution parts. The resin used was both biocompatible and autoclavable, making it suitable for cell culture applications.

Renderings of the bioreactor body from multiple angles are shown in Fig. 2.1. The bioreactor end was cylindrical, allowing the bioreactor to be vertically aligned within an MRI probe. The middle of the bioreactor was a 0.3-inch-thick flat plate centered on the cylindrical axis of the MRI probe. A tapered square hole where the Tissue Culture (TC) chamber sits, is passed through the center of the flat plate. The design of the TC chamber will also be discussed below. Four inlets surrounded each side of the TC chamber hole, allowing perfusion flow from different directions of the scaffold. Grooves for o-rings surrounded the hole on both faces of the plate. O-rings were utilized to seal removable polycarbonate on both bioreactor faces to contain the internal flow path. The windows were mounted with polyether ether ketone (PEEK) screws and nuts that threaded into holes built directly in the body of the bioreactor. The windows provided high sample visibility overall. The top of the bioreactor also had $\frac{1}{4}$ -28 threaded holes manufactured directly in the bioreactor's base which allowed for twelve 0.125 inch outer diameter (OD) polytetrafluoroethylene (PTFE) tubes to be attached to the bioreactor using flat bottom, nut and ferrule fittings. These tubes would eventually feed culture media into the bioreactor as these holes directly fed into the twelve inlet channels that directed flow from the cylindrical end of the bioreactor into three sides of the TC chamber.

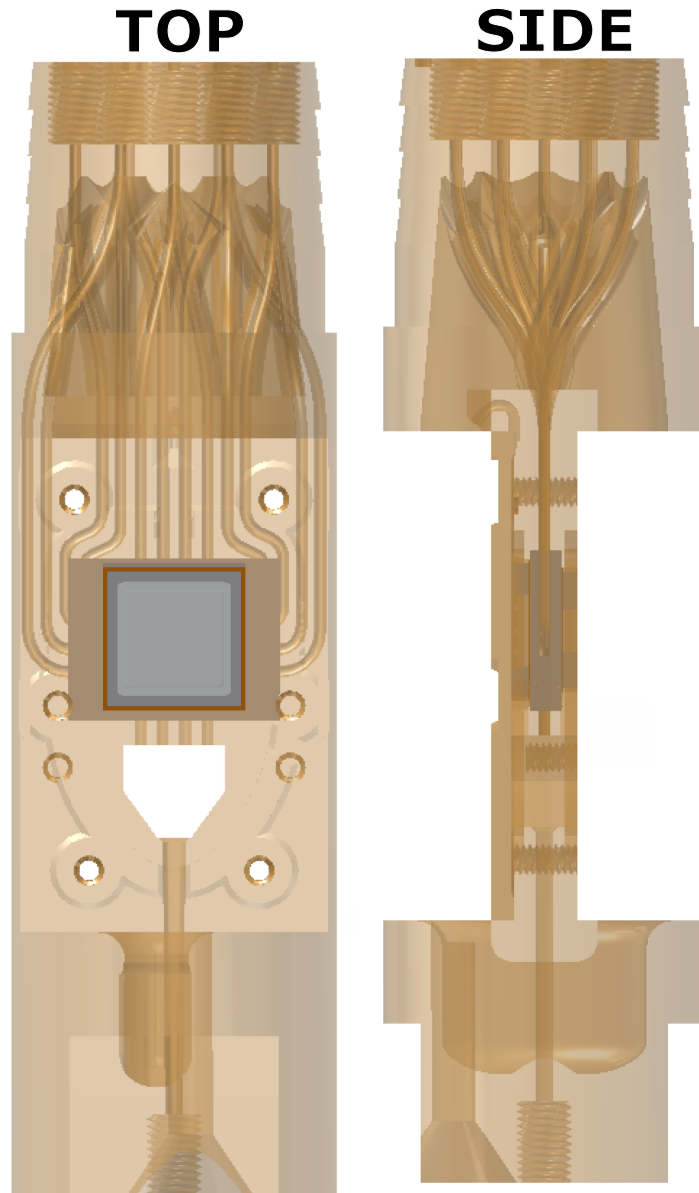


Figure 2.1: **Bioreactor Design.** 3D models of the side and front of the bioreactor.

2.1.2 TC Chamber Design

Figure 2.2 provides renderings of the TC chamber. Rather than place a scaffold (sponge, gel) in the bioreactor directly, a separate insert known as the TC chamber was developed to give more control on scaffold preparation. Made with Dental SG Resin, the TC chamber was a 7

mm tall retaining wall surrounding an empty 1.2 cm x 1.2 cm square shaped region in which the tissue engineering scaffold was contained. Four holes were on each side of the chamber and aligned with the bioreactor inlets. The outside of the TC chamber was angled to sit within the tapered bioreactor hole. Four hooked prongs extended below the corners of the TC chamber to seat a quartz window that served as a flat base for the scaffold. Four corner prongs extended above the TC chamber where a larger quartz window was placed. The windows created well defined geometric boundaries for the TC chamber and provided extra mechanical support for gels cast in the chamber by serving as an additional rigid surface.

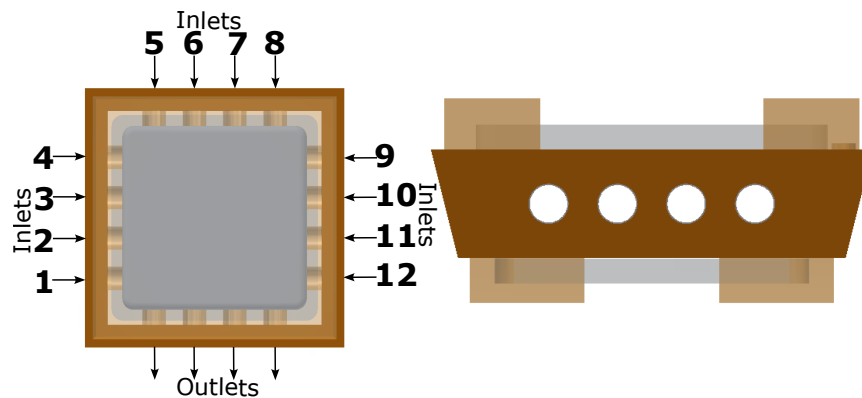


Figure 2.2: **Bioreactor Design.** 3D models of the top and side of the TC chamber. Inlet and outlet directions are labeled.

In order to prevent liquid from circumventing the perfusion flow path through the scaffold's channels, a silicone gasket was created to seal between the walls of the TC chamber and bioreactor. It was cast from food grade liquid silicone (Make Your Own Molds, CopyFlex®) in a stereolithographic mold (Formlabs, Clear Resin). Fig. 2.3 demonstrates how casting was done for the gasket. Stainless Steel tubes were positioned during casting to create channels in the silicone gasket that aligned with the bioreactor inlets while a syringe and needle were used to inject the liquid silicone into the mold. Silicone gaskets were cured for eight hours. The cured gaskets were removed from the mold and soaked in deionized water for five days at 50°C to leach out toxins. Silicone molds used for static six well plate cultures were found to have no influence on viability, morphology, or cell proliferation after leaching.

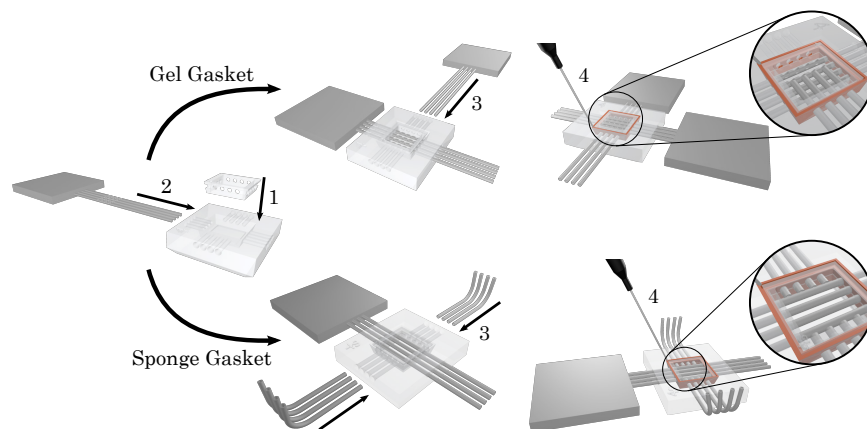


Figure 2.3: **Silicone Gasket Casting.** Workflow diagram of the silicone mold assembly and casting for sponges and biopolymer gels. A magnified view of the last step highlights how metal tubing was aligned. Adapted from [5] with permission, © Brian Archer 2021

2.1.3 Bioreactor System Setup

2.1.3.1 System Assembly

Figure 2.4 provides a schematic of how the bioreactor with the TC chamber was assembled as well as a photograph of the full assembly below the schematic. With the bottom polycarbonate window in place, the TC chamber was placed into the tapered hole in the center of the bioreactor. The TC chamber has quartz windows at the top and bottom to encase the scaffold that would be placed. A silicone gasket also surrounds the TC chamber to ensure no bypass of flow around the scaffold which can be seen in the photograph. PEEK screws and nuts are then utilized to place the top polycarbonate window which seals the chamber. An o-ring ensures a proper seal occurs which is also indicated in the photograph.

Figure 2.5 provides a full view of the fully assembled bioreactor system using photographs. The first half shown with the left photograph provides a view of the valve actuators, flow control valves, pulsation dampener, bubble trap, flowmeters, waste reservoir, peristaltic pump, gas mixer, temperature control console, and pressure relief. The second half shown on the right image has the flow control computer, bioreactor body, total flow flowmeter, Back Pres-

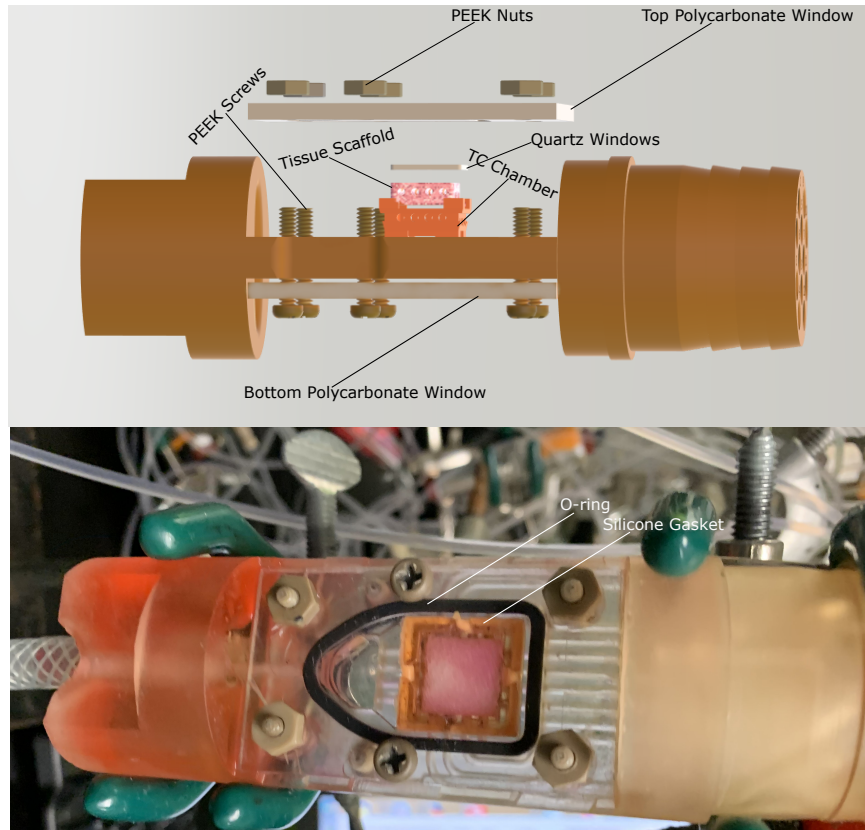


Figure 2.4: **Bioreactor Body Assembly.** Top of the figure shows schematic of full assembly of bioreactor with scaffold and TC chamber. Bottom figure shows photograph of fully assembled bioreactor body.

sure (BP) regulator, humidifier, heating jacket, and media reservoir in view. The flow control computer is where flow rates are inputted in MATLAB. The peristaltic pump pumps the media throughout the whole system. The total flow flowmeter measures the total flow overall towards the bioreactor. Individual flowmeters measure flow rates in each of the 12 tubes that bring media towards the bioreactor body. These measurements communicate with the flow control computer with an Arduino. If adjustments are needed to match individual flow rate measurements with the inputted flow rates in the computer, valve actuators, flow control valves, and the peristaltic pump are automatically controlled and adjusted electronically until such parameters match. The pulsation dampener trapped a volume of air which cyclically compressed to dampen pressure spikes from peristaltic pumps. The BP regulator maintains

inlet pressure upstream. The pressure relief valve ensures pressures do not exceed 40 PSI within the system. Bubble trap minimizes bubbles within the system. Finally, the gas mixer ensures 5% CO₂ is maintained during culture while the temperature control console ensures 37°C is maintained. A closer view of both features is shown in Fig 2.6. The gas mixer in Fig 2.6 (a) is the 2GF-mixer from Oko-labs which mixes air and CO₂ flow rates to maintain 5% CO₂. The temperature control system was engineered by Belilove Company-Engineers and is shown in Fig 2.6 (b)-(c). The pipe heater is shown in (b) while the temperature control console is shown in (c). Media is kept warm through convection with the flow of heated air. The temperature control console provides heat to the stainless-steel pipe heater which heats up the air that flows through it. Temperature of the air flow and the environment are measured using thermocouples and the console provides heat to heat the flow of air until it matches the desired temperature, in this case 37°C. A heating jacket made of styrofoam covers the inlet tubes leading up to the bioreactor to ensure media is warmed before arrival.



Figure 2.5: **Bioreactor System Setup.** Full view of the system setup. Each photo comprises a half of the system.

2.1.3.2 Bioreactor Flow Paths

A process flow diagram (PFD) detailing the bioreactor flow setup is presented in Fig. 2.7.

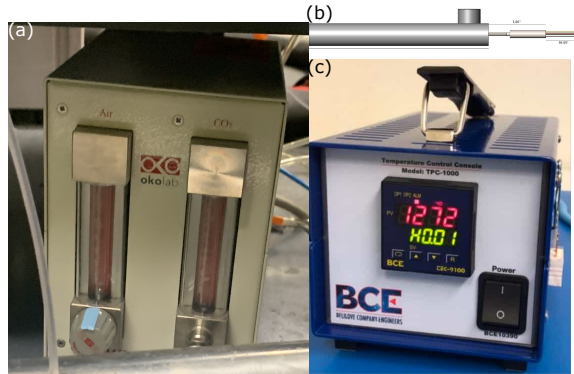


Figure 2.6: **Temperature and Gas Control Components.** (a) Photograph of 2GF-mixer from Oko-labs which was used to maintain 5% CO₂. (b) Steel pipe heater design used to heat the flow of air made from Belilove Company-Engineers. (c) Temperature control console that measures and controls temperature which was also provided from Belilove Company-Engineers.

Primary Flow Path: The primary flow path was a closed circuit where a peristaltic pump circulated cell culture media through the twelve-channel bioreactor. The pump drew media from a reservoir and sent it through two pressure reducing pressure regulators in series that dampened pressure spikes. A digital pressure gauge monitored output from the pump. The media then passed through a bubble trap and then a digital flowmeter measuring the total volumetric flow rate. The path separated into twelve parallel tubes. Each of these tubes included a computer actuated metering valve and digital flowmeter to independently control all bioreactor inlet flow rates. Cell culture media passed through about 25 feet of tubing before entering the bioreactor. The six feet of tubing immediately upstream of the bioreactor were contained in a heating jacket maintained at 37°C to bring cell culture media to body temperature prior to entering the TC chamber. Downstream of the bioreactor the media passed through a back pressure regulator before returning to the reservoir.

Secondary Flow Paths: The manifold through which cell culture media passed prior to returning to the reservoir served as a convergence point for several secondary flow paths. The manifold along with various stopcocks was used to redirect flow through these paths. In order

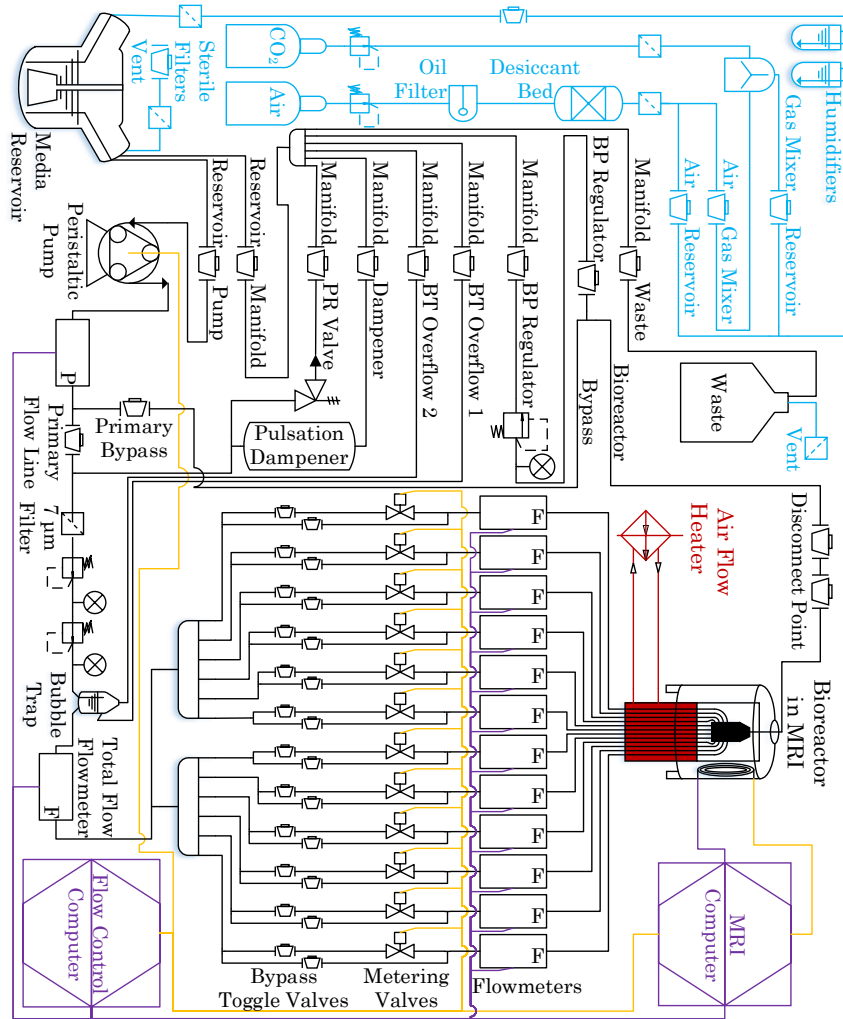


Figure 2.7: **Process Flow Diagram.** Color Legend: Black - cell culture media, blue - gas flow, yellow/purple lines - digital signals generated and received by computer, red - 37°C air flow. Abbreviations: BT - Bubble Trap, PR - Pressure Relief, BP - Back Pressure. Adapted from [5] with permission, © Brian Archer 2021

to prolong the life of the pump tubing (GORE[®] STA-PURE[®]), the pressure downstream of the pump head was prevented from exceeding 40 PSI with a pressure relief valve from a secondary flow path. Media from this valve was returned back to the reservoir. A second flow path involved a large inner diameter tubing called the pulsation dampener. The stopcock was closed for this tube to trap a volume of air which experienced cyclical compressions

that dampened peristaltic induced pressure spikes. One final secondary path involved the bubble trap. The bubble trap was made with two overflow ports (Radnoti) and is part of the primary flow path. The ports usually remain closed during normal operation but can be opened briefly to divert flow and remove buildup of trapped air.

Other Flow Paths: The final flow path involved waste collection to the waste reservoir. A flow line called the primary bypass connected the output of the peristaltic pump to the flow downstream of the bioreactor.

2.1.4 Scaffold Preparation

Two classes of scaffold were prepared for use in the bioreactor: macroporous sponges and hydrogels. In both cases scaffolds were comprised of natural extracellular matrix (ECM) proteins.

2.1.4.1 ECM Hydrogel Mixtures

Hydrogels were cast with a mixture of fibrin, Matrigel[®] (Corning[®]), and rat tail derived type I collagen (Corning[®]). Matrigel[®] is approximately 33% laminin, 60% collagen IV, and 5.4% heparan sulfate [63]. Several hydrogels (Gels 1-4) made from different combinations of ECM proteins were evaluated for their mechanical stability and ability to promote endothelial cell organization. Endothelial cells were used because of their well-established response to flow and shear stress [81, 86–91]. The complete composition of each gel mixture for Gels 1-4 is seen in Table 2.1. Final concentrations of each structural ECM component present in Gels 1-4 are seen in Table 2.2. Fibrinogen and thrombin powders were first sterile filtered with a 0.22 μm pore size membrane. Fibrinogen was then dissolved in Dulbecco's Modified Eagle Medium (DMEM) and kept in a warm bath at 37°C. Thrombin was dissolved at 100 units·mL⁻¹ in 0.1% (w/v) bovine serum albumin (BSA) solution and kept at 4°C.

When preparing gels, collagen solution and NaOH were combined first to neutralize pH

Table 2.1: ECM Hydrogel Compositions.

All Components	Gel 1	Gel 2	Gel 3	Gel 4
	Volumes (μL)			
Collagen ($9.66 \text{ mg}\cdot\text{mL}^{-1}$)	96.34	306	235	241
NaOH (1 M)	4.82	15.31	11.75	11.84
10X DMEM	28.9	28.3	28.5	22.2
FBS	3.85	3.77	3.80	2.96
Thrombin ($100 \text{ units}\cdot\text{mL}^{-1}$)	28.9	28.3	40.0	44.4
Matrigel [®]	48.2	47.2	47.5	37.0
Fibrinogen ($\text{mg}\cdot\text{mL}^{-1}$)	289 (10)	70.7 (25)	133.5 (25)	141.1 (25)

Table 2.2: Final ECM Concentration

ECM Components	Gel 1	Gel 2	Gel 3	Gel 4
Collagen ($\text{mg}\cdot\text{mL}^{-1}$)	1.9	5.9	4.5	4.7
Fibrinogen ($\text{mg}\cdot\text{mL}^{-1}$)	5.8	3.5	6.7	7.0
Matrigel [®] (%)	9.6	9.4	9.5	7.4

and kept on ice to prevent gelation. Fetal bovine serum (FBS), 10X DMEM, Thrombin, and Matrigel[®] were added to the neutralized collagen solution and mixed on ice carefully with a positive displacement pipette to prevent bubbles. While the chilled solution was kept on ice, human aortic endothelial cells (HAECs) were trypsinized and counted. 9×10^5 cells were placed in a tube and pelleted. After aspirating the neutralized trypsin, the pellets were suspended in fibrinogen solution. Fibrinogen cell suspension containing 7.5×10^5 cells was added to the chilled solution and mixed quickly and thoroughly to generate a final cell concentration of $1.5 \times 10^6 \text{ cells}\cdot\text{mL}^{-1}$. Due to low hydraulic conductivity and mechanical strength of natural ECM based hydrogels, open channels in the gel were required to accommodate fluid velocities corresponding to physiologically relevant wall shear stresses ($5\text{-}20 \text{ dyn}\cdot\text{cm}^{-2}$) for endothelial cells [92]. The gel casting chamber was used for this purpose and was designed to align channels with the inlets of the TC chamber using steel tubes. A diagram is shown in Fig. 2.8 The gel was quickly cast with the TC chamber. The chamber was placed in an incubator at 37°C for 30 minutes to anneal. Following gelation, the wells were filled with cell culture media in a 96 well plate to evaluate endothelial cell compatibility with

the scaffold, or the TC chamber was loaded in the bioreactor for flow perfusion compatibility experiments. Gels loaded in the bioreactor did not have cell suspensions and such gels were made by skipping the steps related to cells.

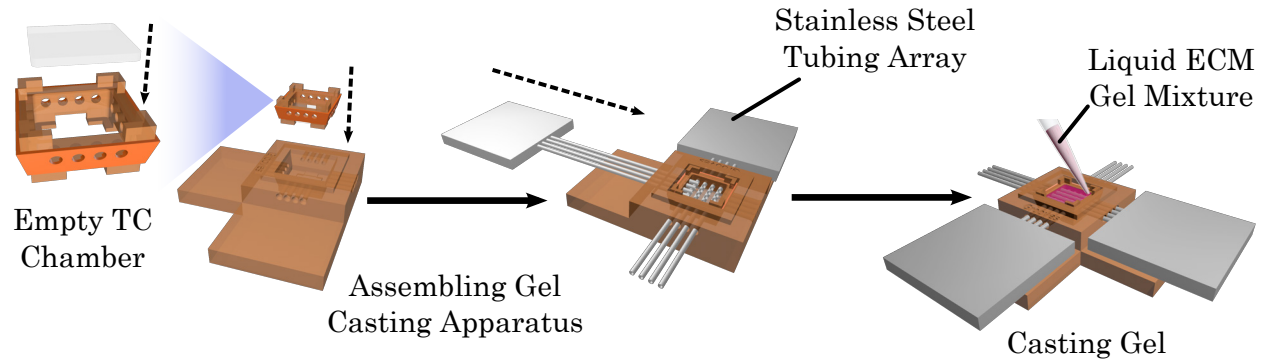


Figure 2.8: **Diagram of the Gel Casting Apparatus.** Diagram demonstrates full assembly and steps taken for gel casting.

2.1.4.2 Porous Sponges

Macroporous sponges evaluated in this study were either collagen (Ultrafoam™) or gelatin (Gelfoam®, Surgifoam®) based. Sponges were cut into blocks with a scalpel blade and discs with a circular biopsy punch. To cut sponges consistently with appropriate dimensions for the TC chamber, scalpel blades were aligned with slits in parts made from Dental SG resin. Dry sponge blocks were adhered to the inner walls of the TC chamber with a nitrocellulose based adhesive film (New-Skin® liquid bandage) to prevent the sponge edges from retracting from the walls of the TC chamber following wetting. Scaffolds not properly anchored to the bioreactor chamber wall (due to initial placement or erosion) result in edge flows in which cell culture media preferentially flows around the scaffold [43,51,93]. Edge flows increase nutrient delivery to cells in the peripheral regions and reduce transport to the interior [51]. After allowing the adhesive to dry for four hours, channels were cut through sponges by focusing a 1500 mW laser tuned to 532 nm through the holes in the sides of the TC chamber. In order to prevent damage to the TC chamber during laser cutting, a slightly smaller channel

diameter of 1.4 mm was used to keep the beam a safe distance. Prior to laser cutting, the TC chamber containing the adhered sponge was sealed in a steam sterilized laser cutting box made from Dental SG. Microscopy coverslips adhered to the sides of the box with a high temperature resistant epoxy allowed light to enter the sponge while preventing microbial contamination during cutting. The box was secured on a stepper motor with a grub screw. The motor was used to rotate the box in 90° increments to allow cutting through all sides of the box. The motor was mounted on a three directional micrometer stage used to position the box beneath the focused laser beam. Sterile filtered (0.22 μm pore size) airflow was directed through the space between the sponge and coverslip to remove smoke particles from the chamber that were generated during the cutting process. A diagram of the laser cutting assembly can be seen in Fig. 2.9.

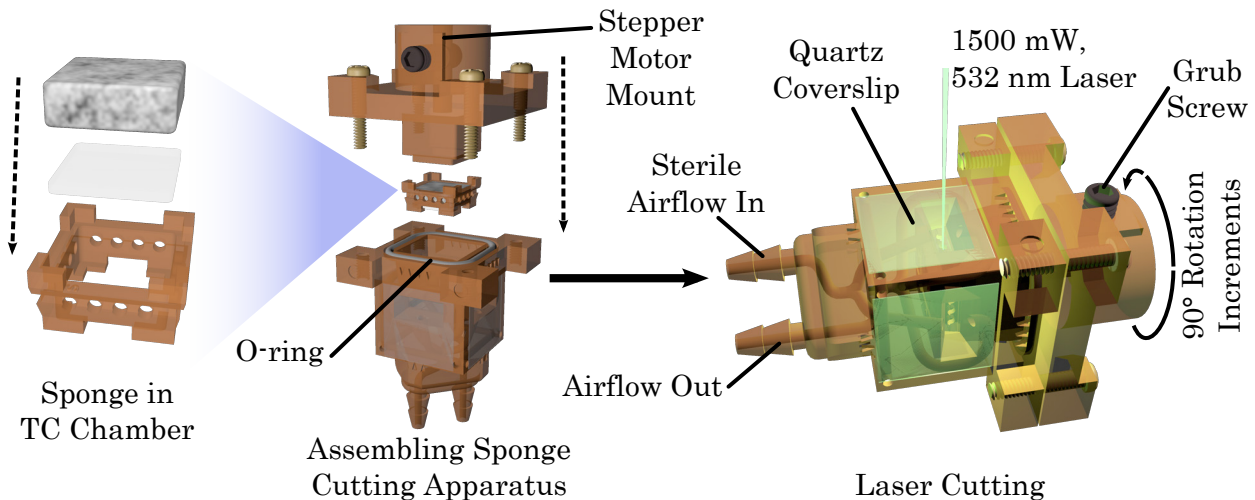


Figure 2.9: **Sponge Laser Cutting Apparatus.** Diagram includes the components and assembly of the apparatus used to contain and position the sponge during laser cutting. Adapted from [5] with permission, © Brian Archer 2021

Following laser cutting, sponges were either placed into the bioreactor to determine their compatibility to perfusion or were seeded by soaking them in cell suspension containing 1.5×10^6 endothelial cells·mL⁻¹ for 2 hours. After seeding, the remaining cell suspension was removed and sponges were placed in a six well plate for static tissue culture to determine

their compatibility for cell growth. Collagen and gelatin sponges were eventually also utilized for 3D cell culture experiments.

2.1.5 Reactor Operation

2.1.5.1 Sterilization

The entire system was sterilized with a specific protocol. First the system was drained of existing cell culture media from a previous experiment. Next the system was primed with deionized water to rinse out any residual cell culture media (proteins in FBS can potentially precipitate out of solution and clog filters and valves). A liquid removal cycle was used to drain the system of the water. Once emptied, the waste reservoir was emptied, all parts of the setup were primed with sterilants (70% ethanol and 7.5% hydrogen peroxide), making sure all surfaces of tubing were in contact with the sterilant for the necessary amount of time as suggested by the CDC [94]. A sterilant used for priming was rinsed with copious amounts of sterile deionized water to ensure any residual sterilant was flushed before priming with another sterilant. Water with catalase was also used as a wash for hydrogen peroxide to ensure elimination of residual hydrogen peroxide and a hydrogen peroxide indicator was utilized to ensure a proper flush occurred [95]. In addition to priming the internal volume of the system with sterilants, two external regions of the system outside of the sealed flow path were flushed with sterilant due to the potential for them to experience brief contact with cell culture media at specific points of operation. These two regions include the space in between the top bioreactor window and the bioreactor body and the disconnect point. After ensuring a proper flush of sterilants, the tubing was dried with pressurized air. Any dry, sterilized tube fitting was covered with a sterile Polyvent filter cap on the open fitting to prevent any microbes in the air from re-entering. Other parts were autoclaved if they were compatible and UV sterilized with a UV-C chamber if they can be exposed directly to the light. Chlorine dioxide, which is a potent but relatively safe disinfectant that is used for

drinking water, was also utilized for sterilization at the media reservoir at a concentration of 0.05 ppm which was found to be effective for antimicrobial activity yet still suitable for mammalian cells [96].

2.1.5.2 Bioreactor Experiment Initialization

Tissue Culture Preparation: The system was primed with 500 mL of cell culture media using a modified liquid priming cycle. **Sample Loading:** After preparing the bioreactor system for tissue culture and seeding a scaffold, the bioreactor was clamped horizontally in a HEPA filtered environment so that the inlets and outlets were at a level height. The top window on the bioreactor was removed with sterile tools, and the TC chamber was inserted into the empty bioreactor chamber. The top polycarbonate window was put back in place and tightened with nuts and screws.

Bubble Removal: Once the TC chamber was in place, the bioreactor was oriented vertically with the outlet above the inlets. All inlet flow rates were set to $0.3 \text{ mL}\cdot\text{min}^{-1}$ to push air out of the bioreactor chamber. If bubbles were present in the bioreactor chamber, attempts were done to dislodge them by mechanically agitating the bioreactor. Persistent bubbles were removed by increasing the hydrostatic pressure in the bioreactor with the BP regulator. The pressure increase reduced the size of the trapped bubbles and allowed them to be dislodged. Inlet flow rates were then set to desired values for the experiment once all the bubbles were removed.

2.1.5.3 Flow Controller

Desired individual flow rates for the 12 inlets were inputted and controlled automatically by a MATLAB program that measured each channel's volumetric flow, determined the difference between the measured flow rates and the set points, and adjusted the degree to which the metering valves were opened based on the difference. 12 flow inlets (4 from a particular

direction) surrounding the scaffold provided the capability to generate a variety of arbitrary flow patterns in the tissue culture chamber for perfusion culture by inputting flow rates from different directions.

2.1.5.4 Flow and Shear Maps

A flow-weighted spin echo multi-slice (SEMS) pulse sequence was used to acquire fluid velocity maps within the bioreactor. One image was acquired during perfusion, and another image was acquired while flow was turned off. Each no-flow velocity map was subtracted from its corresponding flow velocity map to account for errors. A map of the magnitude of flow speed was generated from the velocity maps using the equation:

$$\bar{s} = \sqrt{\bar{v}_x^2 + \bar{v}_y^2 + \bar{v}_z^2} \quad (2.1)$$

where \bar{s} is the flow speed magnitude and \bar{v}_x , \bar{v}_y , and \bar{v}_z are the orthogonal components of the velocity measured with MRI, which are measurements of the average velocity throughout the entire slice thickness, Z_{thc} . Shear maps were calculated using:

$$\bar{\gamma} = (\partial_x \bar{v}_y + \partial_y \bar{v}_x) / 2 \quad (2.2)$$

where $\bar{\gamma}$ is the shear rate of a voxel (measured in s^{-1}) and $\partial_x \bar{v}_y$ and $\partial_y \bar{v}_x$ are determined using finite differences. Briefly: given an $m \times n$ matrix, \bar{v}_y , of y direction velocity measurements, the matrix, $\partial_x \bar{v}_y$, of size $m \times (n - 1)$ is generated by taking the differences between all y velocity measurements adjacent to each other along the x direction and dividing them by the width of the voxels in the x direction, dx . This can be expressed as:

$$\partial_x \bar{v}_y|_{i,j} = (\bar{v}_y|_{i,j+1} - \bar{v}_y|_{i,j}) / dx \quad (2.3)$$

where i is an integer from 1 to m representing each row index and j is an integer from 1 to $n - 1$ representing each column index. Similarly, $\partial_y \bar{v}_x$ can be expressed as:

$$\partial_y \bar{v}_x|_{i,j} = (\bar{v}_x|_{i+1,j} - \bar{v}_x|_{i,j}) / dy \quad (2.4)$$

where \bar{v}_x is an $(m - 1) \times n$ matrix comprised of discrete x velocity component measurements, i is the row index from 1 to $m - 1$, j is the column index from 1 to n , and dy is the y direction length of the voxels. Since the two matrices had different dimensions from each other, they were both resized to the original $m \times n$ size using MATLAB's bicubic interpolation function where an output pixel value is a weighted average of pixels in the nearest 4-by-4 neighborhood.

2.2 Results

2.2.1 General Bioreactor Performance

The bioreactor was found to be able to control all twelve flow inputs, reaching steady state flow targets within 3 minutes of starting the program with all valves completely closed as seen in Fig. 2.10. Once the correct valve inputs were found, only minor adjustments were required to maintain steady flow rates over long periods. For temperature, the temperature control console was able to maintain 37°C for long culture periods (weeks). Therefore, our system was capable of generating steady flow patterns and maintaining temperature over the duration of a cell culture experiment.

2.2.2 Scaffold Results Determine Compatible Scaffolds for Culture and Perfusion Flow

Representative confocal fluorescent micrographs of HAECs cultured in each of the four gel compositions for five days can be seen in Fig. 2.11. Multi cellular structures formed in all four gel compositions, but variations in the size, morphology, and abundance of the structures was apparent. The ECM composition of Gel 1, which was based off of previous flow studies [43], resulted in the formation of the largest, most developed structures [89, 91]. However, this gel composition was too fragile to withstand continuous perfusion and was susceptible to

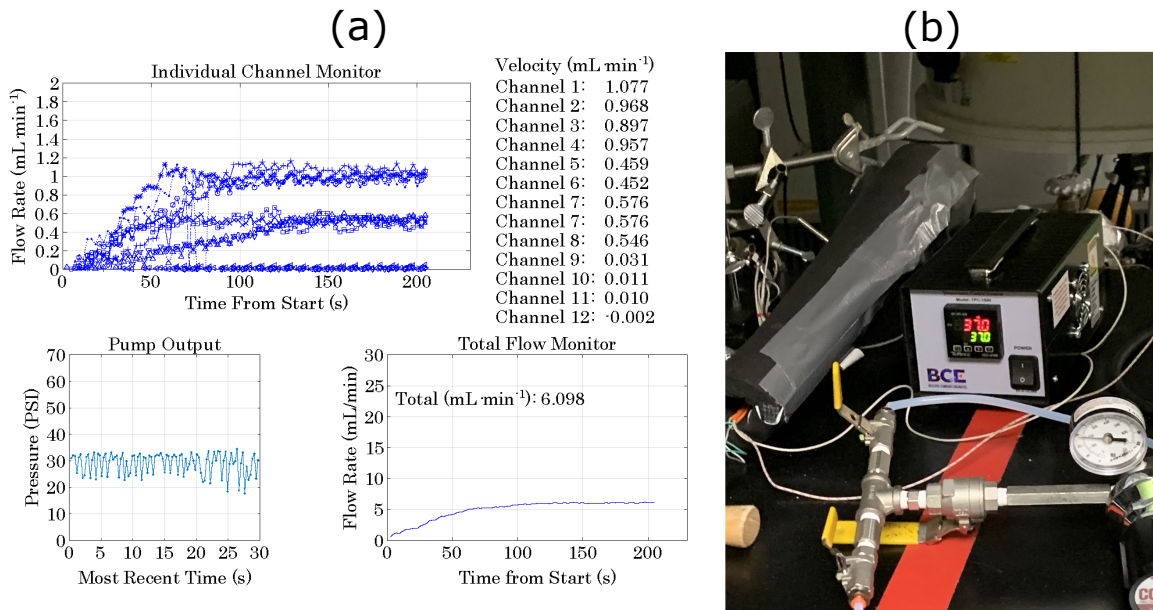


Figure 2.10: **Flow Rate and Temperature Monitors.** Figure shows measurements from flow rate control computer and temperature control console. (a) Flow rate measurements were generated by MATLAB while controlling bioreactor inlet flow rates. Digitally measured parameters related to the bioreactor are plotted over time. Upper plot shows flow rates measured in each of the twelve inlets. Lower left plot shows pressure measured downstream of the peristaltic pump. Lower right plot displays the total flow rate through the bioreactor. Channels 1-4 were set to $1\text{ mL}\cdot\text{min}^{-1}$, channels 5-8 were set to $0.5\text{ mL}\cdot\text{min}^{-1}$, and channels 9-12 were set to $0\text{ mL}\cdot\text{min}^{-1}$. (b) Temperature measurements shown with control console during culture. The red number is the measured value while the green number is the temperature setpoint. Flow rate monitor image and description is originally from [5] with permission, © Brian Archer 2021

shear. Cells cultured in Gels 2 and 3 produced structures similar to each other in size and density. The multicellular structures in Gels 2 and 3 were thinner in average diameter and less interconnected than the structures in Gel 1. However, HAEC structures in Gel 2 appeared to be more similar to those in gel 1 in morphology. The degree of branching and webbing between branches was higher in Gel 2 than in Gel 3. The structures in Gel

3 appeared more linear with less bifurcations and webbing. The structures in Gel 4 were much sparser and smaller in size than in the other three gels. Within the structures in Gel 4, the cell nuclei were more densely packed than in any of the structures seen in other gels. Gel 4 was the most mechanically stiff gel, but its poor suitability for HAEC growth made it unsuitable as a scaffold. Gels 2 and 3 were both able to withstand perfusion in the multi-inlet bioreactor. When cast between quartz windows they were able to maintain distinct channel geometry without collapsing. Despite the potential for further optimization of the biopolymer mixture, Gel 2 seemed most optimal for additional experiments as it provided a sufficient starting point to study neovascularization.

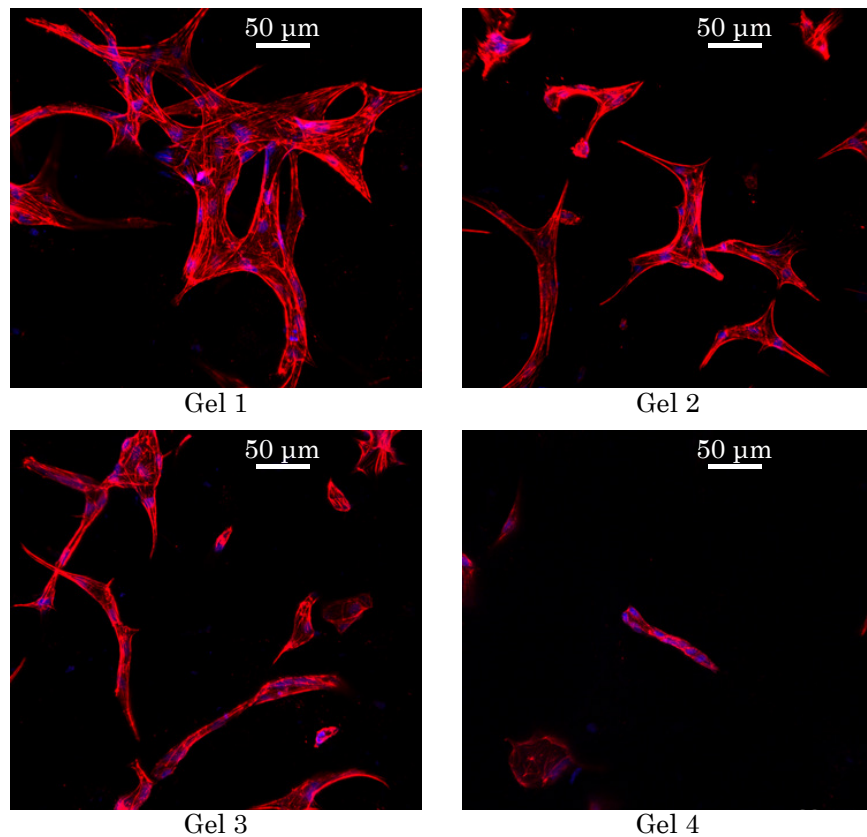


Figure 2.11: **HAEC Static Culture in Biopolymer Gels 1-4.** Confocal images of HAECs cultured statically in each gel composition. Cell nuclei were stained with DAPI (shown in blue) and actin was stained with Texas Red™-X Phalloidin (shown in red). Adapted from [5] with permission, © Brian Archer 2021

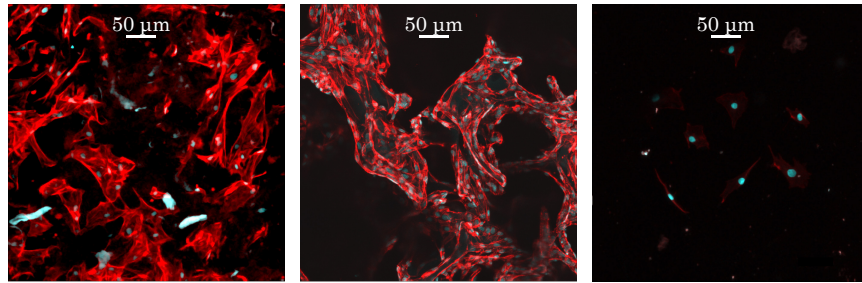


Figure 2.12: **HAEC Static Culture in Macroporous Sponges.** Confocal stacks of HAECs cultured statically in collagen, gelatin, and alginate-RGD sponges from left to right. Cell nuclei were stained with DAPI (shown in blue), and actin was stained with Texas Red™-X Phalloidin (shown in red). Adapted from [5] with permission, © Brian Archer 2021

Representative confocal fluorescent micrographs of HAECs cultured in macroporous sponges are seen in Fig. 2.12. It can be seen that endothelial cells attach, proliferate, and migrate toward each other to form large, multicellular structures blanketing the walls and struts in collagen and gelatin sponges. Despite the fact that cells were able to attach to the alginate-RGD sponge, they did not proliferate into larger numbers, and they maintained randomly scattered positions, which indicated a lack of migration. The pattern of endothelial cell growth in the gelatin sponge highlights the larger pores, which appear as dark regions. Pores in the collagen sponge were smaller and did not dominate large portions of the imaged region. Since the collagen and gelatin sponges promoted endothelial cell growth and were best resistant to flow induced wear for up to two weeks in the bioreactor, they were both considered for 3D cell culture under flow.

2.2.3 Flow Through Scaffolds

Flow maps were obtained using flow-weighted MRI in order to demonstrate not only the capability of monitoring perfusion flow conditions in real time using an MRI-compatible bioreactor, but also demonstrate the various scaffolds and corresponding complex flow patterns that can be supported and measured within the bioreactor for tissue culture.

2.2.3.1 Flow in a Biopolymer Matrix

Adjusting flow inputs into each channel lead to the formation of a wide range of achievable flow patterns throughout the channel grid. Fluid velocity maps were obtained directly from flow-weighted MRI. Velocity maps corresponding to $5 \text{ mL}\cdot\text{min}^{-1}$ flow rates in all input channels are shown in Fig. 2.13. Total flow speed and shear rate maps calculated from the velocity maps are shown in Fig. 2.14.

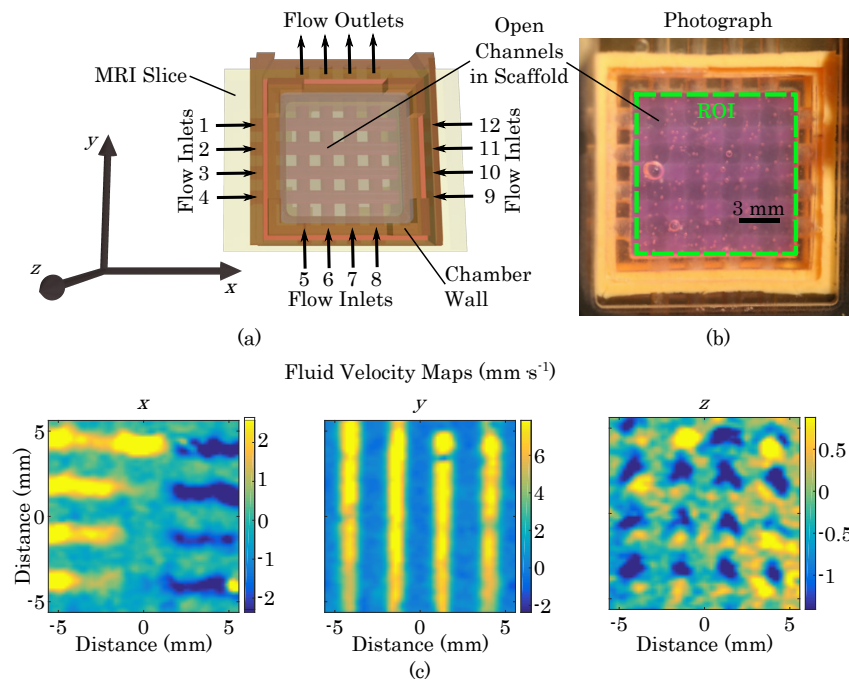


Figure 2.13: **Fluid Velocity Maps in Biopolymer Scaffold.** (a) Diagram of gel scaffold highlighting the pattern of open channels within the gel. Diagram is labelled with channel inlet numbers and the Cartesian coordinate orientation corresponding to all other fluid velocity maps presented. (b) Photograph of biopolymer scaffold mounted in bioreactor. The region of interest (ROI) used when cropping and displaying flow-weighted MRIs is outlined in green. (c) Fluid velocity maps within biopolymer scaffold corresponding to input flow rates of $0.5 \text{ mL}\cdot\text{min}^{-1}$ in all inlet channels. Velocity maps were cropped to include only the scaffold region of the MRI. Values in colorized scale bars are in $\text{mm}\cdot\text{s}^{-1}$. Adapted from [5] with permission, © Brian Archer 2021

The pattern of contrast between regions of high and low flow clearly resembles the geometry of the channels in the gel with higher flow rates corresponding to channel and lower flow rates corresponding to the interstitial space. The x velocity component shows a relatively symmetrical pattern around $x = 0$ with flow rates exceeding $2 \text{ mm}\cdot\text{s}^{-1}$ in opposing directions. A negative z velocity component is visible at each intersection between the vertical and horizontal channels due to the offset of the channels from each other in the z direction. The shear rate map shows that shear rates at the walls of channels with high luminal flow (especially the vertically oriented channels) exceeding 6 s^{-1} , whereas shear rates in the center of these channels were close to 0 s^{-1} . The Reynolds number, Re , at the entrance of each channel where the flow rate was $0.5 \text{ mL}\cdot\text{min}^{-1}$ was $Re=10$, given a channel diameter of 1.5 mm , cell culture media density of $993.37 \text{ kg}\cdot\text{m}^{-3}$, and dynamic viscosity of $6.92 \times 10^{-4} \text{ kg}\cdot\text{m}^{-1}\cdot\text{s}^{-1}$ [97,98]. Assuming the total inlet flow was evenly split between the four outlet channels giving them each a volumetric flow rate of $1.5 \text{ mL}\cdot\text{min}^{-1}$, the Reynolds number increased to $Re=30$ at the exits. Therefore, all flow within the channels was well within the laminar regime, even considering possible variations in the inlet flow distributions.

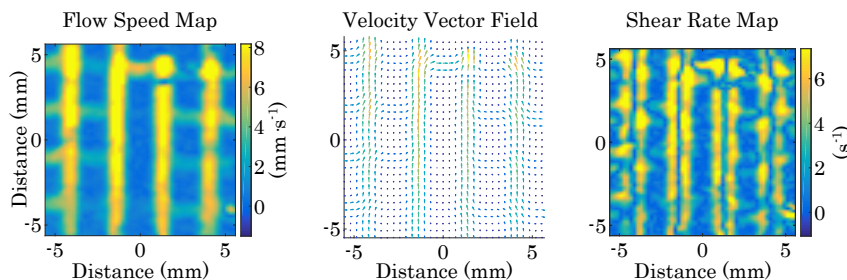


Figure 2.14: **Flow and Shear Maps.** The left is a map of the total flow speed magnitude calculated from the directional fluid velocity maps in Fig. 2.13. The middle plot is a flow vector field determined from x and y fluid velocity maps. The right panel is a shear rate map calculated from the x and y fluid velocity maps. Adapted from [5] with permission, © Brian Archer 2021

To ensure the validity of the flow-weighted MRIs, a model of flow in a cross section of the gel was generated. Given the repetitive geometry of the evenly spaced channels inside

the gel, the model was generated for a unit cell of a cross section of the gel. The unit cell was composed of a single channel and its surrounding matrix. The width of the cell was equal to the distance between channels, 2.74 mm. The height of the cell was equal to the thickness of the gel, 4.32 mm. Given a channel diameter of 1.50 mm, the cross-sectional area of the channel was 1.76 mm², and the cross-sectional area of the surrounding matrix was 10.1 mm². The channel lumen and the interstitial space of the biopolymer matrix were considered parallel flow paths through which liquid could pass. The pressure drop, ΔP , across parallel paths is the same. According to Darcy's law, the pressure drop across a length of matrix is:

$$\Delta P = -\frac{Q_s \mu L}{kA} \quad (2.5)$$

where Q_s is the volumetric flow rate through the matrix, μ is the dynamic viscosity of the liquid, L is the length of the porous medium over which the pressure drop takes place, k is the permeability of the medium in m², and A is the cross-sectional area of the matrix. In the channel's lumen, the pressure drop was determined by the Hagen-Poiseuille law:

$$\Delta P = -\frac{8\mu L Q_c}{\pi R^4} \quad (2.6)$$

where R is the channel radius and Q_c is the volumetric flow rate through the channel. Setting the pressure drops of the lumen and interstitial space equal to each other and solving gives:

$$-\frac{Q_s \mu L}{kA} = -\frac{8\mu L Q_c}{\pi R^4} \quad (2.7)$$

$$Q_s = \frac{8kA_s}{\pi R^4} Q_c \quad (2.8)$$

In order to estimate permeability of gel mixtures, the Happel method [99] modified for porous media comprised of a mixture of rods of varying size was used [63]. Briefly, the permeability, K_h , of a network of randomly distributed, identical rods of type h is determined by the weighted average: $K_h = \frac{2}{3}K_{h,\perp} + \frac{1}{3}K_{h,\parallel}$, where K_{\parallel} is the fluid permeability derived for flow through an array of unidirectional rods in which the flow is parallel to the rod cylinder axis. K_{\perp} is the fluid permeability derived for flow through an array of unidirectional rods in

which the flow is perpendicular to the rod cylinder axis. According to Happel:

$$K_{h,\perp} = \frac{b_h^2}{4} \left[\ln \frac{b_h}{a_h} - \frac{1}{2} \left(\frac{b_h^4 - a_h^4}{b_h^4 + a_h^4} \right) \right] \quad (2.9)$$

$$K_{h,\parallel} = \frac{1}{8b_h^2} \left(4a_h^2 b_h^2 - a_h^4 - 3b_h^4 + 4b_h^4 \ln \frac{b_h}{a_h} \right) \quad (2.10)$$

where a_h is the radius of rod of type h and b_h is the radius of a larger, concentric cylinder making up the unit cell of rod type h . b_h is selected such that the difference, $b_h - a_h = \lambda$, is constant for all fiber sizes and such that the average solid fraction summed over all unit cells is equal to the total solid fraction of fibers in the porous medium. It is found from solving

$$\lambda^2 \left[\sum_h \frac{\phi_h}{a_h^2} \right] + 2\lambda \left[\sum_h \frac{\phi_h}{a_h} \right] + \left[\sum_h \phi_h \right] - 1 = 0 \quad (2.11)$$

where ϕ_h is the volume fraction of each polymer. Once b_h and a_h are obtained, the overall permeability of the porous medium was found from

$$K = \sum_{h=1}^N \left[\frac{n_h}{K_h(b_h, a_h)} \right]^{-1} \quad (2.12)$$

where n_h is the fraction of fibers with radius a_h in a random cross section found using:

$$n_h = \frac{\phi_h / \pi a_h^2}{\sum_h (\phi_h / (\pi a_h^2))}. \quad (2.13)$$

Using this method, permeabilities were calculated for various gel mixtures that are shown in Table 2.3. Matrigel[®] was assumed to be a mixture of 60% type IV collagen, 33% laminin, and 5.4% heparan sulfate [63]. The fiber radii corresponding to type IV collagen, laminin, heparan sulfate, and type I collagen were 0.7 nm [100], 0.6 nm [101], 0.5 nm [102], and 50 nm [103,104]. The volume fractions of each fiber type were determined from $\phi_h = v_h C_h$ where v_h is the partial specific volume of a specific biopolymer and C_h is its concentration. The partial specific volumes of type IV collagen, laminin, and heparan sulfate used were 0.695 mL·g⁻¹ [105–107], 0.73 mL·g⁻¹ [108,109], 0.54 mL·g⁻¹ [110,111]. The partial specific volume of type I collagen was reported to be 0.70 mL·g⁻¹ [112,113], but an effective specific volume

Table 2.3: Gel Permeabilities

Gel Type	Permeability, K (m^2)
Type I Collagen (2 $\text{mg}\cdot\text{mL}^{-1}$)	8.56×10^{-13}
Type I Collagen (4 $\text{mg}\cdot\text{mL}^{-1}$)	3.68×10^{-13}
Type I Collagen (6 $\text{mg}\cdot\text{mL}^{-1}$)	2.21×10^{-13}
Fibrin (from 2 $\text{mg}\cdot\text{mL}^{-1}$ fibrinogen)	5.48×10^{-15}
Fibrin (from 4 $\text{mg}\cdot\text{mL}^{-1}$ fibrinogen)	2.41×10^{-15}
Matrigel (1:10 dilution)	4.29×10^{-16}
Gel 2	4.26×10^{-16}
Gel 1	4.09×10^{-16}
Matrigel, 100%	2.56×10^{-17}

of $1.89 \text{ cm}^3\cdot\text{g}^{-1}$ was also reported, which takes into account intrafibrillar water content [104]. The effective specific volume of $1.89 \text{ cm}^3\cdot\text{g}^{-1}$ did not produce accurate predictions for K in the study in which it was reported. Instead, a more accurate effective specific volume of 1.17 was found from reported volume fractions and corresponding permeabilities reported more recently [103, 114]. The volume fraction of fibrin was determined from the concentration of fibrinogen used according to: $\phi_{fibrin} = \frac{C_{Fbg}}{\rho_{Fbg}\Phi_{int}}$ where ρ_{Fbg} is the density of fibrinogen protein ($1.4 \text{ g}\cdot\text{mL}^{-1}$) and Φ_{int} is the internal solid fraction of a fiber found from the determined relationship $\Phi_{int} = 0.015 \ln(C_{Fbg}) + 0.13$ [115]

Using the Gel 2 fluid permeability estimate of 426 nm^2 , the relationship between Q_s and Q_c became $Q_s = 3.46 \times 10^{-8}Q_c$, suggesting that the interstitial volumetric flow rate through the scaffold was negligible compared to luminal flow through the channels. Since flow-weighted MRIs directly measure fluid velocity, the average fluid velocity in the matrix was compared to the average fluid velocity in the channel using the relationships $Q_c = v_{c,avg}A_c$ and $Q_s = v_{s,avg}A_s$ to give:

$$v_{s,avg}A_s = \frac{8kA_s}{\pi R^4}v_{c,avg}A_c \quad (2.14)$$

$$v_{s,avg} = \frac{8kA_c}{\pi R^4} v_{c,avg} = \frac{8k\pi R^2}{\pi R^4} v_{c,avg} = \frac{8k}{R^2} v_{c,avg} \quad (2.15)$$

The relationship between average fluid velocity in the scaffold versus average fluid velocity in the channel was $v_{s,avg} = 7.16 \times 10^{-11} v_{c,avg}$, demonstrating that any interstitial flow was well below the range of the MRI when the imaging parameters were optimized to encompass intraluminal flow velocities.

Despite the prediction that total flow through the matrix would be significantly lower than flow through the channels, a slip boundary condition and an elevated quantity of flow penetrating the matrix immediately adjacent to the channel wall were expected [116, 117]. According to the Brinkman model, the penetration depth of fluid flow into the matrix was estimated to be on the order of \sqrt{k} [116], or 20.6 nm in the case of gel 2. Since the Brinkman model relies on Darcy's law, which assumes a uniformly homogenous porous material (the length scale of the material \gg the length scale of the pores), James and Davis generated a new model of flow close to the interface on the length scale of the pores. The James and Davis model found that the slip boundary term can safely be ignored in the calculation of wall shear when the solid volume fraction of the porous material is greater than 0.01, and it found that the penetration depth of elevated fluid velocity is less than what was predicted in the Brinkman model [117]. In the case of gel 2, the total solid fraction was estimated to be 0.0246, suggesting that the permeability of the gel and subsurface flow at the channel wall will have no discernable effect on endothelial cells versus an impermeable wall. In comparison to the fluid penetration depth, the height of an endothelial cell nucleus hump when cultured under flow is $1.77 \mu\text{m}$ [118]. The geometry of an endothelial cell monolayer has a greater influence on local shear stress at the channel wall than the permeability of the matrix [119, 120], and even the influence of endothelial cells on shear will be undetectable by MRI given its xy spatial resolution of roughly $100 \mu\text{m}$.

Given the fact that bulk interstitial flow and flow penetration at the wall were negligible, flow through the unit cell cross section of the gel was modelled by considering the channel and

matrix as two distinct regions. In order to validate flow weighted MRIs, flow in the channel was modelled as flow through a pipe, and the surrounding matrix was modelled as static water. Flow in the channel was calculated using the paraboloidal function: $v_y(r_z, r_x) = 2v_{c,avg} \left(1 - \frac{r_z^2}{R^2} - \frac{r_x^2}{R^2}\right)$ where v_y is the y velocity component at a discrete point in 3D space (not averaged over Z_{thc}), r_z is the radial position in the channel along the z axis, and r_x is the radial position in the channel along the x axis. This calculation is valid for fully developed laminar flow. A map of v_y modelled in the unit cell cross section as well as corresponding velocity and shear rate profiles along a one dimensional axis intersecting the center of the channel are displayed in Fig. 2.15 (a). The shear rate profile was determined using finite differences in v_y along the x direction. The shear rate at the wall of the channel in the model determined using finite differences matched the expected wall shear (63 s^{-1}) calculated using

$$\dot{\gamma} = \frac{4Q}{\pi r^3}, \quad (2.16)$$

which is valid for flow in a pipe. $\dot{\gamma}$ is the shear rate at a point in space not averaged over Z_{thc} .

In order to directly compare the modelled flow profiles across a channel to the flow profiles across channels generated by MRI, the z and x resolution of the MRI were taken into account when generating a theoretical flow profile across a channel. The flow-weighted SEMS pulse sequence had a minimum slice thickness (z resolution) of 0.75 mm. Since the channels were 1.5 mm in diameter, a 3D reconstruction of the channels was not feasible with a finely segmented z stack. It was decided to take a single 4 mm thick slice that fully encompassed both sets of channels and the surrounding matrix. The x resolution of the MRI in Fig. 2.12 was $203 \mu\text{m}$. A map of v_y modelled in the unit cell cross section with the same x resolution as the MRI in Fig. 2.13 can be seen in Fig. 2.15 (b). Profiles of \bar{v}_y averaged over the entire 4 mm thick z section and $\bar{\dot{\gamma}}$ calculated from the slice-averaged \bar{v}_y values were plotted along the x direction in the same panel. In order to make the shear rate profile directly comparable to the MRI shear rate profile, the modelled shear rate was calculated using Eq. 2.2, which averages $\partial_x \bar{v}_y$ and $\partial_y \bar{v}_x$. Since the axis of the modelled channel was oriented perpendicularly

to the xz plane, and since it was assumed that the flow was fully developed, $\partial_y \bar{v}_x = 0$, and therefore $\bar{\gamma} = \partial_x \bar{v}_y / 2$. \bar{v}_y and $\bar{\gamma}$ profiles segmented with the corresponding MRI x resolution were plotted in black. Continuous \bar{v}_y and $\bar{\gamma}$ profiles along the x direction were plotted in magenta for comparison. It can be seen that averaging in all liquid within the z slice thickness reduces the apparent maximum flow rate in the center of the channel by approximately a factor of 4. In addition, the parabolic velocity profile has rounded tails near the walls when averaging the entire z slice thickness due to the fact that voxels at the edge of the channel contain more static liquid trapped in the matrix than voxels in the center of the channel. These tails cause the apparent shear rate profile to have two rounded humps rather than a simple linear relationship between radial position and shear rate.

The apparent velocity and shear rate profiles determined via MRI was also analytically solved. To find the average velocity over the entire slice thickness at any point along r_x , the function for \bar{v}_y was integrated with respect to z , keeping r_x constant, and divided by the total slice thickness since the contribution to flow in the matrix is negligible:

$$\bar{v}_y(r_x) = \frac{1}{Z_{thc}} \int_{r_{z_1}}^{r_{z_2}} 2v_{c,avg} \left(1 - \frac{r_z^2}{R^2} - \frac{r_x^2}{R^2} \right) dz \quad (2.17)$$

where the limits r_{z_1} and r_{z_2} are the r_z values at which r_x intersects the channel wall. Solving gives:

$$\begin{aligned} \bar{v}_y(r_x) = \frac{1}{Z_{thc}} & \left(-\frac{2v_{c,avg}}{3R^2} r_{z_2}^3 + 2v_{c,avg} \left(1 - \frac{r_x^2}{R^2} \right) r_{z_2} + \right. \\ & \left. \frac{2v_{c,avg}}{3R^2} r_{z_1}^3 - 2v_{c,avg} \left(1 - \frac{r_x^2}{R^2} \right) r_{z_1} \right) \end{aligned} \quad (2.18)$$

$$\begin{aligned} \bar{v}_y(r_x) = \frac{1}{Z_{thc}} & \left(\frac{2v_{c,avg}}{3R^2} (r_{z_1}^3 - r_{z_2}^3) + \right. \\ & \left. 2v_{c,avg} \left(1 - \frac{r_x^2}{R^2} \right) (r_{z_2} - r_{z_1}) \right) \end{aligned} \quad (2.19)$$

Substituting $r_{z_1} = -\sqrt{R^2 - r_x^2}$ and $r_{z_2} = \sqrt{R^2 - r_x^2}$ gives:

$$\begin{aligned} \bar{v}_y(r_x) = \frac{1}{Z_{thc}} & \left(\frac{2v_{c,avg}}{3R^2} (R^2 - r_x^2)^{(3/2)} + \right. \\ & \left. 2v_{c,avg} \left(1 - \frac{r_x^2}{R^2} \right) \sqrt{R^2 - r_x^2} \right) \end{aligned} \quad (2.20)$$

$$\bar{v}_y(r_x) = \frac{8v_{c,avg}}{3R^2Z_{thc}} ((R - r_x)(R + r_x))^{(3/2)} \quad (2.21)$$

When plotted this gives the same z slice thickness averaged velocity profile modelled in Fig. 2.15 (b). The slice thickness averaged shear rate profile, $\bar{\dot{\gamma}}$, is analytically solved by taking the derivative Eq. 2.21 and averaging with $\partial_y \bar{v}_x$ (in the form: $\bar{\dot{\gamma}}(r_x) = (\frac{d}{dx} \bar{v}_y(r_x) + \partial_y \bar{v}_x) / 2$) to generate:

$$\bar{\dot{\gamma}}(r_x) = \frac{8v_{c,avg}r_x}{3R^2Z_{thc}} \sqrt{(R - r_x)(R + r_x)}, \quad (2.22)$$

which reflects the same z slice thickness averaged shear plot profile modelled in Fig. 2.15 (b).

In order to determine the shear rate cells experience at the wall of a channel from an MRI slice of thickness, Z_{thc} , in a channel of radius, R using Eq. 2.16, Q_c needs to be determined from $Q_c = v_{c,avg}A_c$. The average velocity in the channel, $v_{c,avg}$, can be determined from the slice thickness averaged velocity at the center of the channel, $\bar{v}_y(r_x = 0)$, which is directly measured by MRI by solving Eq. 2.21 for $v_{c,avg}$:

$$v_{c,avg} = \bar{v}_y \frac{3R^2Z_{thc}}{8} ((R - 0)(R + 0))^{-(3/2)} \quad (2.23)$$

$$v_{c,avg} = \frac{3Z_{thc}}{8R} \bar{v}_y(r_x = 0) \quad (2.24)$$

Substituting this into Q_c and substituting Q_c into Eq. 2.16 gives:

$$\dot{\gamma} = \frac{4 \frac{3Z_{thc}}{8R} \bar{v}_y(r_x = 0) A_c}{\pi R^3} \quad (2.25)$$

$$\dot{\gamma} = \frac{3Z_{thc}A_c}{2\pi R^4} \bar{v}_y(r_x = 0), \quad (2.26)$$

which simplifies to

$$\dot{\gamma} = \frac{3Z_{thc}}{2R^2} \bar{v}_y(r_x = 0) \quad (2.27)$$

when substituting $A_c = \pi R^2$. This simple relationship enables the shear at the wall of the lumen to be calculated from the maximum measured velocity in a channel, the known channel geometry, and the MRI slice thickness.

The slice thickness averaged velocity and shear rate profiles modelled across a channel were compared to profiles generated by MRI. In order to generate flow and shear profiles from an MRI, an ROI was drawn around a portion of the image that only included vertically oriented channels and the interstitial gel space in between them. Total flow speed and calculated shear rates in the ROI were averaged along the direction of flow to make one-dimensional flow and shear rate profiles across the four channels. The ROI and corresponding flow and shear rate profiles are displayed in Fig. 2.15. It was assumed that there was no v_z or v_x contribution to the flow in this region, so $s = v_y$.

A comparison of the modelled flow and shear rate profiles to those generated from the MRI showed similar profile shapes. Slight differences between the shape of the modelled profiles and the measured profiles could have resulted from the fact that there was not enough linear channel distance to achieve a fully developed, laminar flow profile. The average flow rate in these channels was determined to be $1.25 \text{ mL}\cdot\text{min}^{-1}$ per channel from the fact that there were ten inlet channels upstream of the four channel bottleneck in the ROI, and each of the inlets had a flow rate of $0.5 \text{ mL}\cdot\text{min}^{-1}$. Therefore, the length of channel required to fully develop the flow profile was 2.28 mm. The length of channel in between channel intersections was only 1.14 mm. However, this did not significantly change the shape of the flow profile from what was expected according to Fig. 2.15. Instead, the biggest discrepancy between the modelled flow and measured flow was the magnitude of the fluid velocity. From Fig. 2.14, the maximum slice thickness averaged fluid velocity of the channels was measured to be $9.0 \pm 1.1 \text{ mm}\cdot\text{s}^{-1}$, whereas the model predicted a maximum $6.0 \text{ mm}\cdot\text{s}^{-1}$. The increase in fluid velocity is likely due to an unaccounted for reduction in channel diameter. After removing the needles used for casting channels, swelling of the biopolymer matrix [121] and flow induced deformation of soft channels [122] are expected to induce changes to channel geometry. Lastly, the x resolution of the MRI was only 14% of the channel diameter. Slight changes in alignment of the voxels in the xy plane relative to the position of the channels could also affect measurements through sampling error.

2.2.3.2 Flow in Macroporous Sponge Scaffold

Total flow speed and shear rate maps of flow in a porous collagen sponge are shown in Fig. 2.16. All channel inputs were set to $0.5 \text{ mL}\cdot\text{min}^{-1}$ during flow image acquisition. Since all channel axes in the sponge were coplanar, a thinner MRI slice of 1.6 mm was used to capture luminal flow in all channels.

Although some luminal flow was seen in the flow speed map, the channel geometry, as indicated by regions of high flow, was much less distinct than in the biopolymer gel. The shear map showed almost no features resembling channels, and the vector plot showed greater flow in the interstitial regions with more stochastic behavior. Thicker MRI slices were not used because averaging larger volumes of interstitial flow from above and below the channels overpowered and obscured the signal from faster luminal flow. The fluid permeability of the UltrafoamTM sponge was $2.54 \times 10^{-12} \text{ m}^2$, its pores ranged from 100 to 200 μm in diameter, and its void volume was 90% [83]. Considering the unit cell of the scaffold and the relationship in Eq. 2.15, the ratio of flow in the open channels to flow in the scaffold was calculated to be $v_{s,avg} = 4.15 \times 10^{-5} v_{c,avg}$. This initially suggests that the flow through the matrix is negligible compared to luminal flow, however, the scaffold pore diameters are not small enough to consider the sponge as a homogenous material. Assuming an average pore size of 150 μm , these pore diameters are about a tenth of the size of the channels and are on the same order of magnitude as the xy resolution of the MRI. Therefore it cannot be assumed that the porous sponge will behave like a uniform material on the observed length scale. Instead, it was assumed that the interconnected pores form a cylindrical pathway approximately twice the length of the scaffold as has been done in previous work [83,123]. Considering all pores as parallel flow paths to the channels and to each other, the pressure drop across each individual pore is the same as the pressure drop across the channel. Therefore, flow in a single pore, Q_{p_i} , was compared to flow in the channel using the relationship:

$$\frac{8\mu L Q_c}{\pi R^4} = \frac{16\mu L Q_{p_i}}{\pi R_{p_i}^4} \quad (2.28)$$

$$Q_{p_i} = \frac{R_{p_i}^4}{2R^4} Q_c \quad (2.29)$$

where R_{p_i} is the radius of an individual pore. The total flow rate through the pores, Q_{p_t} can be found from the flow rate in a single pore using the relationship $Q_{p_i} = Q_{p_t}/n_p$ where n_p is the number of pores. The volume of an individual pore, V_{p_i} is related to the void volume in the scaffold, ϵ , and n_p by

$$V_{p_i} = \frac{\epsilon V_s}{n_p}, \quad (2.30)$$

which can be solved for n_p to obtain

$$n_p = \frac{\epsilon V_s}{V_{p_i}}. \quad (2.31)$$

Substituting this into Eq. 2.29 gives:

$$\frac{Q_{p_t} V_{p_i}}{\epsilon V_s} = \frac{R_{p_i}^4}{2R^4} Q_c \quad (2.32)$$

$$Q_{p_t} = \frac{\epsilon V_s R_{p_i}^4}{2V_{p_i} R^4} Q_c, \quad (2.33)$$

which can be further simplified by substituting the volume of a single pore, $V_{p_i} = 2L\pi R_{p_i}^2$, and the volume of the scaffold's interstitial space, $V_s = A_s L$, to obtain

$$Q_{p_t} = \frac{\epsilon A_s R_{p_i}^2}{4\pi R^4} Q_c. \quad (2.34)$$

Evaluating the expression reveals that $Q_{p_t} = 3.3 \times 10^{-3} Q_c$. This is not nearly as great a difference as seen in the gel, and it suggests that flow in the pores cannot be neglected when modelling flow in a collagen sponge. This is consistent with the flow speed map in Fig. 2.16, which shows less flow concentrated in the channels and more diffuse flow throughout the pores. The complex flow distribution makes MRI particularly useful for measuring local flow in the macroporous environment of a sponge.

The potential to use flow weighted MRIs to approximate the average shear rate at the walls of the pores on a voxel by voxel basis was evaluated. This was only considered for voxels entirely encompassing sponge pores that had no volume overlap with the laser cut channels.

First, the total volumetric flow rate in each voxel was calculated using: $Q_{i,j} = \bar{v}_{i,j} A_v|_{i,j}$ where $Q_{i,j}$ is the volumetric flow rate through an individual voxel, $\bar{v}_{i,j}$ is the average fluid velocity measured in the voxel, and $A_v|_{i,j}$ is the area of the voxel obtained by projecting the voxel onto a plane perpendicular to the velocity vector. Since all channels were aligned in one plane, the z direction velocity component was ignored. Therefore, the equation for flow rate through a voxel became:

$$Q_{i,j} = \sqrt{\bar{v}_x|_{i,j}^2 + \bar{v}_y|_{i,j}^2} W_{i,j} Z_{thc} \quad (2.35)$$

where $W_{i,j}$ is the width of the projected voxel cross section plane found from $W_{i,j} = dy \cos(\theta_1|_{i,j}) + dx \cos(\theta_2|_{i,j})$. $\theta_1|_{i,j}$ and $\theta_2|_{i,j}$ are the angles between the velocity vector and the x and y axes respectively. They are found using $\theta_1|_{i,j} = \arctan(\bar{v}_y|_{i,j}/\bar{v}_x|_{i,j})$ and $\theta_2|_{i,j} = \arctan(\bar{v}_x|_{i,j}/\bar{v}_y|_{i,j})$. Knowing the volumetric flow rate in each voxel and assuming the tortuosity of the pores doubles their length relative to the length of a voxel, the average velocity in the individual pores within each voxel was estimated from:

$$v_{p_i}|_{i,j} = \frac{2L_v|_{i,j} Q_{i,j}}{\epsilon V_v} \quad (2.36)$$

where $L_v|_{i,j}$ is the length of a voxel projected in the direction of overall velocity, $L_v|_{i,j} = dx \cos(\theta_1|_{i,j}) + dy \cos(\theta_2|_{i,j})$ and V_v is the volume of the voxel. Applying Eq. 2.16 to wall shear in an individual pore generates $\dot{\gamma}_{p_i} = \frac{4Q_{p_i}}{\pi R_{p_i}^3}$. Substituting $v_{p_i} \pi R_{p_i}^2$ for Q_{p_i} in this equation and simplifying demonstrates that the average wall shear rate in the pores in a voxel can be approximated by:

$$\dot{\gamma}_{p_i}|_{i,j} = \frac{4v_{p_i}|_{i,j}}{R_{p_i}} \quad (2.37)$$

Using $\tau_w|_{i,j} = \mu \dot{\gamma}_{p_i}|_{i,j}$ where $\tau_w|_{i,j}$ is the approximate wall shear stress for the pores within a voxel and μ is the dynamic viscosity of cell culture media, a map of wall shear stress was plotted in Fig. 2.17.

2.2.4 Discussion

The results were able to show that our bioreactor was able to maintain perfusion flow and temperature for periods that are sufficient for tissue culture. Various scaffolds tested were also found to be compatible in our perfusion system. The various scaffold materials tested in the bioreactor that were found to be compatible will allow for an assortment of future tissue engineering experiments involving complex flow patterns in environments with very different fluid permeabilities and pore sizes. Biopolymer hydrogels patterned with channels provide an optimal environment to study the influence of flow on endothelial sprouting and neovascularization. Endothelial cells range in length from 22-26 μm and in width from 5-13 μm . They cover areas ranging from 70 to 245 μm^2 [124]. Compared to endothelial cells, the pores in a biopolymer hydrogel are small than the cell's dimensions. The combination of dimensions possessed by the cells and pores allows endothelial cells to attach to and migrate across the gel surface as a monolayer similar to the endothelial lining on vessel walls *in vivo*. When this occurs, a single cell blankets many matrix pores and fibers at the gel surface. The dimensions of the cells also allow cells to move through the hydrogel matrix, making biopolymer gels optimal for studying endothelial sprouting which is similar to angiogenesis [81, 86–88, 90] and the process of *de novo* neovascularization [89, 91].

For macroporous sponges, it has been demonstrated that commercial and collagen sponges were the best scaffolds to support endothelial cell culture and were mechanically compatible with the perfused environment of the bioreactor. Therefore, based on these results, we planned to use these sponge scaffolds for culture experiments that can demonstrate the feasibility of our bioreactor in supporting thick tissue constructs to study the effects of flow patterns or large-scale interstitial flow gradients on cell distribution, viability, and growth. The work related to such experiments are shown in the next chapter.

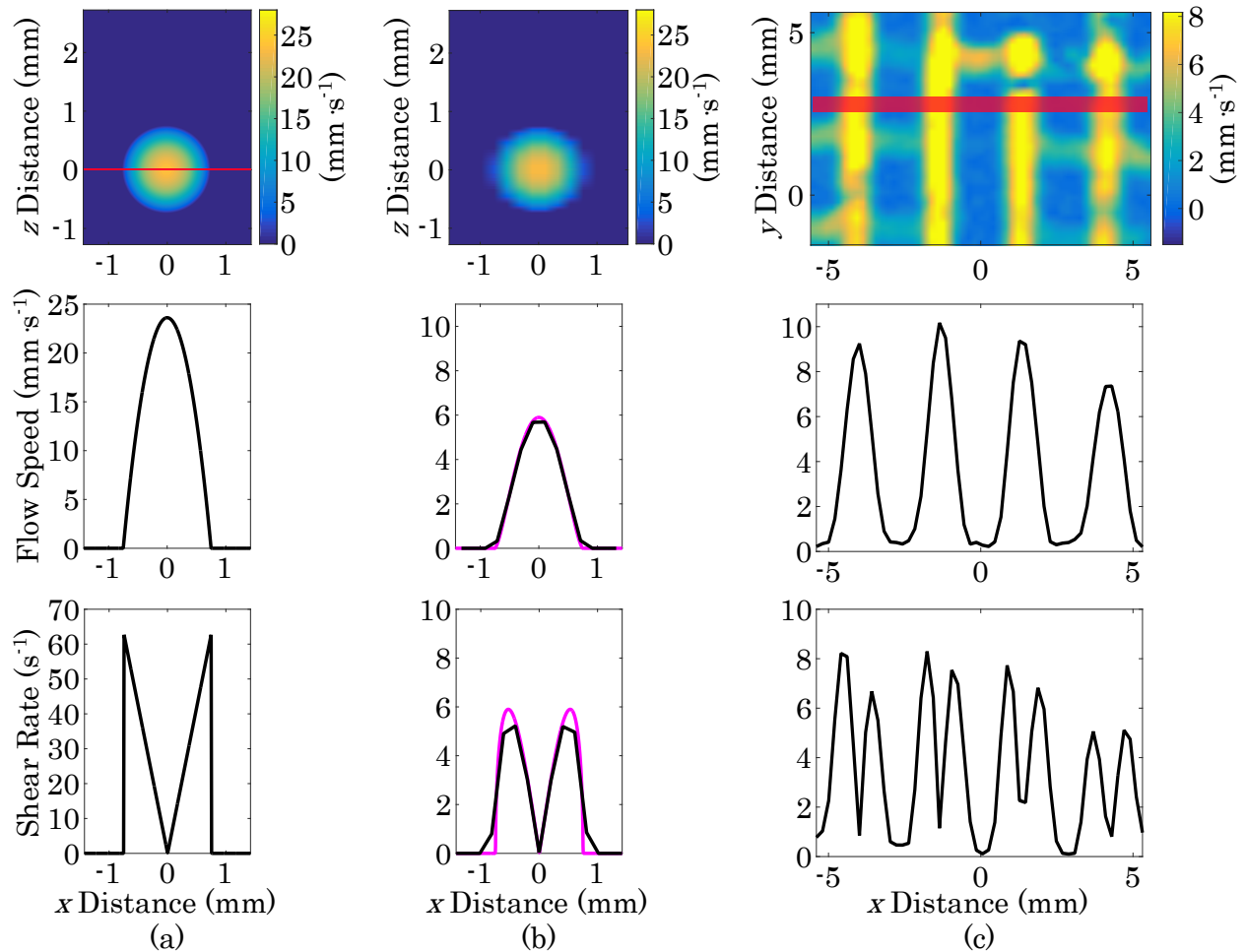


Figure 2.15: **Analysis of Flow-weighted MRI.** (a) Top: cross section view of v_y modelled in channel and surrounding matrix. Middle: plot of modelled v_y along red line. Bottom: plot of modelled $\dot{\gamma}$ in matrix and channel along red line. (b) Top: cross section view of v_y in channel and surrounding matrix segmented with the same x resolution used in the flow-weighted MRI from Fig. 2.13. Middle and Bottom: plot of modelled \bar{v}_y and $\bar{\gamma}$ profiles respectively. Black profile is segmented with same x resolution used in MRI. Magenta profile is unsegmented. (c) Top: portion of flow speed map seen in Fig. 2.13 with ROI highlighted in red. Middle: profile of average flow speed in ROI along x direction. Bottom: profile of average shear rate in ROI along x direction. Adapted from [5] with permission, © Brian Archer 2021

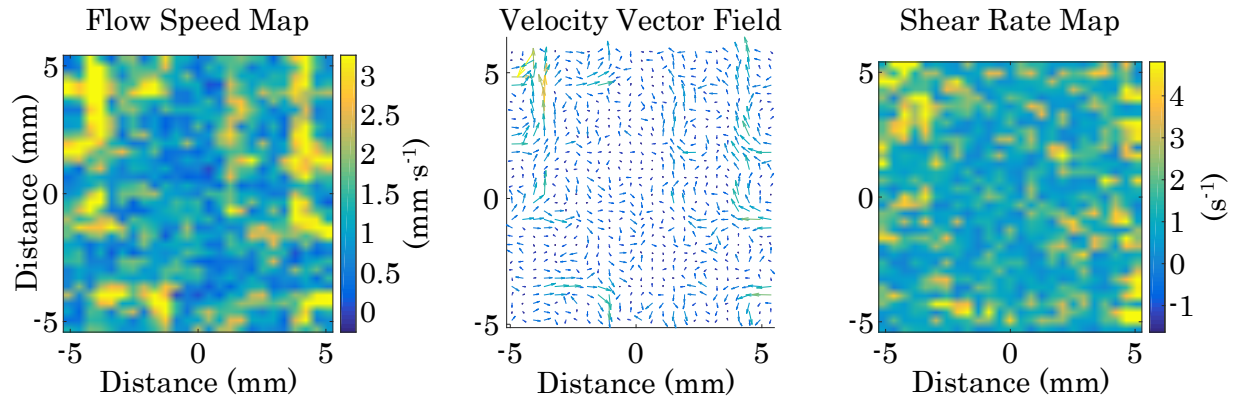


Figure 2.16: **Flow and Shear Maps in Collagen Sponge.** The left panel is a map of the total flow speed magnitude. The middle panel is a flow vector field made from the \bar{v}_x and \bar{v}_y maps. The right panel is a map of $\bar{\gamma}$. Adapted from [5] with permission, © Brian Archer 2021

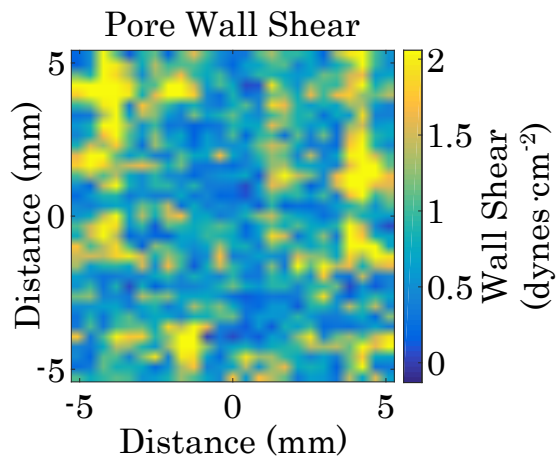


Figure 2.17: **Wall Shear in Collagen Pores.** Map of estimated shear stress at pore walls in collagen sponge plotted in $\text{dynes} \cdot \text{cm}^{-2}$. Adapted from [5] with permission, © Brian Archer 2021

CHAPTER 3

Tissue Culture Experiments with Custom Bioreactor

Thick tissue constructs (>6 mm) are often required when being used for medical applications, whether that be cartilage or bone grafts or artificial skin tissue [26]. However, the maturation of thick constructs cannot be achieved through static culture alone as passive diffusion cannot sufficiently provide nutrients and remove waste throughout the whole construct [26, 44] and it has been demonstrated that inhomogeneous distribution of functional cells will result in non-uniform cell proliferation, viability, and matrix deposition and eventually, inhomogeneous tissue formation [74]. As result, bioreactors were developed to better mimic the native environment by providing the spatiotemporal variation of signals and sufficient delivery of nutrients and removal of waste [75]. However, there still has been limited success in translatability of research with cell-based tissue constructs which is attributed to a lack of standardization and reproducibility issues [11, 12]. All of these challenges demonstrate a lack of understanding on the effects of the complex flow environment on engineered tissue development. As mentioned, we had designed a 10-channel bioreactor with the ability to deliver arbitrary flow patterns and noninvasively control and monitor fluid-induced shear forces in optically opaque media with MRI to study the influence of varied spatiotemporal biomechanical signaling on engineered tissue development [79]. However, no work had been done on determining whether such a bioreactor can support thick, viable tissue constructs. Little work had also been done on whether the bioreactor was compatible with different scaffold types. With our current bioreactor that improves upon the previous model, we have already demonstrated its ability to maintain flow and temperature over long culture periods and its compatibility with multiple scaffold types in the previous chapter.

As a result, tissue culture experiments were carried out in our bioreactor with two major goals: 1) To determine the effects of perfusion flow on distribution of cell growth in a scaffold construct 2) To demonstrate the feasibility of supporting the growth and viability of thick tissue constructs with our novel bioreactor and determine how different flow patterns can affect such parameters of growth and viability. Analysis to evaluate thick tissue culture feasibility was performed similarly from a study done previously [26].

3.1 Materials and Methods

The cell lines chosen for such experiments are parenchymal HEK293 and B16-F10 cells due to their convenience and low cost of culture as mammalian cell models. The scaffold utilized are commercial collagen (Ultrafoam™) and gelatin (Gelfoam™, Surgifoam™) sponges as they were determined from scaffold compatibility experiments to be the most suitable for the 3D perfusion culture of cells. The media utilized was DMEM with 10% FBS, 1% L-Glutamine, and 1% antimycotic-antibiotic solution.

To explore the effect of the perfusion of flow patterns on the distribution of parenchymal cells in 3D tissue culture, human embryonic kidney cells (HEK293) were cultured for five days in the bioreactor in a porous collagen sponge (Ultrafoam™) under a flow pattern where all 12 inlets had a flow rate of 0.5 mL/min. A comparison of the cells cultured under flow is done to cells cultured in static media for the same duration and to cells only two hours following seeding. Cells were seeded by soaking them in cell suspension containing 1.5×10^6 cells·mL⁻¹ for 2 hours at 37°C. After the allotted culture period, scaffolds were fixed, stained with DAPI, and imaged with a 20× objective on a Leica SP-5 confocal microscope at selected regions of the scaffold.

To demonstrate the capability of our novel bioreactor in supporting the growth and viability of thick tissue constructs, B16-F10 cells were seeded on gelatin sponges by soaking them in cell suspension at a 1.0×10^7 cells·mL⁻¹ for 30 minutes at 37°C. The gelatin sponges

were cut to fit in the chamber with dimensions of $1.2\text{ cm} \times 1.2\text{ cm} \times 7\text{ mm}$ which is considered a thick scaffold ($>6\text{ mm}$ scaffolds) [26]. After seeding, scaffolds were either harvested right away, or cultured under flow in the bioreactor for 3 or 5 days or in a 6-well plate under static conditions for 3 or 5 days. Media was changed every 2 days for static conditions. The chosen flow pattern for culture was an input of flow rates of $1\text{ mL}/\text{min}$ for channels 1-4 which would generate a side profile in the tissue chamber. After culture for the allotted time, scaffolds were harvested, stained with CMRA for all cell membranes, Image-IT™DEAD-Green™(denoted as IIT in paper) which stains all dead cells and is compatible with fixation, and fixed with 2% PFA for an hour. Scaffolds were then rinsed with PBS and suspended in sucrose solution in preparation for sample freezing. samples were then covered in OCT-glue in a cryomold, frozen, and stored in a -80°C freezer until further processing. Scaffolds were sectioned at 20 micrometers using a cryostat (2 sections from the periphery or top of the scaffold, 2 sections from the core or center of the scaffold, and 2 sections from the bottom of the scaffold) and mounted using ProLong® Gold Antifade Mountant with DAPI to prolong sample stability and stain with DAPI. Scaffold sections were imaged with a $10\times$ objective on a Zeiss LSM 880 confocal microscope to get a full view of the cells and the scaffold. A z-stack was also taken to ensure the full scaffold section was imaged. Image processing and analysis was done using Fiji software to determine the number of cells, adjust autofluorescence, and improve cell visualization over the whole scaffold. Heatmaps to illustrate cell density distribution were made using countNonZeroPixels2DSphere in CLIJ2 image processing library on Fiji [125]. To determine the effect of different flow patterns on cell growth and viability, many shorter culture experiments (1 Day Culture) were carried out with different flow pattern culture conditions. The same protocol is followed as mentioned previously with B16-F10 cells and gelatin sponges with only the culture period being shortened and only 3 sections being taken (one from top, middle, and bottom) from the scaffold instead of 6. The different flow patterns in the bioreactor being compared are as follows: perfusion conditions with flow rates of either $0.2\text{ mL}/\text{min}$, $0.5\text{ mL}/\text{min}$, or $1\text{ mL}/\text{min}$ inputted in channels of either channels 1-4, 5-8, or

9-12. A static condition group cultured for 1 day was also collected for comparison.

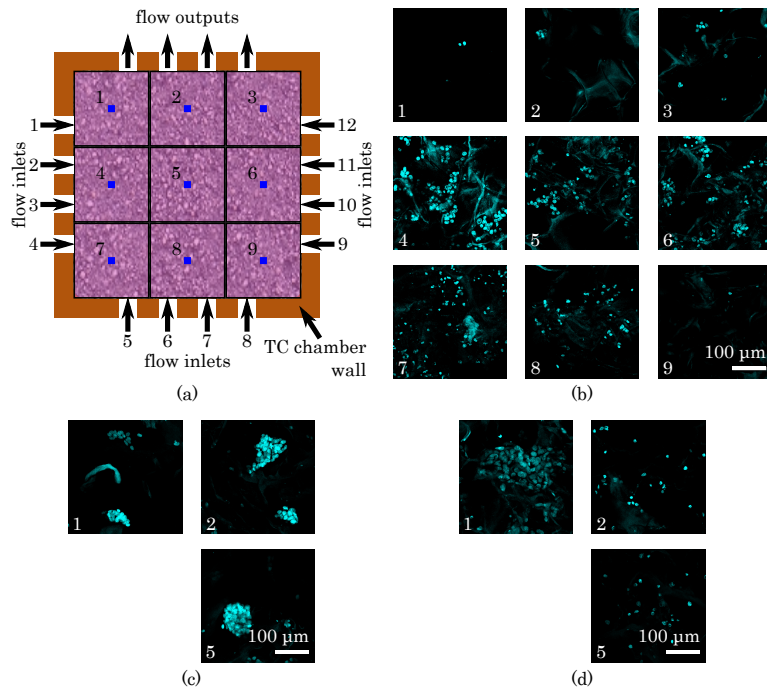


Figure 3.1: Flow Pattern Influences Parenchymal Distribution. (a) Diagram highlighting imaged regions of scaffold. Numbered regions are indicated with respect to the flow channels surrounding the TC chamber. Square regions highlighted in blue correspond to actual size of confocal micrographs. (b) Confocal micrographs of HEK293 cells stained with DAPI cultured on porous collagen scaffold for 5 days under the flow pattern with 0.5 mL/min flow rates in all inlets. (c) Confocal micrographs of select regions of scaffold seeded with HEK293 cells for 2 hours. (d) Confocal micrographs of HEK293 cells cultured on a porous collagen scaffold for 5 days statically in an incubator. Adapted from [5] with permission, © Brian Archer 2021

3.2 Results

3.2.1 Effect of Flow on Cell Growth Distribution in 3D

Figure 3.1 provides representative micrographs of the distribution of parenchymal cells at various regions of the collagen scaffold from different culture periods and conditions. It can be seen from Fig. 3.1 (c) that immediately after seeding, cells clumps about 100-150 μm in diameter attached to walls of the porous scaffold. These clumps were likely an artifact of strong intercellular HEK293 interactions when cultured statically on a 2D surface. Although large clumps and sheets of cells were mechanically disrupted with vigorous pipetting during trypsinization, many cells remained attached to each other in smaller aggregates. In Fig. 3.1 (d) cells that were statically cultured in the porous scaffold for five days tended to dissociate from the large clumps in which they were initially seeded and spread out as individual cells in regions of the sponge with less nutrient access. The corners of the sponge appeared to support growth of higher cell densities, likely due to increased nutrient access in those regions. Only regions 1, 2, and 5 were shown due to the symmetry of nutrient distribution in the statically cultured sponge (regions 1, 3, 7, and 9 are identical corners; regions 2, 4, 6, and 8 are in the middle of the flat edges; and region 5 is the center of the sponge). Representative confocal micrographs of HEK293 cells cultured in a porous scaffold in the bioreactor under the same flow pattern with flow in all inlets are shown in Fig. 3.1 (b). It can be seen that there was an inhomogeneous distribution of cell density throughout the scaffold cultured in the bioreactor, which differs from the distribution seen in static culture. Very few cells were seen near the outlets of the TC chamber where flow was highest. Most cell growth occurred in regions 4, 5, and 6. Cell density in regions 4 and 6 exceeded equivalent regions in statically cultured sponges by a factor of 3.3. The cell density in the center of the sponge (region 5) exceeded the equivalent region in static culture by 2.3 times. It is hypothesized that cell density observed in regions 1, 2, and 3 was much lower than in other regions due to high shear stress disrupting cell adhesion to the pore walls. HEK293s are known to have lower

surface adhesion strength than other mammalian cells [126,127].

3.2.2 Feasibility of Growing Thick Tissue Constructs with Novel Bioreactor

To assess the feasibility of supporting thick tissue constructs in our novel perfusion bioreactor, fluorescent micrographs were obtained from sections of various regions of a thick Gelatin scaffold cultured with B16-F10 cells similar to analysis done previously [26]. Scaffolds were cultured for either 3 or 5 days statically or under a side flow profile with flow rate inputs of 1 mL/min from channels 1-4. Figure 3.2 illustrates representative micrographs of the scaffold that were obtained after five days of culture. While DAPI did show a slightly higher intensity for nuclei, the autofluorescence from the gelatin scaffold was still difficult to filter out and distinguish from DAPI nuclei as observed in Fig. 3.2(b). CMRA was much more selective for cell membranes and allow for better distinction of fluorescent cells compared to background autofluorescence as observed in Fig. 3.2(c). As a result, CMRA was subsequently utilized as a measure of cell number for subsequent scaffold micrographs. IIT was also selective for dead cells as only a selective few cells fluoresced green, suggesting they were dead. Separate to the experiment, a positive test was done for confirmation of dead cell selectivity. Dead cells (submerged in ethanol) were placed in a plate and adherent, live cells in another plate were stained with IIT and imaged for fluorescence and it was found that only the dead cell plate possessed green fluorescence (not shown). Therefore, green fluorescence puncta were also used as a measure for raw dead cell counts. Figure 3.3 provides the cell density measurements (CMRA counts divided by total scaffold volume imaged) of CMRA as a measure of cell growth over time for the different culture conditions. As observed from the plot in Fig. 3.3, CMRA density drastically increased for both culture groups after 5 days compared to initial seeding density measurements (5 times higher for perfusion, 10 times higher for static). This can also be observed from the micrographs in Fig. 3.4 where there were more orange puncta at 3 and 5 days for both culture groups compared to the initial amount of puncta at 0 days. For distribution, it seemed that the number of CMRA-fluorescent cells started to shift

along the edges of the scaffold section for static conditions while the cells in the scaffold for perfusion culture maintained relatively similar distributions over time with cells still residing in the center. This distinction was more pronounced after five days of culture based on the micrographs from Fig 3.4 (d) and (f) which shows the central region of cells where static culture had less puncta. Fig.3.5(b)-(c) shows micrographs of the edge of the scaffold with more puncta being present for static culture. Cell clumping and intercellular interactions were also observed over time for both groups. At 0 days, there was no clumping within the scaffold until after 5 days where it became more visually significant for both groups. An example of cell-cell interactions is shown in Fig. 3.6 both in the 20 \times image in Fig. 3.6 (a) and 100 \times image in Fig. 3.6 (b) as multiple cells are clearly in contact with each other. The 100 \times image provides a clear distinction and visualization of subcellular staining with CMRA staining the membrane (Orange) and DAPI staining the nuclei (Cyan).

To quantitatively visualize how the side perfusion profile affected cell distribution of the tissue scaffolds comparative to static conditions, the image was grayscaled, cells were segmented and labeled, cell pixels were converted to centroid-pixels, and a heat map was generated where every nonzero pixel around every pixel-centroid with radius of around 30 microns was summed and plotted as a heat map on the scaffold where higher heatmap values represent more CMRA pixel signals which correlates to more cells in that region. Heatmaps from both static and perfusion culture scaffolds are shown in Figure 3.7. For static culture scaffolds, it can be observed that there were more CMRA fluorescence signals from the heatmap in Figure 3.7(a) on the outer edge of the scaffold compared to the central region which correlates to micrographs in Fig 3.6 for CMRA cell fluorescence. For perfusion culture, it can be seen that CMRA fluorescence signal, was lower on the left side of the scaffold, where the flow rates entered the scaffold, and on the bottom of the scaffold, which is where the outlets were located, suggesting lower cell counts at these regions of the scaffold. Both sections from a perfusion culture scaffold showed this trend in Figure 3.7(b)-(c). Besides cell growth, another parameter analyzed to assess the support of thick tissue in our bioreactor

is viability. Image-IT™ DEAD-Green™ micrographs, which is a fluorescent dye for dead cells, was analyzed. As observed by the plotted counts in Fig. 3.8 (a)-(c), higher counts of cells stained with IIT were found for 3 day and 5 day static conditions compared to perfusion conditions from the whole scaffold, the periphery, and the core of the scaffold which suggests higher cell death for static conditions. The representative micrographs in Fig. 3.8 (d)-(e) portray these differences as more cells were fluorescing green under static conditions compared to micrographs from the perfusion culture group.

3.2.3 Effects of Different Flow Patterns on Cell Growth and Viability of Tissue Constructs

In order to determine whether different flow patterns had an effect on cell growth and viability in tissue development, Various 1-day culture experiments with different flow patterns were carried out and the scaffolds were again stained with CMRA and IIT for comparison. Based on the CMRA cell density plot from Fig. 3.9 (a), CMRA cell density was highest for the 0.5 mL/min flow rates in channels 1-4 and 9-12 but not for 5-8. For viability, static culture again seemed to have the highest number of IIT-fluorescent cells which suggests a higher number of dead cells compared to the other culture groups. Representative micrographs of the different flow patterns with 0.5 mL/min flow rates inputted at each channel are shown in Fig. 3.10. The images correlated with the comparisons found in Fig. 3.9 as there were more CMRA puncta from channels 1-4 and 9-12 but not for 5-8 at 0.5 mL/min flow rate inputs. The distribution of the orange puncta seemed to be relatively uniform. MRI flow maps from the particular pattern are also shown in Fig. 3.9(b) which is above the micrograph images and correlated to the expected flow profile from flow rate inputs.

3.3 Discussion

In Fig. 3.1, it was demonstrated how flow patterns can alter the distribution of parenchymal cells within a scaffold which could be a result of differential nutrient distribution from the particular flow pattern. Shear forces may have also contributed to such a distribution as cells may have detached from regions of higher shear stress. Such results demonstrate the importance of flow patterns in perfusion culture as it can alter the distribution of cells in a scaffold where uniform distribution of cells are desired in a functional scaffold [128]. Results with B16-F10 cells in gelatin sponges also demonstrated the feasibility of our novel bioreactor in culturing thick tissue scaffolds, in this case 7 mm scaffolds. Fig. 3.3 demonstrated an increase of CMRA densities for both culture groups (static, perfusion) after 3 and 5 days which suggests cell growth after seeding. Samples processed right after seeding (0 Day Samples) had very low cell counts which could have been a result of 30 minute incubation times being too short for all cells to adhere in time to the scaffold. However, low cell counts may have had utility in demonstrating growth as the change in CMRA number over time was more drastic for determining tissue growth. Another feature found from scaffolds over later culture periods was greater clumping of cells compared to seeded scaffolds which suggests both migration and proliferation occurring in the scaffold which are important cell behaviors for cell-cell interactions in tissue engineering [40]. Cell-cell contact for potential interactions can clearly be seen from both the 20 \times and 100 \times micrographs in 3.6 where multiple cells are visually clumped adjacent to each other. Such images also ensured that subcellular staining was accurately and specifically occurring as CMRA stained the cell membrane and DAPI stained the cell nuclei as expected. Another result that was expected was the intensity heatmap of CMRA for a static scaffold section. The scaffold had more cells populated along the edges (especially upper left corner in the heatmap) than the central region of the scaffold which possessed many zero pixels in the center (black regions). Micrographs from Fig. 3.4 and Fig. 3.5 parallels what was shown from the heatmaps. This confirms the limitations with static culture where cells along the edges can consistently be supported through direct

contact and diffusion of media while diffusion is insufficient to support the central region of the scaffold [26]. One interesting result from the CMRA data was the lower cell densities of scaffolds under perfusion compared to scaffolds under static culture in Fig. 3.3. This could potentially be explained by analyzing the intensity profiles from sections of the scaffold under perfusion in Fig. 3.7 (b)-(c). Intensity signals for CMRA seem to populate at regions to the upper right and center of the scaffold with a relatively uniform distribution being present in the center. Lowest signals were found for regions on the left and bottom of the scaffold. Both of these regions are expected to experience the highest shear forces as the left of the scaffold would directly experience flow from the inlets of channels 1-4 and the bottom of the scaffold would experience perfusion flow to the outlets. Such forces may have caused a "washing-out" effect where cells with weaker adhesion strength were detached initially from the scaffold, resulting in lower CMRA counts as a scaffold starting point. While there were some intense signals in the first section heatmap at the region adjacent to the inlets, this could be a result of cells who were able to resist and still adhere to the scaffold wall under high shear forces. Such adhered then would be able to proliferate due to having direct access of nutrients by being adjacent to the inlets with flow. Lower cell counts from lack of nutrients seemed unlikely as the trend for cell growth was present based on the plot of CMRA density over time for the 0.5 mL/min flow rates at channels 1-4 flow group. IIT analysis from Fig. 3.8 also seems to confirm this as the number of dead cells was significantly lower for all regions of the scaffold under perfusion flow compared to static conditions over time. Such a difference could be a result of interstitial flow from perfusion which provided greater access to oxygen and nutrients throughout the whole thick scaffold to maintain viable cells while diffusion alone from static conditions could not support the viability of all the cells in the scaffold. Therefore, such results demonstrate the ability of our bioreactor in supporting thick scaffolds that could be clinically relevant. Such experiments and analysis are based on a similar feasibility paper carried out previously and is in agreement with the finding that static culture could not support viability throughout a thick scaffold [26].

We now examine how different flow patterns can affect growth and viability in thick scaffolds. Results from Fig. 3.9 suggests a distinct difference in both viability and growth based on the flow pattern. 0.5 mL/min inputted at channels 1-4 and 9-12 yielded the highest CMRA densities while static culture conditions had the highest number of dead cells compared to perfusion flow patterns. Viability results again confirm the results previously where static conditions cannot properly support all cells through passive diffusion alone. CMRA results suggest some optimal condition could be present for tissue growth due to differences present from different flow patterns. The flow patterns could potentially have been optimal by having flow rates that were not too high to avoid inducing cellular detachment of cells but not too low to hinder nutrient access required for cell growth. Interestingly, the flow pattern generated from 0.5 mL/min at channels 5-8 was not much higher compared to the other groups. This could potentially be a result of lower shear forces generated from flow in channels 5-8 compared to side flow profiles of 1-4 or 9-12 as observed by the flow maps in Fig. 3.9 (b) which suggests the possibility that a certain mechanical cue from a shear stress cutoff value is needed to induce cell growth but more research is necessary to explain such a result. Overall, such a culture experiment demonstrates the importance of flow patterns in a bioreactor due to their effect on cell growth and viability in tissue scaffolds which stresses the importance of the proposed perfusion bioreactor as it can generate a variety of different flow patterns from its 12 channel inlets.

One drawback of the bioreactor system was its degree of operating complexity and intensive use of resources for culture and sterilization. The large number of steps and flow configurations required when preparing the system required extensive operator training and careful execution. Sterilization and culture were also intensive as it required large volumes of sterilant and media to cover the whole bioreactor system. One way to reduce the complexity experienced by the operator would be to replace the manually toggled stopcocks with digitally controlled solenoid valves. With these in place, most aspects of rinsing could be programmed to run in an automated sequence. Components that required reorientation and

mechanical agitation could be mounted on stepper motors, which could also be programmed into the sequence. Additionally, a simpler system could be designed with less total components to manage if one way gas pressure driven flow was implemented, since all of the components for dampening peristaltic motion would not be required. However, the cost of running a one-way flow system would be significantly higher.

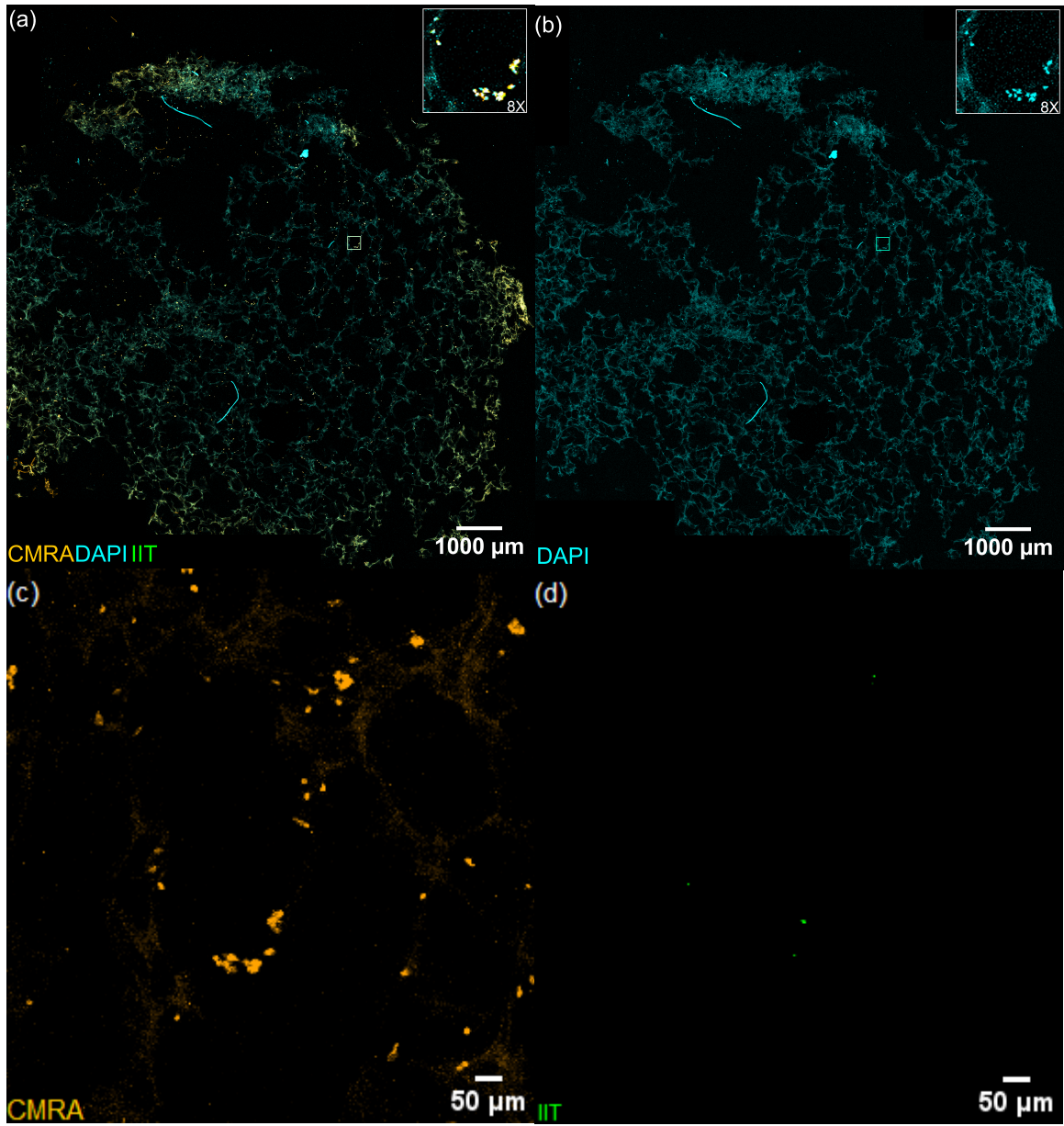


Figure 3.2: **Representative Micrographs of a Whole Scaffold Sample.** (a) Micrograph of the scaffold with all fluorescent signals overlaid (cyan-DAPI, IIT-Green, Orange-CMRA). A 8× zoomed inset image is shown on the upper right corner. (b) Micrograph of the scaffold with DAPI only. A 8× zoomed inset image is shown on the upper right corner. (c) Micrograph of the scaffold with CMRA only at the region around the 8× zoomed inset image. (d) Micrograph of the scaffold with IIT only at the region around the 8× zoomed inset image. The brightness and contrast were adjusted for all images using Fiji for visualization.

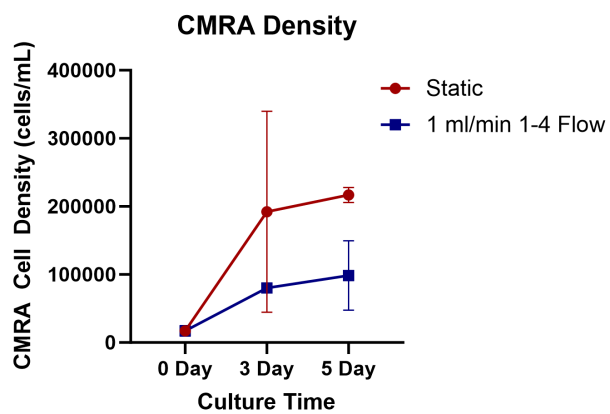


Figure 3.3: **Plot for CMRA over the Designated Culture Period.** CMRA Density plot over time. Density was calculated as the number of raw CMRA cell counts divided by the volume of the scaffold imaged. The red plot is for static culture sample densities while the blue plot is for perfusion culture densities. Height of bar and error bars are a measure of the mean and standard deviation.

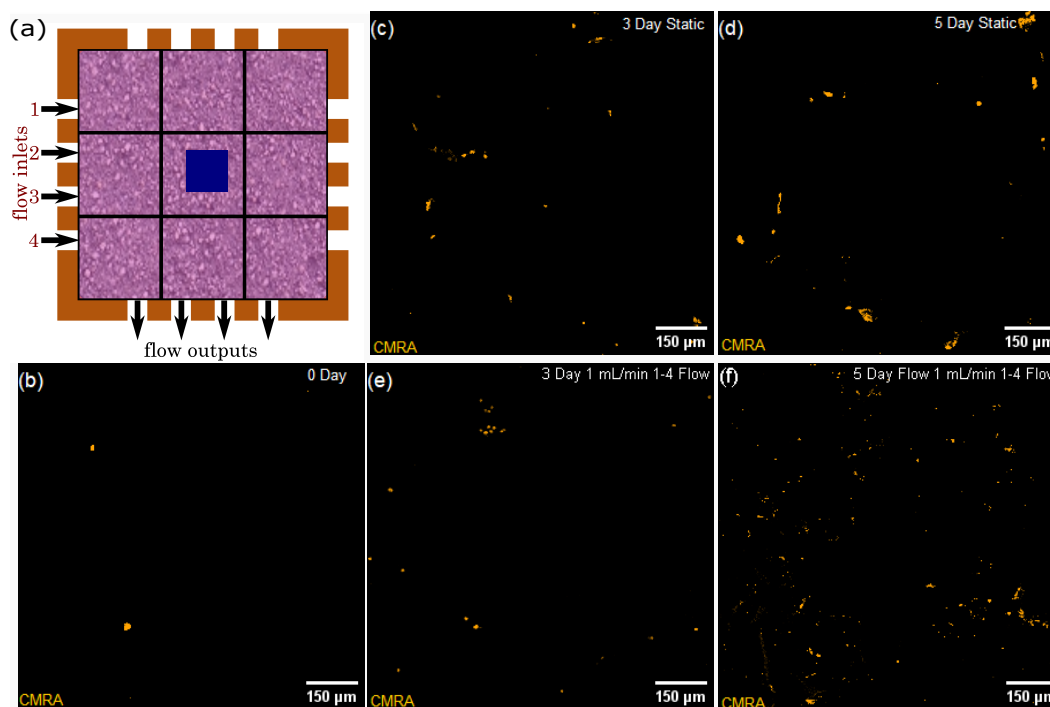


Figure 3.4: **Representative CMRA Micrographs of Central Region of Scaffold Sections from Various Culture Groups.** (a) Graphic showing direction of flow in scaffold under perfusion culture (channels 1-4 at 1 mL/min). Blue square represents central region where micrographs were taken. (b) Representative micrograph at central region of scaffold section after 0 Days of culture just after seeding. (c) Representative micrograph at central region of scaffold section from 3 Day static culture. (d) Representative micrograph at central region of scaffold section from 5 Day static culture. (e) Representative micrograph at central region of scaffold section from 3 Day perfusion culture. (f) Representative micrograph at central region of scaffold section from 5 Day perfusion culture. Contrast and brightness were adjusted with Fiji to remove autofluorescence and enhance visualization.

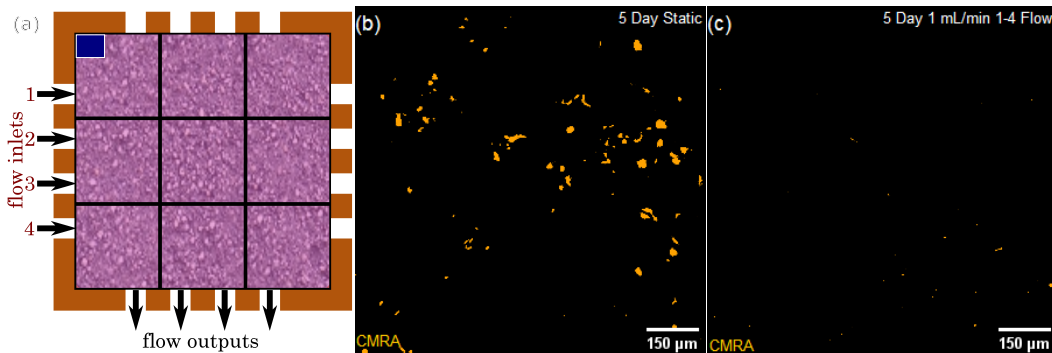


Figure 3.5: **Representative CMRA Micrographs of Edge of Scaffold Sections After 5 Days from Static or Perfusion Culture.** (a) Graphic showing direction of flow in scaffold under perfusion culture (channels 1-4 at 1 mL/min). Blue square represents central region where micrographs were taken. (b) Representative micrograph of an edge of a scaffold section after 5 days of static culture. (c) Representative micrograph of an edge of a scaffold section after 5 days of perfusion culture. Contrast and brightness were adjusted with Fiji to remove autofluorescence and enhance visualization.

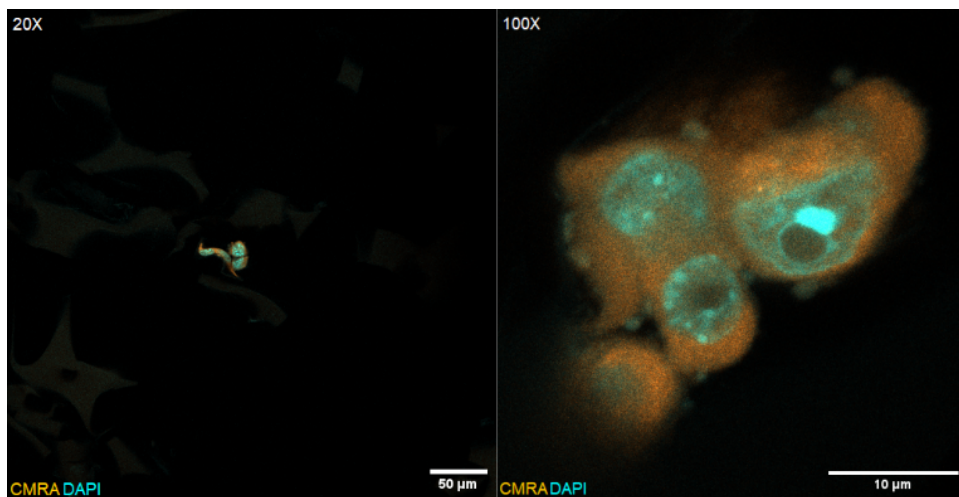


Figure 3.6: **Higher Objective Micrographs of Cell-Cell Interactions in Tissue Scaffold.** (a) 20× image of a cell clump in tissue scaffold. (b) 100× image visualizing cell-cell interactions in scaffold with expected subcellular staining visualized.

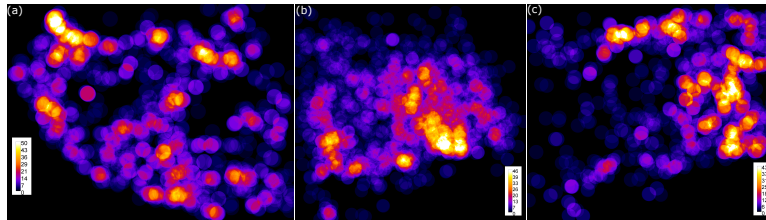


Figure 3.7: **Cell Distribution Analysis of Scaffolds From Different Culture Conditions using Intensity Heatmaps.** (a) Intensity heatmap for CMRA from a section of a static culture scaffold. (b) Intensity heatmap for CMRA from a section of a perfusion culture scaffold (1 mL/min flow rates at channels 1-4). (c) Intensity heatmap for CMRA from another lower section of a perfusion culture scaffold (1 mL/min flow rates at channels 1-4).

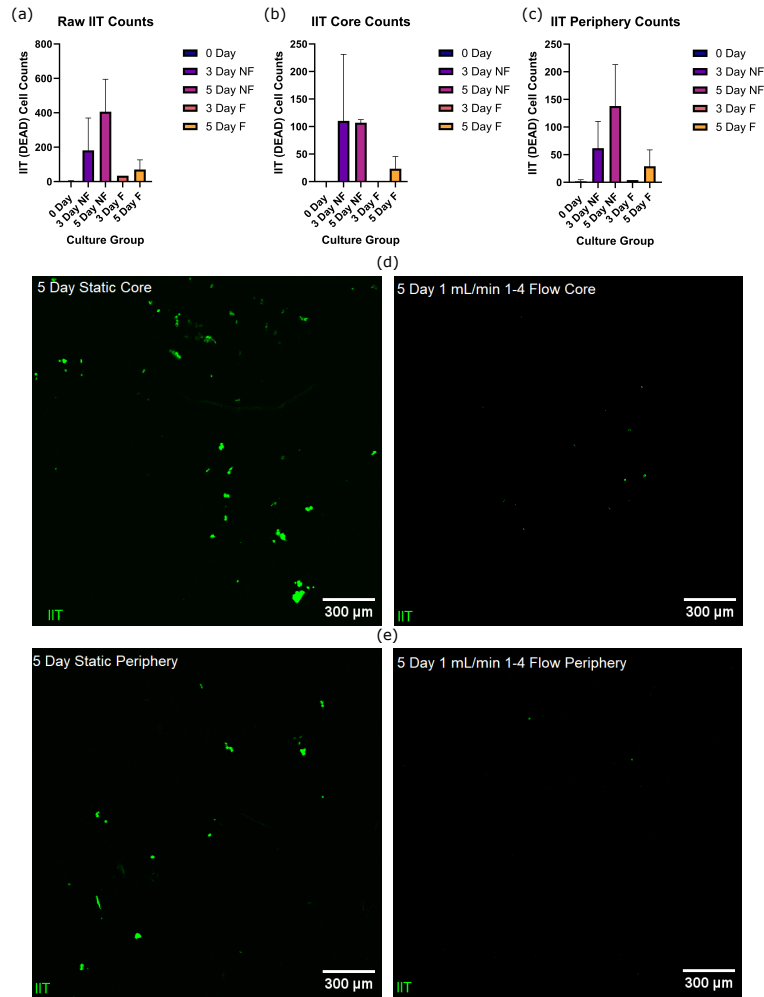


Figure 3.8: **Dead Cell Analysis for Various Culture Groups.** (a) Plot of Raw IIT Counts from the whole scaffold of different culture groups. NF stands for No Flow or static culture conditions and F stands for Flow or perfusion culture conditions. (b) Plot of Raw IIT Counts from the core or center of the scaffold. NF stands for No flow or static culture conditions and F stands for Flow or perfusion culture conditions. (c) Plot of Raw IIT Counts from the periphery or top of the scaffold. NF stands for No flow or static culture conditions and F stands for Flow or perfusion culture conditions. (d)-(e) Representative 5-day culture IIT micrographs. Top two images are micrographs from center section of the scaffold. Bottom two images are micrographs from sections specifically from the top of the scaffold. Each row has the static condition micrograph on the left and the perfusion culture condition on the right.

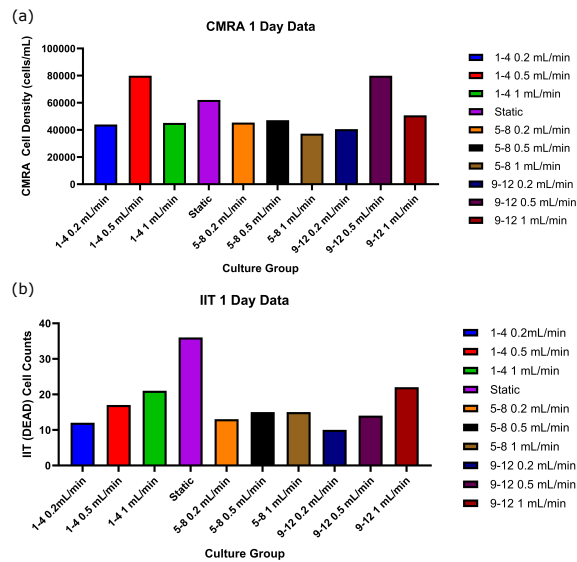


Figure 3.9: **Plots for CMRA and IIT of Different Culture Groups.** (a) Plot of CMRA cell density for different culture groups. Density was calculated as CMRA cell counts divided by volume of the scaffold. (b) Plot of raw IIT cell counts.

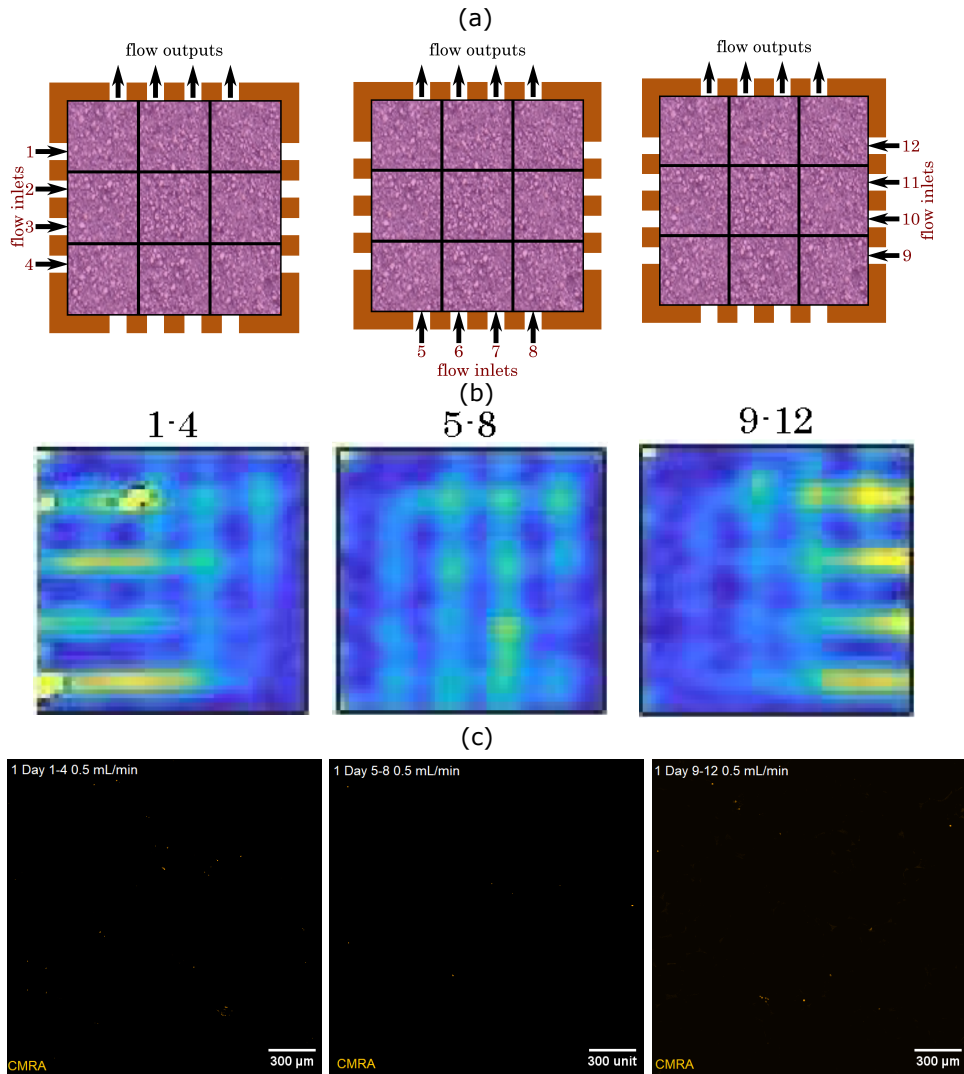


Figure 3.10: MRI Flow Maps and CMRA Micrographs for 0.5 mL/min Channel Flow Rate Culture Groups. (a) Graphic illustrating the direction of flow rate within the scaffold chamber. (b) Flow maps from flow-weighted MRI of flow patterns generated from 0.5 mL/min flow rates at the designated channels (1-4 for left map, 5-8 for middle map, 9-12 for right map). (c) CMRA micrographs for flow patterns generated from 0.5 mL/min flow rates at channels 1-4 (left micrograph), channels 5-8 (middle micrograph), and channels 9-12 (right micrograph).

CHAPTER 4

Conclusion

This thesis presents the design, construction, and evaluation of an MRI compatible, perfusion bioreactor with multiple flow inlets capable of generating custom, steady flow patterns throughout a 3D tissue culture scaffold. The study details the design of the bioreactor, the layout of the flow system, and the protocols for sterilization and aseptic cell culture loading. Multiple types of natural ECM scaffolds including macroporous sponges and biopolymer hydrogels were demonstrated to be both suitable for endothelial cell culture and mechanically compatible with the perfused environment within the bioreactor. These scaffolds also allowed for custom flow patterns to be generated throughout the TC chamber that were unique to each type of scaffold. MRI flow maps were consistent with expected results, and they were found to be useful for determining shear stresses felt by cells attached to surfaces in various types of 3D environments. It was demonstrated that MRIs of flow through cylindrical channels in a hydrogel with low interstitial fluid permeability could be used to calculate the shear stress experienced at the wall of the channel. It was also shown that maps of wall shear stress in pores of a sponge could be estimated from flow weighted MRIs.

Culture experiments also confirm the feasibility of our bioreactor in supporting thick tissue constructs from robust cell lines over multiple days. Such studies could potentially inform future work as an optimal culture condition could be found that consistently maximizes viability and density and maintains uniform distribution in a thick tissue scaffold.

Future work should look into supporting other tissue or cell types that are medically relevant and mechanically sensitive such as bone tissue or endothelial cells and determine

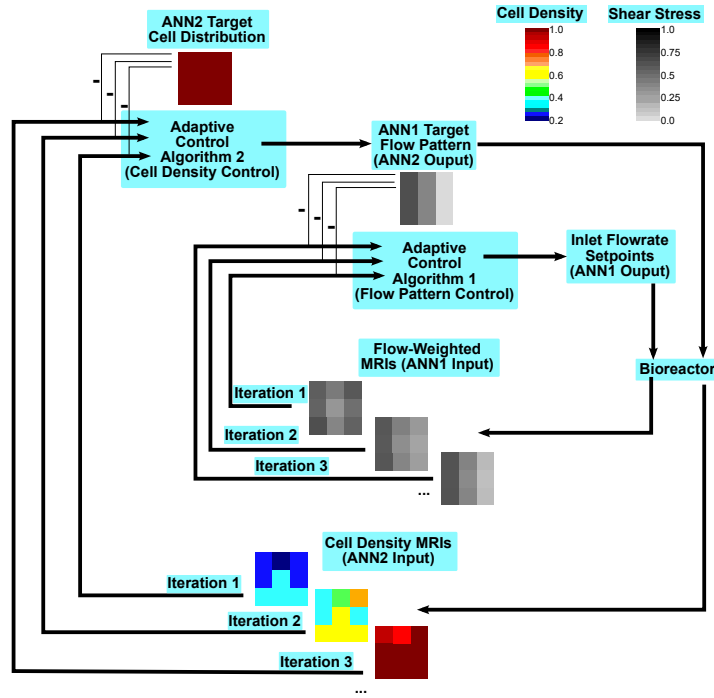


Figure 4.1: **Example of ANN Control Loop Algorithms for Tissue Optimization.**

Outer control loop is cell density control loop with target set to maximal density. Output from density loop sets target for inner control loop which is flow pattern control loop. Each iteration progressively gets closer to target due to automated adjustment. Inputs for both cell density and flow pattern is measured via MRI.

potentially an optimal culture condition for such tissues [129]. Work can also be done to develop a noninvasive, real-time cell culture monitoring platform with MRI by combining both the flow-weighted MRI maps with viability-density maps developed previously by our group [130]. Maps of viability and density can be obtained on the scaffold as well as the flow gradient of the media. Areas where density and viability are low can be supported in real time by adjusting the flow rate of inlets and monitoring the change in interstitial flow to ensure greater nutrient and oxygen access is achieved in that region. Such work can also eventually be automated with trained AI algorithms that maximize density and viability of tissue scaffolds and alters flow patterns to achieve such parameters based on the inputs generated from viability-density tissue maps at a particular time point. Fig 4.1 demonstrates

an example of an algorithm that could someday be used where maximal density and viability of a tissue are desired and adjustments to media flow are made in real time to attain such desired outputs based off of noninvasive, real-time MRI map measurements.

APPENDIX A

Supplemental Figures

A.1 Code for Density Heatmaps in Fiji

```
// To make this script run in Fiji, please activate
// the clij and clij2 update sites in your Fiji
// installation. Read more: https://clij.github.io

// Generator version: 2.5.1.5

// file to analyse
open("C:/Users/haase/Downloads/Sec 9 20X_ICC Merged_ch02.tif");

// radius to count other cells (in pixel units)
radius = 100;

// as we cannot process RGB images
run("8-bit");

// optional visualization
```

```

run(" Enhance Contrast", "saturated=0.35");

// Init GPU
run(" CLIJ2 Macro Extensions", "cl_device=");

// Load image from disc
image_1 = getTitle();
Ext.CLIJ2_pushCurrentZStack(image_1);

// Threshold Otsu
Ext.CLIJ2_thresholdOtsu(image_1, image_3);
Ext.CLIJ2_release(image_1);

// Connected Components Labeling Box
Ext.CLIJ2_connectedComponentsLabelingBox(image_3, image_4);
Ext.CLIJ2_release(image_3);

// show segmentation result
Ext.CLIJ2_pull(image_4);

// Reduce Labels To Centroids
Ext.CLIJ2_reduceLabelsToCentroids(image_4, image_5);
Ext.CLIJ2_release(image_4);

// count centroids in spheres around every pixel

```

```
Ext.CLIJ2_countNonZeroPixels2DSphere(image_5, image_6, radius, radius);  
Ext.CLIJ2_release(image_5);
```

```
Ext.CLIJ2_pull(image_6);  
run("Fire");  
Ext.CLIJ2_release(image_6);
```


REFERENCES

- [1] A. G. Abdelaziz, H. Nageh, S. M. Abdo, M. S. Abdalla, A. A. Amer, A. Abdal-hay, and A. Barhoum, "A review of 3d polymeric scaffolds for bone tissue engineering: Principles, fabrication techniques, immunomodulatory roles, and challenges," *Bioengineering*, vol. 10, no. 2, p. 204, 2023.
- [2] J. Petzold and E. Gentleman, "Intrinsic mechanical cues and their impact on stem cells and embryogenesis," *Frontiers in Cell and Developmental Biology*, vol. 9, no. 761871, 2021.
- [3] W. Swanson, M. Omi, Z. Zhang, H. K. Nam, Y. Jung, G. Wang, P. X. M, N. E. Hatch, and Y. Mishina, "Macropore design of tissue engineering scaffolds regulates mesenchymal stem cell differentiation fate," *Biomaterials*, vol. 272, no. 120769, 2021.
- [4] N. Salehi-Nik, G. Amoabediny, H. Tabesh, M. Shokrgozard, N. Haghhighipour, N. Khabtibi, F. Anisi, K. Mottaghy, and B. Zandieh-Doulabi, "Engineering parameters in bioreactor's design: a critical aspect in tissue engineering," *Biomed research international*, vol. 2013, no. 2314-6141, p. 762132, 2013.
- [5] B. Archer, *Applications of MRI in Tissue Engineering: Environmental Control and Noninvasive Culture Surveillance*. PhD thesis, University of California, Los Angeles, 2021.
- [6] F. Berthiaume, T. Maguire, and M. Yarmush, "Tissue engineering and regenerative medicine: history, progress, and challenges," *Annual review of chemical and biomolecular engineering*, vol. 2, no. 1947-5438, pp. 406–430, 2011.
- [7] A. Chiu, D. Sharma, and F. Zhao, "Tissue engineering-based strategies for diabetic foot ulcer management," *Advances in wound care*, vol. 12, no. 3, pp. 145–167, 2023.
- [8] A. O. Lukomskyj, N. Rao, L. Yan, J. S. Pye, H. Li, and B. Wang, "Stem cell-based tissue engineering for the treatment of burn wounds: A systematic review of preclinical studies," *Stem cell review and reports*, vol. 18, no. 6, pp. 1926–1955, 2022.
- [9] K. C. Rustad, M. Sorokin, B. Levi, M. T. Longaker, and G. C. Gurtner, "Strategies for organ level tissue engineering," *Organogenesis*, vol. 6, no. 3, pp. 151–157, 2010.
- [10] C. T. Laurencin and L. S. Nair, "The quest toward limb regeneration: a regenerative engineering approach," *Regenerative biomaterials*, vol. 3, no. 2, pp. 123–125, 2016.
- [11] T. Hoffman, A. Khademhosseini, and R. Langer, "Chasing the paradigm: Clinical translation of 25 years of tissue engineering," *Tissue engineering. Part A*, vol. 25, no. 9-10, pp. 679–687, 2019.

- [12] N. Sarkar, S. Bhumiratana, L. Geris, I. Papantoniou, and W. L. Grayson, “Bioreactors for engineering patient-specific tissue grafts,” *Nature Reviews Bioengineering*, vol. 1, no. 5, pp. 361–377, 2023.
- [13] C. J. Shen, J. Fu, and C. S. Shen, “Patterning cell and tissue function,” *Cellular and Molecular Bioengineering*, vol. 1, pp. 15–23, 2008.
- [14] C. T. Laurencin and Y. Khan, “Regenerative engineering,” *Science translational medicine*, vol. 4, no. 160, p. 160ed9, 2012.
- [15] D. Min, W. Lee, I.-H. Bae, T. R. Lee, P. Croce, and S.-S. Yoo, “Bioprinting of biomimetic skin containing melanocytes,” *Experimental Dermatology*, vol. 27, no. 5, pp. 453–459, 2018.
- [16] Y. S. Zhang, A. Arneri, S. Bersini, S.-R. Shin, K. Zhu, Z. Goli-Malekabadi, J. Aleman, C. Colosi, F. Busignani, V. Dell’erba, C. Bishop, T. Shupe, D. Demarchi, M. Moretti, M. Rasponi, M. R. Dokmeci, A. Atala, and A. Khademhosseini, “Bioprinting 3d microfibrous scaffolds for engineering endothelialized myocardium and heart-on-a-chip,” *Biomaterials*, vol. 110, pp. 45–59, 2016.
- [17] M. Carter and J. Shieh, *Guide to Research Techniques in Neuroscience*. Elsevier, Inc., 2015.
- [18] K. H. Benam, S. Dauth, B. Hassell, A. Herland, A. Jain, K.-J. Jang, K. Karalis, H. J. Kim, L. Macqueen, R. Mahmoodian, S. Musah, Y.-s. Torisawa, A. D. van der Meer, R. Villenave, M. Yadid, K. K. Parker, and D. E. Ingber, “Engineered in vitro disease models,” *Annual Reviews Pathology*, vol. 10, pp. 195–162, 2015.
- [19] C. Moysidou, C. Barberio, and R. Owens, “Advances in engineering human tissue models,” *Frontiers in bioengineering and biotechnology*, vol. 8, no. 22964185, p. 620962, 2021.
- [20] A. Khademhosseini and R. Langer, “A decade of progress in tissue engineering,” *Nature Protocols*, vol. 11, no. 10, pp. 1775–1781, 2016.
- [21] S. Przyborski, *Technology Platforms for 3D Cell Culture: A User’s Guide*. John Wiley and Sons, Inc., 2017.
- [22] A. Gonçalves, M. Rodrigues, S. Lee, A. Atala, J. Yoo, R. Reis, and M. Gomes, “Understanding the role of growth factors in modulating stem cell tenogenesis,” *PLoS One*, vol. 8, no. 12, p. e83734, 2013.
- [23] G. Morris, J. Bridge, O. Eltboli, M. Lewis, A. Knox, J. Aylott, C. BRightling, A. Ghaemmaghami, and F. Rose, “Human airway smooth muscle maintain in situ cell orientation and phenotype when cultured on aligned electrospun scaffolds,” *American journal of physiology. Lung cellular and molecular physiology*, vol. 307, no. 1, pp. L38–47, 2014.

- [24] J. Rouwkema, B. Koopman, C. Blitterswijk, W. Dhert, and M. Jos, “Supply of nutrients to cells in engineered tissues,” *Biotechnology and genetic engineering reviews*, vol. 26, no. 1, pp. 163–178, 2010.
- [25] F. Galbusera, M. Cioffi, M. T. Raimondi, and R. Pietrabissa, “Computational modeling of combined cell population dynamics and oxygen transport in engineered tissue subject to interstitial perfusion,” *Computer methods in biomechanics and biomedical engineering*, vol. 10, no. 4, pp. 279–287, 2007.
- [26] A. M. Sailon, A. C. Allpro, E. H. Davison, D. D. Reformat, R. J. Allen, and S. M. Warren, “A novel flow-perfusion bioreactor supports 3d dynamic cell culture,” *Journal of biomedicine and biotechnology*, vol. 2009, no. 873816, pp. 1–7, 2009.
- [27] S. Weinbaum and Y. Zeng, “A model for the excitation of osteocytes by mechanical loading-induced bone fluid shear stresses,” *Journal of biomechanics*, vol. 27, no. 3, pp. 339–360, 1994.
- [28] S. Fritton and C. Rubin, “Quantifying the strain history of bones: spatial uniformity and self-similarity of low-magnitude strains,” *Journal of biomechanics*, vol. 33, no. 3, pp. 317–325, 2000.
- [29] N. Baeyens, C. Badnyopadhyay, B. G. Coon, S. Yun, and M. A. Schwartz, “Endothelial fluid shear stress sensing in vascular health and disease,” *Journal of Clinical Investigation*, vol. 126, no. 3, pp. 821–828, 2016.
- [30] L. C. Delon, Z. Guo, A. Oszmiana, C.-C. Chien, R. Gibson, C. Prestidge, and B. Thierry, “A systematic investigation of the effect of the fluid shear stress on caco-2 cells towards the optimization of epithelial organ-on-chip models,” *Biomaterials*, vol. 225, no. 119521, 2019.
- [31] J. D. Stucki, N. Hobi, A. Galimova, A. O. Stucki, N. Schneider-Daum, C.-M. Lehr, H. Huwer, M. Frick, M. Funke-Chambour, T. Geiser, and O. T. Guenat, “Medium throughput breathing human primary cell alveolus-on-chip models,” *Scientific Reports*, vol. 8, no. 1, 2018.
- [32] S. Diederichs, S. Böhm, A. Peterbaur, C. Kasper, T. Scheper, and M. van Griensven, “Application of different strain regimes in two-dimensional and three-dimensional adipose tissue-derived stem cell cultures induces osteogenesis: Implications for bone tissue engineering,” *Journal of Clinical Investigation*, vol. 94A, no. 3, pp. 927–936, 2010.
- [33] H.-M. Zhou, J. Wang, C. Elliott, W. Wen, D. W. Hamilton, and S. J. Conway, “Spatiotemporal expression of periostin during skin development and incisional wound healing: lessons for human fibrotic scar formation,” *Journal of cell communication and signaling*, vol. 4, no. 2, pp. 99–107, 2010.

- [34] L. Holmgren, A. Glaser, S. Pfeifer-Ohlsson, and R. Ohlsson, “Angiogenesis during human extraembryonic development involves the spatiotemporal control of pdgf ligand and receptor gene expression,” *Development*, vol. 113, no. 3, pp. 749–754, 1991.
- [35] K. Stankunas, G. K. Ma, F. J. Kuhnert, C. J. Kuo, and C.-P. Chang, “Vegf signaling has distinct spatiotemporal roles during heart valve development,” *Developmental biology*, vol. 347, no. 2, pp. 325–336, 2010.
- [36] S. Maxeiner, O. Krüger, K. Schilling, O. Traub, S. Urschel, and K. Willecke, “Spatiotemporal transcription of connexin45 during brain development results in neuronal expression in adult mice,” *Neuroscience*, vol. 119, no. 3, pp. 689–700, 2003.
- [37] M. Iwashita, N. Kataoka, K. Toida, and Y. Kosodo, “Systematic profiling of spatiotemporal tissue and cellular stiffness in the developing brain,” *Development*, vol. 141, no. 19, pp. 3793–3798, 2014.
- [38] T. Schwend and S. C. Ahlgren, “Zebrafish *con/displ1* reveals multiple spatiotemporal requirements for hedgehog-signaling in craniofacial development,” *BMC developmental biology*, vol. 9, no. 1, p. 59, 2009.
- [39] F. Serwane, A. Mongera, P. Rowghanian, D. A. Kealhofer, A. A. Lucio, Z. M. Hockenbery, and O. Campàs, “In vivo quantification of spatially varying mechanical properties in developing tissues,” *Nature methods*, vol. 14, no. 2, p. 181, 2017.
- [40] E. E. Hui and S. N. Bhatia, “Micromechanical control of cell–cell interactions,” *Proceedings of the National Academy of Sciences*, vol. 104, no. 14, pp. 5722–5726, 2007.
- [41] M. J. Song, D. Dean, and M. L. K. Tate, “In situ spatiotemporal mapping of flow fields around seeded stem cells at the subcellular length scale,” *PLoS one*, vol. 5, no. 9, p. e12796, 2010.
- [42] X. Xu, Z. Li, L. Cai, S. Calve, and C. P. Neu, “Mapping the nonreciprocal micromechanics of individual cells and the surrounding matrix within living tissues,” *Scientific reports*, vol. 6, p. 24272, 2016.
- [43] J. J. Mack, K. Youssef, O. D. Noel, M. P. Lake, A. Wu, M. L. Iruela-Arispe, and L.-S. Bouchard, “Real-time maps of fluid flow fields in porous biomaterials,” *Biomaterials*, vol. 34, no. 8, pp. 1980–1986, 2013.
- [44] V. I. Sikavitsas, G. N. Bancroft, and A. G. Mikos, “Formation of three-dimensional cell/polymer constructs for bone tissue engineering in a spinner flask and a rotating wall vessel bioreactor,” *Journal of biomedical materials research*, vol. 62, no. 1, pp. 136–148, 2002.

- [45] K. A. Fitzgerald, M. Malhotra, C. M. Curtin, F. J. O'Brien, and C. M. O'Driscoll, "Life in 3d is never flat: 3d models to optimise drug delivery," *Journal of controlled release*, vol. 215, pp. 39–54, 2015.
- [46] A. C. Luca, S. Mersch, R. Deene, S. Schmidt, I. Messner, K.-L. Schäfer, S. E. Baldus, W. Huckenbeck, W. T. Piekorz, Roland P Knoefel, a. Krieg, and N. H. Stoecklein, "Impact of the 3d microenvironment on phenotype, gene expression, and egfr inhibition of colorectal cancer cell lines," *PLoS One*, vol. 8, no. 3, p. e59689, 2013.
- [47] N. Plunkett and F. J. O'Brien, "Bioreactors in tissue engineering," *Technology and health care*, vol. 19, no. 1, pp. 55–69, 2011.
- [48] S. Van Vlierberghe, P. Dubruel, and E. Schacht, "Biopolymer-based hydrogels as scaffolds for tissue engineering applications: a review," *Biomacromolecules*, vol. 12, no. 5, pp. 1387–1408, 2011.
- [49] A. Charles, "Preparation of collagen sponge," Nov. 17 1964. US Patent 3,157,524.
- [50] H.-W. Kang, Y. Tabata, and Y. Ikada, "Fabrication of porous gelatin scaffolds for tissue engineering," *Biomaterials*, vol. 20, no. 14, pp. 1339–1344, 1999.
- [51] L. A. Hidalgo-Bastida, S. Thirunavukkarasu, S. Griffiths, S. H. Cartmell, and S. Naire, "Modeling and design of optimal flow perfusion bioreactors for tissue engineering applications," *Biotechnology and bioengineering*, vol. 109, no. 4, pp. 1095–1099, 2012.
- [52] J. T. Podichetty and S. V. Madihally, "Modeling of porous scaffold deformation induced by medium perfusion," *Journal of Biomedical Materials Research Part B: Applied Biomaterials*, vol. 102, no. 4, pp. 737–748, 2014.
- [53] F. Maes, P. Van Ransbeeck, H. Van Oosterwyck, and P. Verdonck, "Modeling fluid flow through irregular scaffolds for perfusion bioreactors," *Biotechnology and bioengineering*, vol. 103, no. 3, pp. 621–630, 2009.
- [54] B. Porter, R. Zauel, H. Stockman, R. Guldborg, and D. Fyhrie, "3-d computational modeling of media flow through scaffolds in a perfusion bioreactor," *Journal of biomechanics*, vol. 38, no. 3, pp. 543–549, 2005.
- [55] A. Rahbari, H. Montazerian, E. Davoodi, and S. Homayoonfar, "Predicting permeability of regular tissue engineering scaffolds: scaling analysis of pore architecture, scaffold length, and fluid flow rate effects," *Computer methods in biomechanics and biomedical engineering*, vol. 20, no. 3, pp. 231–241, 2017.
- [56] A. A. Al-Munajjed, M. Hien, R. Kujat, J. P. Gleeson, and J. Hammer, "Influence of pore size on tensile strength, permeability and porosity of hyaluronan-collagen scaffolds," *Journal of Materials Science: Materials in Medicine*, vol. 19, no. 8, pp. 2859–2864, 2008.

- [57] S. Truscello, G. Kerckhofs, S. Van Bael, G. Pyka, J. Schrooten, and H. Van Oosterwyck, "Prediction of permeability of regular scaffolds for skeletal tissue engineering: a combined computational and experimental study," *Acta biomaterialia*, vol. 8, no. 4, pp. 1648–1658, 2012.
- [58] F. J. O'Brien, B. A. Harley, M. A. Waller, I. V. Yannas, L. J. Gibson, and P. J. Prendergast, "The effect of pore size on permeability and cell attachment in collagen scaffolds for tissue engineering," *Technology and Health Care*, vol. 15, no. 1, pp. 3–17, 2007.
- [59] B. Starly, E. Yildirim, and W. Sun, "A tracer metric numerical model for predicting tortuosity factors in three-dimensional porous tissue scaffolds," *Computer methods and programs in biomedicine*, vol. 87, no. 1, pp. 21–27, 2007.
- [60] Y. Reinwald, R. Johal, A. Ghaemmaghami, F. Rose, S. Howdle, and K. Shakesheff, "Interconnectivity and permeability of supercritical fluid-foamed scaffolds and the effect of their structural properties on cell distribution," *Polymer*, vol. 55, no. 1, pp. 435–444, 2014.
- [61] Y. Chen, M. Schellekens, S. Zhou, J. Cadman, W. Li, R. Appleyard, and Q. Li, "Design optimization of scaffold microstructures using wall shear stress criterion towards regulated flow-induced erosion," *Journal of biomechanical engineering*, vol. 133, no. 8, p. 081008, 2011.
- [62] J. A. Stammen, S. Williams, D. N. Ku, and R. E. Guldberg, "Mechanical properties of a novel pva hydrogel in shear and unconfined compression," *Biomaterials*, vol. 22, no. 8, pp. 799–806, 2001.
- [63] W. J. McCarty and M. Johnson, "The hydraulic conductivity of matrigel™," *Biorheology*, vol. 44, no. 5-6, pp. 303–317, 2007.
- [64] M. H. Zaman, L. M. Trapani, A. L. Sieminski, D. MacKellar, H. Gong, R. D. Kamm, A. Wells, D. A. Lauffenburger, and P. Matsudaira, "Migration of tumor cells in 3d matrices is governed by matrix stiffness along with cell-matrix adhesion and proteolysis," *Proceedings of the National Academy of Sciences*, vol. 103, no. 29, pp. 10889–10894, 2006.
- [65] R. G. Wells, "The role of matrix stiffness in regulating cell behavior," *Hepatology*, vol. 47, no. 4, pp. 1394–1400, 2008.
- [66] C. M. Murphy, M. G. Haugh, and F. J. O'Brien, "The effect of mean pore size on cell attachment, proliferation and migration in collagen–glycosaminoglycan scaffolds for bone tissue engineering," *Biomaterials*, vol. 31, no. 3, pp. 461–466, 2010.

- [67] M. Anguiano, C. Castilla, M. Maška, C. Ederra, R. Peláez, X. Morales, G. Muñoz-Arrieta, M. Mujika, M. Kozubek, A. Muñoz-Barrutia, *et al.*, “Characterization of three-dimensional cancer cell migration in mixed collagen-matrigel scaffolds using microfluidics and image analysis,” *PloS one*, vol. 12, no. 2, p. e0171417, 2017.
- [68] Y.-l. Yang, S. Motte, and L. J. Kaufman, “Pore size variable type i collagen gels and their interaction with glioma cells,” *Biomaterials*, vol. 31, no. 21, pp. 5678–5688, 2010.
- [69] O. Lieleg, R. M. Baumgärtel, and A. R. Bausch, “Selective filtering of particles by the extracellular matrix: an electrostatic bandpass,” *Biophysical journal*, vol. 97, no. 6, pp. 1569–1577, 2009.
- [70] R. C. Arevalo, J. S. Urbach, and D. L. Blair, “Size-dependent rheology of type-i collagen networks,” *Biophysical journal*, vol. 99, no. 8, pp. L65–L67, 2010.
- [71] G. Raeber, M. Lutolf, and J. Hubbell, “Molecularly engineered peg hydrogels: a novel model system for proteolytically mediated cell migration,” *Biophysical journal*, vol. 89, no. 2, pp. 1374–1388, 2005.
- [72] B. A. Harley, H.-D. Kim, M. H. Zaman, I. V. Yannas, D. A. Lauffenburger, and L. J. Gibson, “Microarchitecture of three-dimensional scaffolds influences cell migration behavior via junction interactions,” *Biophysical journal*, vol. 95, no. 8, pp. 4013–4024, 2008.
- [73] A. M. Sitarski, H. Fairfield, C. Falank, and M. R. Reagan, “3d tissue engineered in vitro models of cancer in bone,” *ACS Biomaterials Science and Engineering*, vol. 4, no. 2, pp. 324–336, 2017.
- [74] M. Gholipourmalekabadi, S. Zhao, B. S. Harrison, M. Mozafari, and A. M. Seifalian, “Oxygen-generating biomaterials: A new, viable paradigm for tissue engineering?,” *Trends in Biotechnology*, vol. 34, no. 12, pp. 1010–1021, 2016.
- [75] J. Leijten, J. Seo, K. Yue, G. T.-d. Santiago, A. Tamayol, G. Ruiz-Esparza, S. R. Shin, R. Sharifi, I. Noshadi, M. M. Álvarez, Y. S. Zhang, and A. Khademhosseini, “Spatially and temporally controlled hydrogels for tissue engineering,” *Materials science & engineering. R, Reports*, vol. 119, pp. 1–35, 2017.
- [76] G. Vunjak-Novakovic, I. Martin, B. Obradovic, A. Grodzinsky, R. Langer, and L. Freed, “Bioreactor cultivation conditions modulate the composition and mechanical properties of tissue-engineered cartilage,” *Journal of orthopaedic research: official publication of the Orthopaedic Research Society*, vol. 17, no. 1, pp. 130–138, 1999.
- [77] L. Freed, G. Vunjak-Novakovic, and R. Langer, “Cultivation of cell-polymer cartilage implants in bioreactors,” *Gravitational and space biology bulletin*, vol. 51, no. 3, pp. 257–264, 1993.

- [78] G. N. Bancroft, V. I. Sikavitsas, and A. G. Mikos, “Design of a flow perfusion bioreactor system for bone tissue-engineering applications,” *Tissue Engineering*, vol. 9, no. 3, pp. 549–554, 2003.
- [79] K. Youssef, N. N. Jarenwattananon, B. J. Archer, J. Mack, M. L. Iruela-Arispe, and L.-S. Bouchard, “4-d flow control in porous scaffolds: Toward a next generation of bioreactors,” *IEEE Transactions on Biomedical Engineering*, vol. 64, no. 1, pp. 61–69, 2016.
- [80] R. Tiruvannamalai-Annamalai, D. R. Armant, and H. W. Matthew, “A glycosaminoglycan based, modular tissue scaffold system for rapid assembly of perfusable, high cell density, engineered tissues,” *PloS one*, vol. 9, no. 1, p. e84287, 2014.
- [81] P. Galie, D. Nguyen, C. Choi, D. Cohen, P. Janmey, and C. Chen, “Fluid shear stress threshold regulates angiogenic sprouting,” *Proceedings of the National Academy of Sciences*, vol. 111, no. 22, pp. 7968–7973, 2014.
- [82] K. Youssef, J. Mack, M. Iruela-Arispe, and L.-S. Bouchard, “Macro-scale topology optimization for controlling internal shear stress in a porous scaffold bioreactor,” *Biotechnology and bioengineering*, vol. 109, no. 7, pp. 1844–1854, 2012.
- [83] M. A. Brown, R. K. Iyer, and M. Radisic, “Pulsatile perfusion bioreactor for cardiac tissue engineering,” *Biotechnology progress*, vol. 24, no. 4, pp. 907–920, 2008.
- [84] R. Rohanizadeh, M. V. Swain, and R. S. Mason, “Gelatin sponges (gelfoam®) as a scaffold for osteoblasts,” *Journal of Materials Science: Materials in Medicine*, vol. 19, no. 3, pp. 1173–1182, 2008.
- [85] F. S. Majedi, M. M. Hasani-Sadrabadi, Y. Kidani, T. J. Thauland, A. Moshaverinia, M. J. Butte, S. J. Bensinger, and L.-S. Bouchard, “Cytokine secreting microparticles engineer the fate and the effector functions of t-cells,” *Advanced Materials*, vol. 30, no. 7, p. 1703178, 2018.
- [86] G. M. Price, K. H. Wong, J. G. Truslow, A. D. Leung, C. Acharya, and J. Tien, “Effect of mechanical factors on the function of engineered human blood microvessels in microfluidic collagen gels,” *Biomaterials*, vol. 31, no. 24, pp. 6182–6189, 2010.
- [87] A. Ueda, M. Koga, M. Ikeda, S. Kudo, and K. Tanishita, “Effect of shear stress on microvessel network formation of endothelial cells with in vitro three-dimensional model,” *American Journal of Physiology-Heart and Circulatory Physiology*, vol. 287, no. 3, pp. H994–H1002, 2004.
- [88] J. W. Song and L. L. Munn, “Fluid forces control endothelial sprouting,” *Proceedings of the National Academy of Sciences*, vol. 108, no. 37, pp. 15342–15347, 2011.

- [89] C.-L. E. Helm, M. E. Fleury, A. H. Zisch, F. Boschetti, and M. A. Swartz, “Synergy between interstitial flow and vegf directs capillary morphogenesis in vitro through a gradient amplification mechanism,” *Proceedings of the National Academy of Sciences*, vol. 102, no. 44, pp. 15779–15784, 2005.
- [90] H. Kang, K. J. Bayless, and R. Kaunas, “Fluid shear stress modulates endothelial cell invasion into three-dimensional collagen matrices,” *American Journal of Physiology-Heart and Circulatory Physiology*, vol. 295, no. 5, pp. H2087–H2097, 2008.
- [91] C. P. Ng, C.-L. E. Helm, and M. A. Swartz, “Interstitial flow differentially stimulates blood and lymphatic endothelial cell morphogenesis in vitro,” *Microvascular research*, vol. 68, no. 3, pp. 258–264, 2004.
- [92] J. J. Mack, T. S. Mosqueiro, B. J. Archer, W. M. Jones, H. Sunshine, G. C. Faas, A. Briot, R. L. Aragón, T. Su, M. C. Romay, *et al.*, “Notch1 is a mechanosensor in adult arteries,” *Nature communications*, vol. 8, no. 1, p. 1620, 2017.
- [93] D. Lacroix, M. Brunelli, C. Perrault, A. Baldit, M. Shariatzadeh, A. C. Marin, A. Castro, and S. Barreto, *Multiscale Mechanobiology in Tissue Engineering*. Springer, 2019.
- [94] J.-H. Yoo, “Review of disinfection and sterilization-back to the basics,” *Infection and chemotherapy*, vol. 50, no. 2, pp. 101–109, 2018.
- [95] I. Rotstein, “Role of catalase in the elimination of residual hydrogen peroxide following tooth bleaching,” *Journal of endodontics*, vol. 19, no. 11, pp. 567–569, 1993.
- [96] K. Sogawa, R. Okawa, K. Yachiku, M. Shiozaki, T. Miura, H. Takayanagi, T. Shibata, and S. Ezoe, “Effects of continuous exposure to low concentrations of clo_2 gas on the growth of viability, and maintenace of undifferentiates mscs in long-term cultures,” *Regenerative Therapy*, vol. 14, no. 2352-3204, pp. 184–190, 2020.
- [97] R. Perry and D. Green, *Perry’s Chemical Engineer’s Handbook*. The McGraw-Hill Companies, Inc., 1984.
- [98] C. Y. J. Ma, R. Kumar, X. Y. Xu, and A. Mantalaris, “A combined fluid dynamics, mass transport and cell growth model for a three-dimensional perfused bioreactor for tissue engineering of haematopoietic cells,” *Biochemical engineering journal*, vol. 35, no. 1, pp. 1–11, 2007.
- [99] J. Happel, “Viscous flow relative to arrays of cylinders,” *AIChE Journal*, vol. 5, no. 2, pp. 174–177, 1959.
- [100] C. H. Chen, D. O. Clegg, and H. G. Hansma, “Structures and dynamic motion of laminin-1 as observed by atomic force microscopy,” *Biochemistry*, vol. 37, no. 22, pp. 8262–8267, 1998.

- [101] C. H. Chen and H. G. Hansma, “Basement membrane macromolecules: insights from atomic force microscopy,” *Journal of structural biology*, vol. 131, no. 1, pp. 44–55, 2000.
- [102] C. Leblond and S. Inoue, “Structure, composition, and assembly of basement membrane,” *American journal of anatomy*, vol. 185, no. 4, pp. 367–390, 1989.
- [103] V. Serpooshan, M. Julien, O. Nguyen, H. Wang, A. Li, N. Muja, J. E. Henderson, and S. N. Nazhat, “Reduced hydraulic permeability of three-dimensional collagen scaffolds attenuates gel contraction and promotes the growth and differentiation of mesenchymal stem cells,” *Acta biomaterialia*, vol. 6, no. 10, pp. 3978–3987, 2010.
- [104] J. Levick, “Flow through interstitium and other fibrous matrices,” *Quarterly Journal of Experimental Physiology: Translation and Integration*, vol. 72, no. 4, pp. 409–437, 1987.
- [105] H. Sage, R. G. Woodbury, and P. Bornstein, “Structural studies on human type iv collagen.,” *Journal of Biological Chemistry*, vol. 254, no. 19, pp. 9893–9900, 1979.
- [106] B. Trüeb, B. Gröbli, M. Spiess, B. Odermatt, and K. Winterhalter, “Basement membrane (type iv) collagen is a heteropolymer.,” *Journal of Biological Chemistry*, vol. 257, no. 9, pp. 5239–5245, 1982.
- [107] R. DÖLZ, J. ENGEL, and K. KÜHN, “Folding of collagen iv,” *European journal of biochemistry*, vol. 178, no. 2, pp. 357–366, 1988.
- [108] P. R. Macdonald, A. Lustig, M. O. Steinmetz, and R. A. Kammerer, “Laminin chain assembly is regulated by specific coiled-coil interactions,” *Journal of structural biology*, vol. 170, no. 2, pp. 398–405, 2010.
- [109] P. D. Yurchenco, Y.-S. Cheng, and J. C. Schittny, “Heparin modulation of laminin polymerization.,” *Journal of Biological Chemistry*, vol. 265, no. 7, pp. 3981–3991, 1990.
- [110] W. D. Comper, *Heparin (and Related Polysaccharides): Structural and Functional Properties*, vol. 7. Gordon & Breach Publishing Group, 1981.
- [111] A. Oldberg, L. Kjellen, and M. Höök, “Cell-surface heparan sulfate. isolation and characterization of a proteoglycan from rat liver membranes.,” *Journal of Biological Chemistry*, vol. 254, no. 17, pp. 8505–8510, 1979.
- [112] R. V. Rice, E. F. Casassa, R. E. Kerwin, and M. D. Maser, “On the length and molecular weight of tropocollagen from calf skin,” *Archives of biochemistry and biophysics*, vol. 105, no. 2, pp. 409–423, 1964.
- [113] E. G. Young and J. Lorimer, “A comparison of the acid-soluble collagens from the skin and swim bladder of the cod,” *Archives of biochemistry and biophysics*, vol. 92, no. 1, pp. 183–190, 1961.

- [114] V. Serpooshan, N. Muja, B. Marelli, and S. N. Nazhat, “Fibroblast contractility and growth in plastic compressed collagen gel scaffolds with microstructures correlated with hydraulic permeability,” *Journal of Biomedical Materials Research Part A*, vol. 96, no. 4, pp. 609–620, 2011.
- [115] A. Wufsus, N. Macera, and K. Neeves, “The hydraulic permeability of blood clots as a function of fibrin and platelet density,” *Biophysical journal*, vol. 104, no. 8, pp. 1812–1823, 2013.
- [116] H. Brinkman, “A calculation of the viscous force exerted by a flowing fluid on a dense swarm of particles,” *Flow, Turbulence and Combustion*, vol. 1, no. 1, p. 27, 1949.
- [117] D. F. James and A. M. Davis, “Flow at the interface of a model fibrous porous medium,” *Journal of Fluid Mechanics*, vol. 426, pp. 47–72, 2001.
- [118] K. A. Barbee, P. F. Davies, and R. Lal, “Shear stress-induced reorganization of the surface topography of living endothelial cells imaged by atomic force microscopy.,” *Circulation research*, vol. 74, no. 1, pp. 163–171, 1994.
- [119] K. A. Barbee, T. Mundel, R. Lal, and P. F. Davies, “Subcellular distribution of shear stress at the surface of flow-aligned and nonaligned endothelial monolayers,” *American Journal of Physiology-Heart and Circulatory Physiology*, vol. 268, no. 4, pp. H1765–H1772, 1995.
- [120] P. F. Davies, T. Mundel, and K. A. Barbee, “A mechanism for heterogeneous endothelial responses to flow in vivo and in vitro,” *Journal of biomechanics*, vol. 28, no. 12, pp. 1553–1560, 1995.
- [121] R. Van der Sman, “Biopolymer gel swelling analysed with scaling laws and flory–rehner theory,” *Food Hydrocolloids*, vol. 48, pp. 94–101, 2015.
- [122] T. Gervais, J. El-Ali, A. Günther, and K. F. Jensen, “Flow-induced deformation of shallow microfluidic channels,” *Lab on a Chip*, vol. 6, no. 4, pp. 500–507, 2006.
- [123] W. F. Pickard, “The ascent of sap in plants,” *Progress in biophysics and molecular biology*, vol. 37, pp. 181–229, 1981.
- [124] B. Garipcan, S. Maenz, T. Pham, U. Settmacher, K. D. Jandt, J. Zanow, and J. Bossert, “Image analysis of endothelial microstructure and endothelial cell dimensions of human arteries—a preliminary study,” *Advanced Engineering Materials*, vol. 13, no. 1-2, pp. B54–B57, 2011.
- [125] R. Haase, L. A. Royer, P. Steinbach, D. Schmidt, A. Dibrov, U. Schmidt, M. Weigert, N. Maghelli, P. Tomancak, F. Jug, and E. W. Myers, “CliJ: Gpu-accelerated image processing for everyone,” *Nature Methods*, vol. 17, no. 1, pp. 5–6, 2020.

- [126] E. Potthoff, O. Guillaume-Gentil, D. Ossola, J. Polesel-Maris, S. LeibundGut-Landmann, T. Zambelli, and J. A. Vorholt, “Rapid and serial quantification of adhesion forces of yeast and mammalian cells,” *PLoS One*, vol. 7, no. 12, p. e52712, 2012.
- [127] M. Patel, D. A. Wilcox, A. M. Giddings, T. R. McKay, and J. C. Olsen, “81. modification of hek 293 cell integrin expression profile allows convenient large-scale roller bottle production of lentiviral vectors,” *Molecular Therapy*, vol. 9, no. S1, p. S33, 2004.
- [128] D. Wendt, S. Stroebel, M. Jakob, G. John, and I. Martin, “Uniform tissues engineered by seeding and culturing cells in 3d scaffolds under perfusion at defined oxygen tensions,” *Biorheology*, vol. 43, no. 3-4, pp. 481–488, 2006.
- [129] A. Lieder, D. Kaspar, p. Augat, A. Ignatius, and L. Claes, *Mechanosensitivity in Cells and Tissues*. Academia, 2005.
- [130] B. J. Archer, J. J. Mack, S. Acosta, R. Nakasone, F. Dahoud, K. Youssef, A. Goldstein, A. Goldsman, M. C. Held, M. Wiese, B. Blumich, M. Wessling, M. Emondts, J. Klankermayer, M. L. Iruela-Arispe, and L.-S. Bouchard, “Mapping cell viability quantitatively and independently from cell density in 3d gels noninvasively,” *IEEE transactions on bio-medial engineering*, vol. 68, no. 10, pp. 2940–2947, 2021.